Tutorial Vol. 15, No. 1 / March 2023 / *Advances in Optics and Photonics* 1

Advances in Optics and Photonics

Loss in hollow-core optical fibers: mechanisms, scaling rules, and limits

Eric Numkam Fokoua,[1,*] Seyed Abokhamis Mousavi,[1] Gregory T. Jasion,[1] David J. Richardson,[1] and Francesco Poletti[1]

[1] *Optoelectronics Research Centre, University of Southampton, Southampton SO17 1BJ, UK*
**Corresponding author: Eric.Numkam-Fokoua@soton.ac.uk*

Received July 28, 2022; revised September 28, 2022; accepted September 29, 2022; published 20 January 2023

Over the past few years, progress in hollow-core optical fiber technology has reduced the attenuation of these fibers to levels comparable to those of all-solid silica-core single-mode fibers. The sustained pace of progress in the field has sparked renewed interest in the technology and created the expectation that it will one day enable realization of the most transparent light-propagating waveguides ever produced, across all spectral regions of interest. In this work we review and analyze the various physical mechanisms that drive attenuation in hollow-core optical fibers. We consider both the somewhat legacy hollow-core photonic bandgap technology as well as the more recent antiresonant hollow-core fibers. As both fiber types exploit different guidance mechanisms from that of conventional solid-core fibers to confine light to the central core, their attenuation is also dominated by a different set of physical processes, which we analyze here in detail. First, we discuss intrinsic loss mechanisms in perfect and idealized fibers. These include leakage loss, absorption, and scattering within the gas filling the core or from the glass microstructure surrounding it, and roughness scattering from the air–glass interfaces within the fibers. The latter contribution is analyzed rigorously, clarifying inaccuracies in the literature that often led to the use of inadequate scaling rules. We then explore the extrinsic contributions to loss and discuss the effect of random microbends as well as that of other perturbations and non-uniformities that may result from imperfections in the fabrication process. These effects impact the loss of the fiber predominantly by scattering light from the fundamental mode into lossier higher-order modes and cladding modes. Although these contributions have often been neglected, their role becomes increasingly important in the context of producing, one day, hollow-core fibers with sub-0.1-dB/km loss and a pure single-mode guidance. Finally, we present general scaling rules for all the loss mechanisms mentioned previously and combine them to examine the performance of recently reported fibers. We lay some general guidelines for the design of low-loss hollow-core fibers operating at different spectral regions and conclude the paper with a brief outlook on the future of this potentially transformative technology.

https://doi.org/10.1364/AOP.470592

Loss in hollow-core optical fibers: mechanisms, scaling rules, and limits

ERIC NUMKAM FOKOUA, SEYED ABOKHAMIS MOUSAVI,
GREGORY T. JASION, DAVID J. RICHARDSON, AND
FRANCESCO POLETTI

LIST OF SYMBOLS AND ABBREVIATIONS

The following list describes several symbols and abbreviations that will be later used within the body of this manuscript:

α attenuation coefficient

β Propagation constant

κ Spatial frequency, also coupling coefficient

$|\psi_k\rangle$ k^{th} optical mode supported by the fiber

λ Wavelength of light in vacuum

$\omega = \frac{2\pi c}{\lambda}$, optical frequency

ζ material loss suppression factor

$\boldsymbol{c}$ Speed of light in vacuum

$k = \frac{2\pi}{\lambda}$, vacuum wavenumber

$\boldsymbol{u_{nm}}$ m^{th} zero of the Bessel function $J_{n-1}(x)$

7c, 19c, 37c. . . hollow-core photonic bandgap fibers with seven, nineteen, thirty-seven, . . . cells core defects respectively

ARF Antiresonant fiber

HCF Hollow-core fiber

MTF Mechanical transfer function

NANF Nested Antiresonant Nodeless Fiber

PBGF Photonic bandgap fiber

PSD Power spectral density

1. INTRODUCTION

A little over 20 years ago, it was reported for the first time that 35% of light emitted from a laser had been successfully transmitted in the fundamental mode of a 40-mm-long sample of a new optical fiber featuring an air-filled core [1]. This most exciting development was the first reported attempt at demonstrating that concepts of photonic crystals and associated photonic bandgaps could be exploited for light confinement and guidance in long and flexible hollow-core optical waveguides. Pioneering theoretical works by Yablonovich [2] and John [3] which inspired work on the fiber, had independently shown that dielectric structures incorporating three-dimensional wavelength-scale periodic refractive index distributions could inhibit the existence of certain photonic states (characterized by frequency ω and wave vector $\mathbf{k}$). In perfect analogy with the electronic bandgaps in solid-state physics, such structures would not permit even spontaneous emission due to the absence of allowed photonic states, and could thus be used to engineer strong localization of light within a purposely created defect [2,3]. Adopting these concepts, it was shown that with a 2D periodic arrangement of dielectric materials extending infinitely in a third dimension, an out-of-plane photonic bandgap could be realized and thus exploited for light guidance in a suitably engineered core defect. Such an out-of-plane bandgap was possible even with a refractive index contrast as low as that between air and silica [4,5]. Owing to this legacy of adapting concepts from photonic crystals, such fibers came to be known generically as photonic crystal fibers [6–8].

This first demonstration of light guidance in an air core sparked genuine optimism and ushered in an era of intensive research into hollow-core optical fiber technology. The enthusiasm for this technology was justified because light guidance in air either completely removes many of the material imposed limitations of conventional optical fibers, or suppresses them by several orders of magnitude, while uniquely enabling many novel photonics applications by virtue of some unique properties of their own [9,10].

First, the absence of a solid material in the core greatly reduces the likelihood of the core of the fiber incurring damage by dielectric breakdown from high-intensity radiation. At the same time, this also virtually eliminates the Kerr optical nonlinearity present in conventional solid-core optical fibers and vastly improves the power handling ability of hollow-core fibers (HCFs), making them ideally suited for the delivery of continuous wave or high-energy pulsed laser light [11–15]. The nearly three orders of magnitude lower optical nonlinearity implies the removal of the serious impediment of nonlinear noise in optical fiber telecommunications systems, a fundamental limitation to the data-carrying capacity of conventional fiber-based systems [16,17].

Second, by virtue of its group index being very close to 1, a HCF guides light with near-vacuum latency, a property emerging as increasingly important in many data communications applications [18]. Indeed, low latency is advantageous for the deployment and functioning of 5G networks, where timing requirements are stringent [19–24], or in data centers and even supercomputers [25–28]. Moreover, as the optical field of the guided mode inside the hollow core does not interact strongly with the solid material, the low latency is complemented by very low group velocity dispersion and is remarkably resilient to changes in the environment, particularly temperature [29–31]. This unique property makes HCFs ideal for applications in high-precision interferometry, synchronization, and time and frequency metrology [32,33].

Third, removing the solid material from the core of the fiber makes it an ideal platform for the study of light–matter interactions in liquid or gaseous phases, both in the linear and nonlinear regimes [34,35]. Here, the long interaction lengths and the simultaneous confinement of light and fluid materials have led to the realization of many applications including frequency conversion [36], the generation of supercontinua [37], and pulse shaping [38]. Low-loss confinement of light in a hollow core also opens up the possibility of levitating and guiding particles over long distances in such structures [39–41].

Most importantly, however, the excitement about HCF technology was largely born out of the hope that the removal of the solid material from the core of the fiber would result in lower propagation losses than achievable in standard single-mode fibers. Attenuation in the latter is fundamentally imposed by Rayleigh scattering arising from density fluctuations characterizing the disordered nature of glass [42,43]. Such disorder may be quantified through the fictive temperature which is typically higher in fiber than in bulk silica [44]. Over the years, the gap between the fictive temperatures of bulk glass and fiber has narrowed significantly and it is now widely acknowledged that significant loss reduction below ~0.14 dB/km in silica fibers is unlikely. Further loss reduction must therefore employ a medium less susceptible to scattering and with its nearly three orders of magnitude lower density, air is the perfect such medium (and vacuum arguably an even better one). In addition to low scattering, low-loss guidance in air/vacuum is possible at wavelengths where glass is opaque, if the fibers can be designed to avoid a strong overlap between the guided mode field and the solid glass material. This opens up prospects for low-loss optical guidance in spectral regions spanning from the ultraviolet (UV) to the mid-infrared (mid-IR) on a single solid material platform. Despite all these enticing prospects, achieving HCF loss levels comparable to or lower than conventional fibers has proved a formidable challenge until recently [45].

Within a few years of the first report of a HCF, researchers soon discovered that the physical mechanisms exploited to guide light in a hollow core introduce some unique loss mechanisms. First, unlike conventional fibers where total internal reflection ensures that the guided optical modes are truly confined, guiding light in microstructured fibers in general, and in HCFs in particular, is always accompanied by some leakage, i.e., the modes are leaky and a fraction of the optical power flows away from them as they propagates along the fiber axis [46,47] . This leads to *leakage* or *confinement* loss, akin to what results for example from partial reflection when a conventional solid-core fiber is bent and some of the light lost through refraction. One fundamental aspect of the leakage loss is that it increases with the order of the transverse mode, leading to differential loss between guided modes. Second, in HCFs, the presence of many air–glass interfaces gives rise to a unique *surface scattering* mechanism which contributes to loss. Researchers realized early on that in photonic bandgap fibers (PBGFs) for example, the roughness on these interfaces despite being extremely small (sub-nanoscale intrinsic roughness), can lead to substantial scattering loss when the light propagates over long distances. This was found to impose a somewhat fundamental limit to the loss that can be achieved in these fibers [48,49]. In the newer type of hollow-core antiresonant fibers (ARFs), this contribution appears to no longer be dominant, but still plays a role in determining the total loss of the fiber.

In addition to these two distinct and unique loss mechanisms, other intrinsic loss mechanisms present in solid-core fibers also contribute to the loss of HCFs. The first is *Rayleigh scattering* which may originate in the glass or within the hollow regions when they are filled with air or other gases. Rayleigh scattering from gases is nearly three orders of magnitude lower than in glass, making its contribution negligible. In HCFs, a very small fraction of the optical power is guided in the glass. This highly suppresses loss contributions from Rayleigh scattering within the glass regions. The second is *absorption* which may also occur in the glass or within a potential filling gas. Like scattering, glass absorption is highly suppressed due to the small overlap between the guided mode field and the glass material. Absorption in potential filling gases depends on the specific gas composition and the operating wavelength, but can in principle be eliminated by evacuating the fiber.

A range of extrinsic loss mechanisms present in solid-core fibers also affect the loss of HCFs. For example, leakage loss increases when the fiber is bent or deployed in a coiled configuration for applications such as sensors or interferometers. This is known as *macrobend* loss. When the fiber axis deviates locally from a straight path due to random lateral loads applied to it, for example when wound on a drum with a rough surface or pressing against a rough strength member in a cable, it incurs additional loss known as *microbending*. In addition to these bend-induced loss mechanisms, random fluctuations in the fiber manufacturing process result in small structural perturbations or non-uniformities of the fiber structure. As in solid-core fibers, the consequence of such perturbations is to cause power transfer between the core-guided modes and between these core-guided modes and radiation modes, leading to additional loss.

The aim of this article is to present as complete a picture as is currently possible of what is understood or sometimes misunderstood about the physical mechanisms that contribute to loss in HCFs. The mechanisms providing the dominant contribution to loss are inextricably linked to the relevant guidance mechanism and fiber type. We distinguish broadly between two families of fibers. The first is a family of fibers which guide light via a photonic bandgap effect, and here too, the distinction can be made between 1D PBGFs whose cladding consists of an omnidirectional dielectric mirror [50] and 2D PBGFs whose cladding features a 2D periodic honeycomb-like structure [1]. The second family is made of fibers which typically feature a cladding made of an arrangement of thin glass membranes and guide light via a mechanism known as antiresonance or often referred to as inhibited coupling [51,52]. Although these may not encompass all types of HCF, we focus on 2D PBGFs and ARFs because of their demonstrated potential for sub-1-dB/km loss at wavelengths from the visible to the near-IR. We place greater attention still on ARFs which have been the focus of intense research in the last few years and have now demonstrated sub-0.2-dB/km loss in multi-kilometer spans [45]. We start with a brief overview of the current status of performance in both fiber types.

1.1. Current Status of PBGFs

In PBGFs, the cladding region typically consists of a periodic arrangement of dielectric materials in the transverse direction. The choice of these dielectric materials and their arrangement determines the region of the space of photonic states, i.e., the range of frequencies and wave vector $(\omega, \mathbf{k})$ in which the cladding does not support any state. This region is known as the photonic bandgap, in analogy with electronic bandgaps in solid-state physics [2,3]. When a suitable defect is introduced in this arrangement, for example, to form the core of the fiber, it is able to support states which are not allowed in the cladding region and which therefore remain confined and guided along the fiber length.

A distinction can be made between fibers with 1D bandgaps, or so-called Bragg fibers and those with 2D photonic bandgaps. In the former, the hollow-core is surrounded by a cladding consisting of alternating layers of two different materials, often with a high-refractive-index contrast, which provides omnidirectional reflectivity [50,53]. Owing to the requirement of high-index contrast and the small layer thicknesses needed for operation at visible or near-IR wavelengths, such fibers have been most successful for operation at longer wavelengths in the infrared, particularly at the 10.6 μm emission wavelength of CO_2 lasers [50]. Excellent reviews into their properties can be found in Ref. [54]. Here, however, we focus on fibers with 2D bandgaps and simply refer to them as hollow-core photonic bandgap fibers (HC-PBGFs). In these fibers, the hollow core is surrounded by a cladding consisting of a periodic array of air holes embedded in a silica matrix. Such fibers have been intensely researched for applications at wavelengths spanning from the visible to mid-IR. Some examples of cross-sectional images of PBGFs reported in the literature are shown in Fig. 1 and excellent reviews into how these fibers guide light and their key properties can be found in Refs. [9,10].

Figure 1

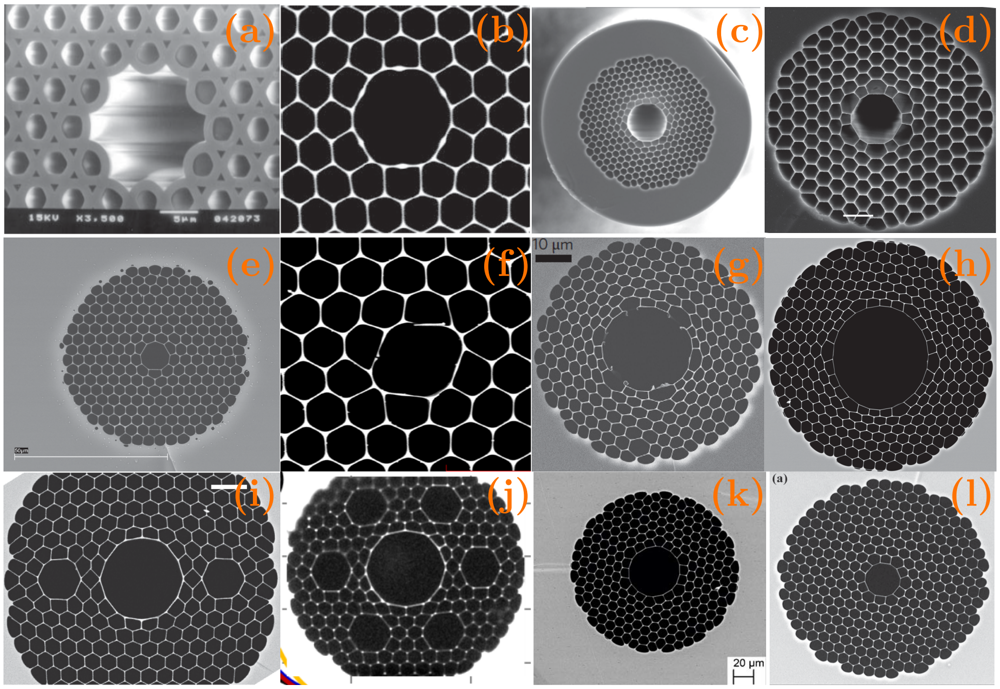

Examples of PBGFs from the literature. (a) First reported fiber from Cregan *et al.* Science, **285**, 1537–1539 (1999) [1]. Reprinted with permission from AAAS. (b) Low-loss 7c fiber from Corning [55]. (c) Low-loss 19c fiber from Mangan *et al.* [56]. Reprinted with permission from B. J. Mangan. (d) Surface-mode free 7c fiber from Amezcua-Correa *et al.* [57]. Reprinted with permission from [57] © The Optical Society. (e) Single-mode 3c bandgap fiber from Petrovitch *et al.* [58]. (f) Highly birefringent 4c fiber from Chen *et al.* [59]. Reprinted with permission from [59] © The Optical Society. (g) Surface-mode free 19c fiber from Poletti *et al.* [18]. (h) First 37c fiber used for mode-division multiplexed data transmission [60–62]. (i) Polarization maintaining fiber [63]. (j) 19c fiber with improved single-modality [19]. Reprinted with permission from B. J. Mangan. (k) Low-loss 19c fiber for mid-IR operation [64]. (l) Commercially available 7c fiber from NKT photonics used by many research groups [65,66]. Reprinted with permission from [66] ©The Optical Society.

It is now well understood that the cladding of HC-PBGFs which most often consists of a triangular lattice of hexagonally shaped air holes, is in fact made up of three *resonator* types which when isolated, support optical modes of their own (as characterized by $(\omega, \mathbf{k})$). These *resonators* are: the glass nodes which are the areas with concentrated glass mass between any three neighboring holes, the interconnecting thin glass struts, and the air holes themselves [10,67,68]. Figure 2 illustrates how the interaction between the modes of these resonators when brought together, leads to the formation of the photonic bandgap. The size of the nodes is key in determining the spectral position of the photonic bandgap, whereas their average spacing determines its width. When brought in close proximity, the modes of the individual nodes near cutoff overlap spatially with each other, leading to the formation of bands of allowed photonic states separated by regions of forbidden photonic states, in perfect analogy with energy band formations and energy gaps in lattices of closely spaced atoms [10]. In principle, when the arrangement of nodes is perfectly periodic, one expects multiple forbidden guidance regions. The addition of the thin glass membranes, necessary for physical support, however, modifies this simple picture by typically closing all but

Figure 2

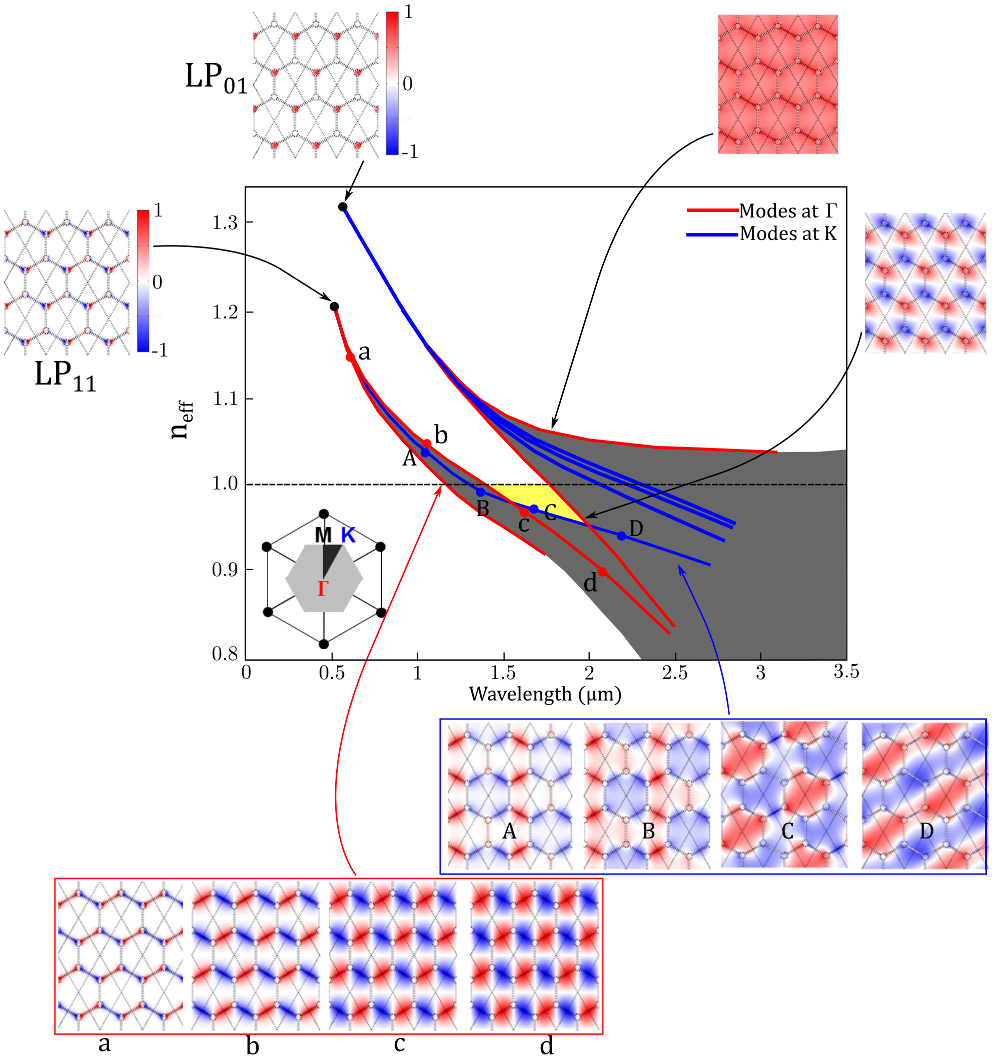

Photonic bandgap guidance in a triangular lattice of holes cladding (adapted from Ref. [68]). At short wavelengths and above the light line ($n_{eff} = 1$), the *nodes* are effectively isolated and support discrete modes labeled LP here for simplicity. As the wavelength increases and the discrete modes in the nodes expand spatially, they start overlapping and forming bands of allowed states (gray areas). Near the light line ($n_{eff} = 1$) where the nodes modes are effectively at cutoff, the modes expand further, overlapping with the struts and air holes regions. However, the gap between the LP$_{01}$ and LP$_{11}$ bands in the nodes extend below the light line, forming the photonic bandgap region (yellow) where no states are allowed in the periodic structure but where an air core can support guided modes.

the fundamental bandgap of the nodes. The size of the resulting air holes determines how far below the air line the photonic bandgap extends. This now widely accepted interpretation of photonic bandgap formation has been called the photonic tight-binding model, again, in analogy with the same concept in solid-state physics [9].

In the two decades following the first demonstration of light guidance in an all-silica HCF, steady progress was made in the development of PBGF technology. The early challenge facing researchers was that of achieving uniform and regular microstructured claddings with sufficiently high air-filling fractions to support wide bandgaps and low-loss guidance. These steps allowed loss reduction from approximately dB/cm levels to approximately dB/m performances. In 2003, a team at Corning reported success in increasing the cladding's air filling fraction from below 50% to above 90%, resulting in the loss reducing to 13 dB/km at 1500 nm in a fiber with a core made by omitting seven unit cells (7c) at the center of the structure [55].

It was thought at first that the attenuation in these fibers resulted from possible longitudinal variations of the structure which may lead to the loss of the bandgap and from the coupling to surface modes [69,70]. It soon emerged, however, that surface scattering from the air–glass interfaces rather than the Rayleigh scattering as in conventional fibers, was the dominant loss mechanism and imposed fundamental limits on the achievable losses in these fibers [49,56,71,72]. These surfaces possess intrinsic residual roughness of thermodynamic origin in the form of frozen-in thermally excited capillary waves, which is as fundamental as the density fluctuations giving rise to Rayleigh scattering in conventional fibers [49,73]. Despite being extremely small (<0.1 nm roughness root mean square (r.m.s.)), this roughness was shown to be capable of causing approximately dB/km level loss. Its fundamental nature implies it cannot be completely removed by current fabrication processes. Further loss reduction therefore required reducing the strength of the guided optical field at the air–glass interfaces. This was achieved by enlarging the core defect to remove 19 unit cells (19c) and using a thick core wall, chosen to be in *antiresonance* at the wavelength of operation. This approach was successful and led to the lowest ever reported loss figures in these fibers, 1.2–1.7 dB/km [49,56,71].

However, using such thick core boundary walls comes at the expense of reducing the operational bandwidth which narrowed to only ~20 nm due to the introduction of surface modes (these are lossy modes supported by the nodes or struts at the core boundary, see Section 2.1d and Refs. [69,70,74]). Such narrow bandwidths severely limit the application prospects for these fibers [49,56]. Theoretical and numerical work later indicated that the operational bandwidth of the fiber could be preserved with acceptable loss penalties if the core wall was approximately half the thickness of the cladding struts [57,75–77]. With this understanding and through further improvements in increasing air-filling fractions, researchers at Bath reported a similar 7c fiber with a loss reduced to 9.5 dB/km [57]. This loss would later be reduced to 3.5 dB/km in a 19c fiber fabricated by our team at Southampton and operating over a bandwidth as large as 160 nm and this remains to date the fiber offering such a record combination of loss and operational bandwidth near 1550 nm [78]. Owing to its unique features, this fiber was among the first to be used to demonstrate high-capacity, low-latency wavelength division multiplexed data transmission in a HCF [18]. Figure 3 summarizes the progress in loss reduction in PBGFs and illustrates this trade-off between loss and bandwidth over the past two decades. Along with these breakthroughs, remarkable progress was made in the fabrication of such fibers, with demonstrations of the ability to draw them in lengths up to 10 km [81], aided by accurate modeling of the fluid dynamics of the fiber draw process [82,83].

Enlarging the core of the fiber by removing a further ring of holes (18 unit cells) appeared to be the next necessary step to reduce the loss in these fibers beyond the reported figures. Reported fibers with 37c core sizes did not, however, achieve the expected lower losses [60]. Beyond the practical difficulty of controlling the fiber structure with such large cores, we believe that the role of other loss mechanisms, particularly of extrinsic origin such as microbending which become significant for larger core sizes, or the longitudinal variations of the structure (particularly its core), were not considered and had not yet been properly understood. Providing a comprehensive analysis that encompasses such contributions is the aim of this paper.

Figure 3

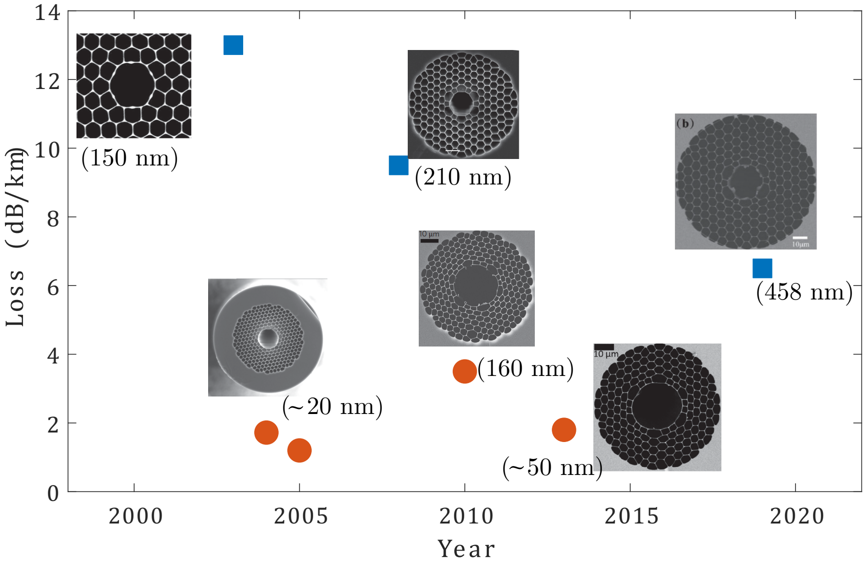

Loss progression in HC-PBGFs over the years. The blue squares indicate 7c fibers (from, left to right, [55, 57] (reprinted with permission © The Optical Society), [79] (reprinted with permission © The Optical Society)), and the orange dots 19c fibers (from left to right, [49,56] (reprinted with permission from B. J. Mangan), [78, 80] (reprinted with permission © The Optical Society)). For each fiber, the number in the parentheses reports the measured operational low-loss bandwidth.

1.2. Current Status of ARFs

After a few years of intense research into HCPBGFs, researchers at the University of Bath reported a HCF that appeared to achieve approximately dB/m loss levels over octave-spanning spectral bandwidths that would not be expected if a photonic bandgap was the underlying guidance mechanism [51]. It would later emerge that unlike PBGFs, these fibers with a Kagomé-like cladding relied on a combination of inhibited coupling to *low density of states* cladding modes and antiresonance from the thin glass membranes making up the cladding [34,51]. One marked difference with PBGFs as it was soon discovered, is that the addition of further rings of air holes to the structure did not seem to reduce the loss of the fibers which numerical modeling showed was dominated by leakage or confinement loss (we henceforth use the terms leakage or confinement loss interchangeably) [84,85]. This realization led to many reports of fibers with effectively a single ring of air holes in the cladding but with relatively uncompromised loss performance [86,87].

In this class of fibers, there is no accumulation of glass at the intersection of the thin membranes to form the *nodes* we identified as key for photonic bandgap guidance (except arguably on the core boundary where they have a negative effect on loss, see Section 2.1d). Instead, the thin glass membranes themselves are the *resonators* that dictate the overall guidance in the fiber. When they are of equal thickness t and refractive index n, they are effectively transparent to resonant wavelengths given by [34]

$$\lambda_m = \frac{2t}{m}\sqrt{n^2 - 1}, \quad m = 1, 2, 3, \ldots . \tag{1}$$

Wavelengths between these resonances however, can be confined and guided in the core with low loss. In analogy therefore to Fabry–Pérot interferometers where the condition under which reflectivity is optimal is called antiresonance, these fibers have been referred to as ARFs, and we adopt this terminology throughout this paper.

In the years following their introduction, ARFs were perceived as generally suffering from much higher loss than the PBGFs, although they offered wider, often octave-spanning operational bandwidths. Furthermore, the spectral loss of such fibers showed spurious loss peaks and dips across the transmission bands due to the relatively thicker nodes at the intersection of the membranes, particularly those on the core boundary [34,84,99,100]. A step change in this type of fiber occurred when it was realized, accidentally perhaps, that the loss reduced substantially if the core boundary was such that these nodes were positioned far away from the center of the core, with the core boundary curved inwards, leading to the so-called hypocycloid-core Kagomé fibers or negative curvature fibers [88,101]. Detailed studies have shown that the key to loss reduction may not lie entirely in the negatively curved shape of the core boundary itself. Rather, it can also be achieved if the core boundary is such that it prevents the waves leaking from the core region from interfering constructively in the far-field [102–104]. Introducing the negatively curved core boundary design and combining it with the knowledge that further cladding rings of air holes did not play an important role in reducing the loss led to much simplified designs consisting of a single ring of cylindrical tubes, contacting at first and non-touching later [86,89,90]. Despite their simple structures, such ARFs have shown remarkable improvements in performance and are now outperforming PBGFs on many accounts, including achievable attenuation and operational bandwidths. Excellent reviews into how these fibers guide light can be found in Refs. [35,105–107] and Fig. 4 shows cross sections of example ARFs reported in the literature.

In ARFs, scattering from surface roughness plays a minor role in determining the fiber attenuation because at antiresonant wavelengths, the electromagnetic field intensity near the air–glass interfaces is minimized due to destructive interference between incident and reflected waves on the thin glass membranes [52,71]. This is the very same principle exploited to achieve the lowest loss to date in bandgap fibers, albeit at the cost of severely limited operational bandwidth due to the introduction of surface modes [49,71]. In ARFs with non-contacting tubes, however, no such penalty is present and scattering from surface roughness is low across all the available operational window. So far, loss appears instead to be dominated by contributions from leakage.

Figure 5 shows some examples of recently reported ARFs with minimum loss at wavelengths spanning from 500 nm to 5 µm. As can be seen, fibers with the simple cladding geometry made of non-contacting and non-nested tubes (henceforth referred to as tubular fibers) are, in effect, the most prevalent type and offer losses below that of pure silica at almost all wavelengths, except in the range from 800 nm to about 2 µm. Loss in this spectral range is dominated by leakage. An important step for further leakage loss reduction in ARFs operating in this highly technologically relevant spectral region was a proposal to reduce the leakage loss by introducing nested tubes to enhance light confinement in the hollow core [114]. At the same time, ensuring no contact points between the sets of nested tubes led to the seminal introduction of the nested antiresonant nodeless fiber (NANF) concept [52]. Contact points, if present, would introduce spurious resonances with a negative effect on loss. Four years after these theoretical proposals, a group in Beijing reported a fiber based on a similar concept of enhancing the reflection to lower the leakage loss [94], achieving a minimum loss of ~2 dB/km near 1512 nm, but still suffering from small spurious loss peaks due to the presence of small nodes in the conjoined-tube design.

Subsequently, research efforts in producing NANFs have brought hollow-core ARF technology to the cusp of genuine breakthroughs. Their lowest attenuation now

Figure 4

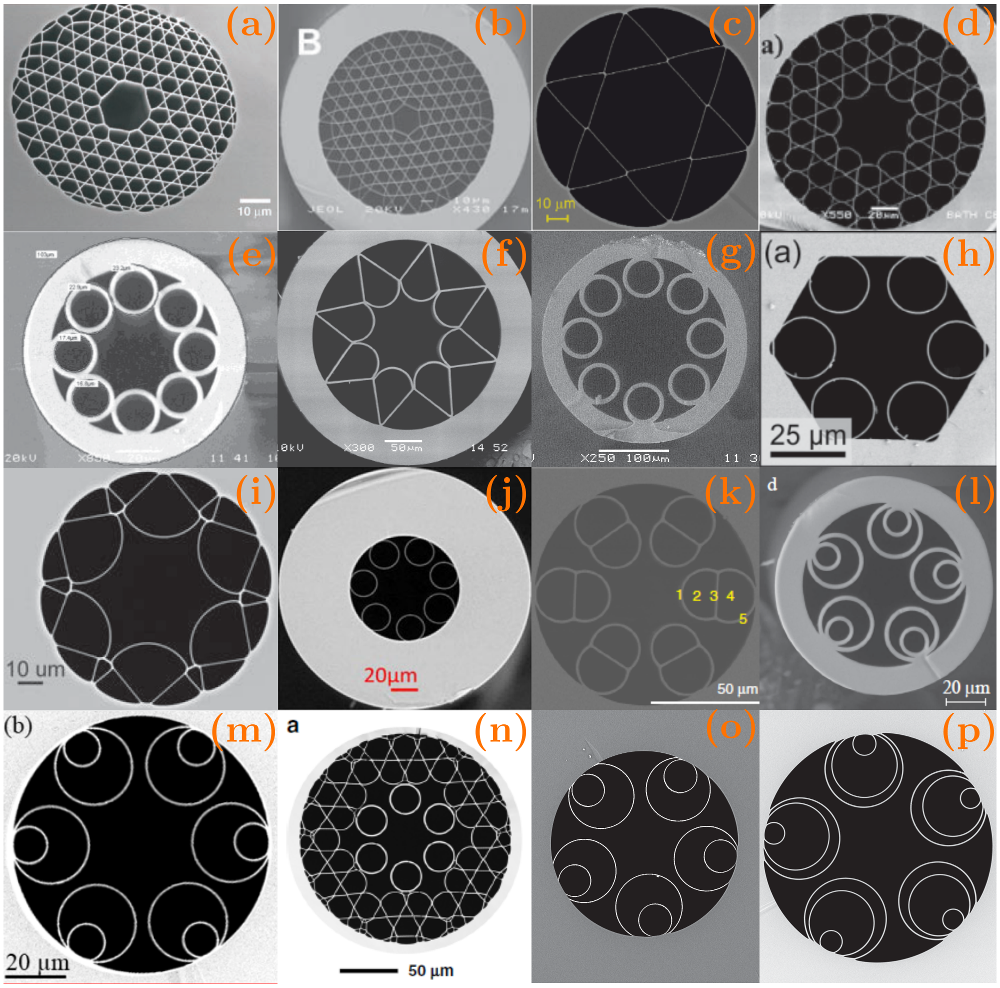

Example antiresonant hollow-core optical fibers from the literature: (a) Kagomé fiber from [51] (from Benabid *et al.*, Science, **298**, 399–402 (2002) [51], reprinted with permission from AAAS), (b) large-pitch single-cell-core Kagomé fiber (from Couny *et al.*, Science **318**, 1118–1121 (2007) [34], reprinted with permission from AAAS), (c) antiresonant hexagram HCF [87], (d) hypocycloid-core Kagomé fiber (from [88], reprinted with permission ©The Optical Society), (e) negative curvature fiber (from [89], reprinted with permission from ©The Optical Society), (f) negative curvature fiber (from [86], reprinted with permission ©The Optical Society), (g) *revolver* hollow-core optical fiber (reprinted with permission from [90] ©The Optical Society), (h) effectively single-mode six-tube fiber (reprinted with permission from [91] ©The Optical Society), (i) lotus fiber from Ref. [92], (j) low-loss tubular fiber with octave spanning bandwidth from Ref. [93], (k) conjoined-tube fiber from Ref. [94], (l) nested fiber from Kosolapov *et al.* [95] (reprinted with permission from Turpion), (m) first sub-dB/km NANF from Ref. [96], (n) hybrid cladding fiber from Ref. [97], (o) low-loss (0.22 dB/km) 5-tube NANF from Ref. [98], (p) record low-loss double nested antiresonant fiber (DNANF) from Ref. [45].

stands at 0.174 dB/km, 20% above that of pure-silica-core single-mode fibers in the telecommunications C-band, but comparable to commercial germanium-doped core single-mode fibers [45,98,115]. Furthermore, these fibers are now the most transparent fibers ever made in all other spectral regions including the visible, the important wavelengths of 850 and 1060 nm as well as in the mid-IR [116,117]. Such low loss

Figure 5

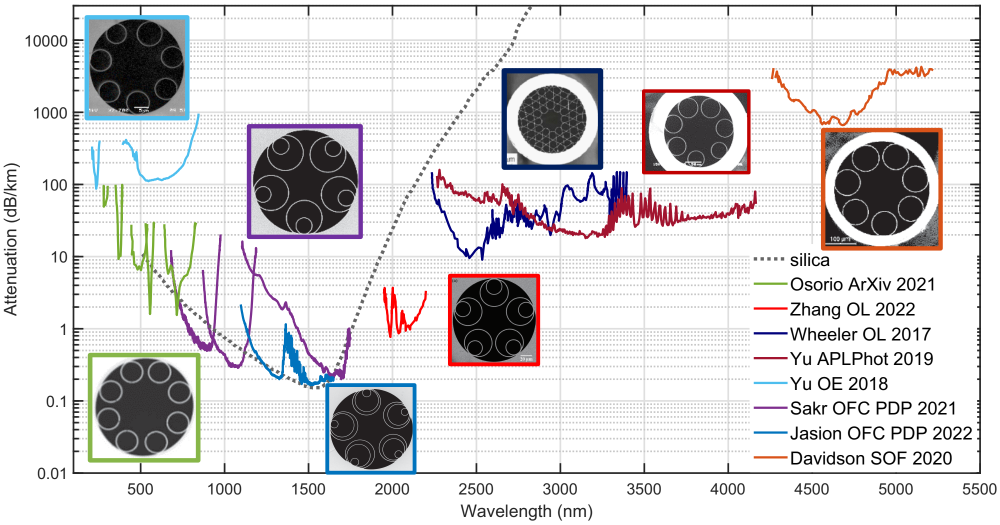

Lowest-loss ARFs reported in the literature. From left to right: cyan, Yu *et al.* (reprinted with permission from [108] ©The Optical Society); green, Osório *et al.* [109] (reprinted with permission from F. Benabid); purple, Sakr *et al.* [98]; blue, Jasion *et al.* [45]; red, Zhang *et al.* (reprinted with permission from [110] © Optica Publishing Group); dark blue, Wheeler *et al.* [111]; dark red, Yu *et al.* [112]; orange, Davidson *et al.* [113]. The dashed black line shows the loss of bulk silica for comparison.

values are ushering in an era of flexible, long length optical fibers and cables with near-vacuum optical properties, something unachievable in conventional glass-core fibers.

The advent of such low losses has prompted a greater need for a deeper understanding of the mechanisms that will ultimately limit the attenuation in these fibers. Such a complete picture must encompass the known intrinsic loss contributions from leakage and surface scattering, and also take into account extrinsic loss mechanisms such as microbending as well as the coupling between fundamental and lossy higher-order modes arising from a range of perturbations along the fiber length.

The remainder of this paper is aimed at providing such a picture and is organized as follows: the first part discusses the *intrinsic* loss mechanisms where Section 2.1 is devoted to leakage loss, reviewing its origins, interpretations, and dependence on the guiding mechanisms. This is followed by a discussion of the material absorption in Section 2.2. In Sections 2.3 and 2.4, we discuss scattering contributions to loss, first from bulk contributions in either the glass or the gas within the hollow regions, followed by scattering from surface roughness. This first part is completed by a brief discussion of how these intrinsic mechanisms affect the higher-order core-guided transverse modes and lead to mode-dependent loss in Section 2.5. The second part explores *extrinsic* contributions to loss, starting with the effect of random microbends in Section 3.1 and other potential random perturbations in Section 3.2. In Section 3.3, we discuss macrobend loss occurring when the fiber is deployed at a constant curvature diameter such as in a coil. In the final part of the paper, we bring all these contributions together to discuss the loss performance in state-of-the-art HCFs in Section 4.1. The scaling rules derived throughout the paper are used to make projections for potentially achievable losses in ARFs in Section 4.2. Section 4.3 presents our take on the future prospects of this exciting technology, followed by concluding remarks in the final section.

2. INTRINSIC LOSS MECHANISMS

2.1. Leakage or Confinement Loss

In standard solid-core single or multimode fibers, the core has a higher refractive index than the surrounding cladding and light is confined and guided in the core region by virtue of total internal reflection. This is known as index guiding. In a ray-optics picture, confined rays are incident on the core-cladding interface at an angle greater than the critical angle and, therefore, as per Fresnel's law, undergo perfect lossless reflection. As a result, solid-core index-guiding fibers do not suffer from leakage loss. The situation changes however for higher-order modes at wavelengths longer than their cutoff or when the fiber is bent. When this is the case, the rays only experience partial reflections at the core/cladding interface and thus suffer power loss due to refraction. These rays have been called leaky, and the associated loss is therefore termed leakage or confinement loss [118].

From the perspective of optical modes, the guided modes in a solid-core fiber in which the core with refractive index n_1 is surrounded by a cladding with index n_2 have real propagation constants β_k that satisfy $n_2k_0 \leq \beta_k \leq n_1k_0$. That is, β_k must be larger than the wavenumber in the cladding. Such modes are therefore strictly confined and not subject to leakage. Below a mode's cutoff frequency, some solutions to Maxwell's equations possess complex propagation constants, corresponding to fields that continuously lose power as they propagate [118,119]. The leakage loss coefficient is then expressed as the imaginary part of the propagation constant:

$$\alpha\ (\mathrm{dB/m}) = \frac{20}{\log 10}\Im(\beta). \tag{2}$$

In HCFs, perfect reflection at the *core/cladding boundary* does not occur. Regardless of the chosen guidance mechanism, HCFs typically have a silica jacket with a higher refractive index than the central hollow-core region. As a result, any core-guided mode has a lower propagation constant than the wavenumber in the outermost silica layer, and thus is subject to tunneling or leakage [54]. The guidance mechanism however, is crucial in determining the relative contribution of this loss mechanism to the total loss of the fiber and in devising adequate strategies to reduce it. It is known for example that in PBGFs, leakage loss can be reduced to arbitrarily low levels simply by adding further rings of air holes in the cladding [47,120]. In ARFs, a demonstrated route to loss reduction has been the addition of nested elements [52]. In the following, we review the key physical insights to help understand the physical origin of this loss contribution in HCFs.

2.1a. Understanding Leakage Loss as Partial Ray Reflection

One of the ways in which leakage loss can be understood, regardless of the guiding mechanism involved, is by conceiving it as the result of partial reflection at the *boundary* between core and cladding. When this is the case, the residual refraction means that optical power radiates away from the core region. This interpretation from the ray-optics picture implies that leakage loss in hollow waveguides can be estimated from an effective reflection coefficient at each reflection. To illustrate this, we consider the simplest HCF possible, a circular hollow region surrounded by an infinitely extending dielectric region first studied by Marcatili and Schmeltzer [121] (see Fig. 6). Let us consider such a waveguide made of an air-filled core of radius a surrounded by silica. When $a \gg \lambda$ (λ is the wavelength), the real part of the propagation constant for the $\mathrm{EH_{nm}}$ mode is given as [121]

$$\Re(\beta_{mn}) = \frac{2\pi}{\lambda}\left\{1 - \frac{1}{2}\left(\frac{u_{nm}\lambda}{2\pi a}\right)^2\right\}, \tag{3}$$

where u_{nm} the mth zero of the Bessel function of the first kind $J_{n-1}(x)$. From the real part of the propagation constant, one works out that the incidence angle of corresponding light rays is simply

$$\theta_i = \frac{\pi}{2} - \arccos\frac{\mathcal{R}(\beta_{nm})}{k_0} \simeq \frac{\pi}{2} - \left(\frac{u_{nm}\lambda}{2\pi a}\right). \tag{4}$$

Here, $k_0 = 2\pi/\lambda$ is the free-space wavenumber. After some simple algebra, one can show using Fresnel's equation that for this incident angle when the ray is s- (therefore TE) or p-polarized (TM), the power reflection coefficient per reflection is

$$R_s \approx 1 - \frac{4}{\sqrt{n^2-1}}\left(\frac{u_{nm}\lambda}{2\pi a}\right), \tag{5}$$

$$R_p \approx 1 - \frac{4n^2}{\sqrt{n^2-1}}\left(\frac{u_{nm}\lambda}{2\pi a}\right), \tag{6}$$

where n is the refractive index of the glass material. A meridional ray with the incident angle above undergoes a number N of reflections per unit distance given by

$$N = \frac{\tan\left(\pi/2 - \theta_i\right)}{2a} \approx \frac{u_{nm}\lambda}{4\pi a^2}. \tag{7}$$

Combining the equations above, one finds that the linear power loss coefficient per unit length of the ray is simply

$$\alpha_s = -N\log(R_s) \approx \left(\frac{u_{nm}}{2\pi}\right)^2\frac{\lambda^2}{a^3}\frac{2}{\sqrt{n^2-1}} + O(\lambda^3/a^4), \tag{8}$$

$$\alpha_p = -N\log(R_p) \approx \left(\frac{u_{nm}}{2\pi}\right)^2\frac{\lambda^2}{a^3}\frac{2n^2}{\sqrt{n^2-1}} + O(\lambda^3/a^4). \tag{9}$$

From this simple picture of partial reflection, we are thus able to reproduce exactly the expressions derived by Marcatili and Schmeltzer obtained through solving Maxwell's equations [121], giving credence to this intuitive understanding of leakage loss. The same treatment above also reproduces exactly expressions derived for a dielectric tube waveguide [122] and by extension those from a multilayered model structure with l alternating glass/air layers as examined by Bird [123] which state that to the leading order,

$$\alpha_{TE}\ (\text{dB/m}) = \frac{20}{\ln 10}\left(\frac{u_{nm}}{2\pi}\right)^{l+2}\left(\frac{1}{\sqrt{n^2-1}}\right)^{l+1}\left(\frac{\lambda^{l+2}}{a^{l+3}}\right)\prod_{i=1}^{m}\frac{1}{\sin^2(\phi_i)}, \tag{10}$$

$$\alpha_{TM}\ (\text{dB/m}) = \frac{20}{\ln 10}\left(\frac{u_{nm}}{2\pi}\right)^{l+2}\left(\frac{n^2}{\sqrt{n^2-1}}\right)^{l+1}\left(\frac{\lambda^{l+2}}{a^{l+3}}\right)\prod_{i=1}^{l}\frac{1}{\sin^2(\phi_i)}, \tag{11}$$

where ϕ_i is the transverse phase accumulated across each air or glass layer labeled i. The loss of hybrid modes is the average of the two. From these expressions, the hollow dielectric waveguide of Marcatili and Schmeltzer would correspond to $l = 0$ and a thin tube to $l = 1$. We plot in Fig. 6 the leakage loss for the fundamental mode (solid colored curves) and LP_{11}-like modes (dashed lines) for the hollow dielectric waveguide and a silica tube of thickness $t = 550nm$. Note how for the tube, the loss show the resonance peaks described by Eq. (1), corresponding to $\phi_1 = 2\pi t\sqrt{n^2-1}/\lambda = m\pi$ [123]. Although these model structures are only simplifications of practical fibers, they convey some important features of the loss properties in HCFs. The first is that leakage can be made arbitrarily low by increasing the core size. This comes, as we show, at the cost of the fiber supporting an increasingly high number of modes and

Figure 6

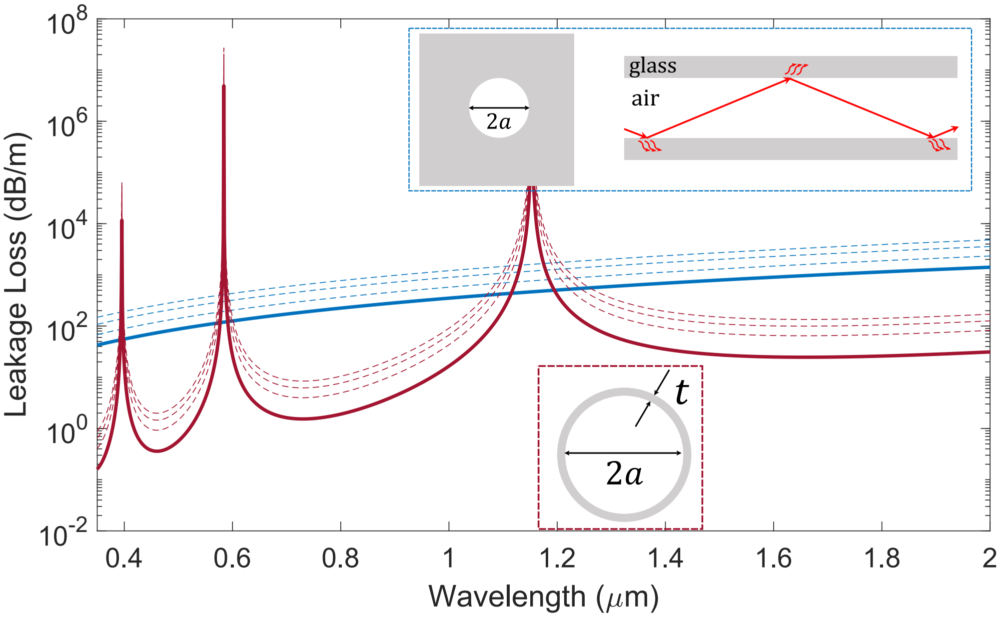

Leakage loss from a hollow dielectric waveguide and dielectric tube waveguide estimated through the prism of partial reflection at the air–glass interfaces. The solid lines show the loss of the lowest loss LP_{01}-like mode and the dashed lines the calculated loss for the LP_{11}-like modes (the TM_{01} is the highest loss mode, the HE_{21} modes are degenerate, and the TE_{01} has the lowest loss).

a dramatic increase in bend-induced penalties. Second, leakage loss for higher-order modes is higher than that of the fundamental mode. In the simple ray-optics picture, the corresponding light rays are incident on the core cladding interface with increasingly more oblique angles and this is reflected in the analytical expression through the loss scaling as u_{nm}^2 ($u_{nm} = 2.4048, 3.8317, 5.1356, 5.5201, 6.3802, \ldots$). Third, the polarization of the modes is important as the loss of TM modes is n^2 times higher than that of the TE modes of the same order. Finally and more importantly, higher reflectivity coefficients of the cladding can lead to much lower losses. In PBGFs, the reflectivity generally increases with the number of cladding rings, reaching unity when infinitely many rings are incorporated. The same holds in ARFs. From the model structures studied by Bird, we see from Eqs. (10) and (11) that the addition of more antiresonant layers leads to reduced loss. In practical fibers, this takes the form of additional nested tubes such as in the NANF, or further reflective layers such as in the conjoined tube structures, which lead to orders of magnitude lower losses.

2.1b. Leakage Loss Arising from Mode Coupling and the Inhibited Coupling Picture

It has recently been shown that with knowledge of the reflectivity of a given cladding design (which one can only calculate numerically for more complex designs), the simple ray optics formalism above can give accurate predictions of the leakage loss of the fiber [124]. However, despite its appealing simplicity, the ray picture does not capture all of the intricacies of leakage loss and its dependence on fiber parameters in most practical cases. This is exacerbated by the fact that the reflectivity of the cladding in most cases can only be obtained numerically, making it difficult to easily draw useful conclusions such as the dependence of loss and mode-dependent loss on fiber parameters.

An alternative interpretation, also credited as key to the guiding mechanism in ARFs, is the so-called inhibited coupling interpretation [34,125]. Here, the complex structure of a HCF is regarded as an arrangement of different *waveguides* which would support their own modes with defined propagation constants and loss when isolated. These *waveguides* are the central hollow core, the cladding structure which may be further subdivided into its own constituent waveguides, and the surrounding silica jacket. We refer to the modes supported by these waveguides with the notation $|\psi\rangle$ and clarify explicitly which regions of the fiber supports them or through the use of subscript labels. A low-loss core mode propagating alongside the continuum of lossy and leaky cladding and jacket modes has been likened to the quantum mechanical concept of abound state in the continuum [126,127]. Let us now assume that a core mode $|\psi_k\rangle$ propagates alongside a cladding or jacket mode $|\psi_l\rangle$ which has loss coefficient α_l. In this case, a coupled mode theory formalism has been invoked to show that for sufficiently long propagation distances, the core mode suffers additional loss given by [69,70]:

$$\alpha_{k,l} \approx \frac{\alpha_l |\kappa_{k,l}|^2}{(\Delta\beta_{k,l}/2)^2 + |\kappa_{k,l}|^2}, \tag{12}$$

where $\Delta\beta_{k,l}$ is the difference between the propagation constants of the core and cladding modes and $\kappa_{k,l}$ is a coupling coefficient or overlap integral between their corresponding mode fields. One can therefore postulate that if we were to know the loss and propagation constants of all the cladding modes, the leakage loss α_k of the core mode $|\psi_k\rangle$ could be written as a superposition of the losses due to coupling to cladding and jacket modes:

$$\alpha_k = \sum_l \frac{\alpha_l |\kappa_{k,l}|^2}{(\Delta\beta_{k,l}/2)^2 + |\kappa_{k,l}|^2}, \tag{13}$$

where the summation is across all the discrete cladding modes and takes the meaning of an integral when such modes form a continuum.

Despite their almost deceptive simplicity, these expressions offer a powerful insight. First, if core and lossy cladding modes possess a similar propagation constant, i.e., $\Delta\beta \sim 0$, then as long as the coupling between the two is not zero, the loss of the core mode tends asymptotically toward the loss of said cladding mode. This offers the prospect of designing cladding features to strip out undesired higher-order core modes, for example, by engineering them so that they support lossy modes with the same propagation constant as said core mode. This is the underlying principle used to achieve effective single-mode operation in bandgap structures [128–131] and in ARFs [91].

Second, the propagation of a core mode is unaffected by the presence of lossy cladding modes, even if they have the same propagation constant, provided their coupling strength κ is zero. As the coupling between core and cladding modes is related to a spatial overlap integral, it is apparent that if the modes are highly localized, i.e., they occupy different regions of the cross section with vanishing overlap between the tails of their transverse profiles, then the core mode cannot be affected. This is the case for example in PBGFs. The periodic cladding supports no modes with the same propagation constant as the core modes, however, some radiation modes of the silica jacket fulfill this condition. Adding more rings of air holes outside the core ensures sufficiently large physical distance between the core and jacket, allowing the tail of the core modes to decay substantially, thereby limiting their overlap, resulting in leakage loss being negligible. The coupling integral can also be drastically reduced and made vanishingly small if the transverse phase profile of one of the modes changes very rapidly whereas that of the other does not, in effect rendering the modes orthogonal. This, it has been argued, is the case for example when the innermost boundary of the core in Kagomé fibers is curved so as to look convex from the core [88,127,132–134]. The introduction of such a *negatively* curved core boundary resulted in dramatic loss reduction in this type of fiber [88]. We note, however, that an important feature of such a core boundary is that it pushes glass *nodes* at the core boundary away from the center of core, thereby significantly reducing the overlap between core modes and the lossy modes localized therein. This effect is the same as the substantial loss reduction in going from a cladding formed of contacting thin glass tubes to non-contacting thin glass tubes, removing entirely the local glass *nodes* [52].

Although conceptually straightforward, the great difficulty in estimating the loss of the fiber using the expressions above lies in the fact that a large number of cladding modes, which cannot be obtained analytically in any practical case, must be included for an acceptable approximation. In most cases, the difficulty and computational cost in obtaining those modes is greater than that of solving numerically for the leakage loss directly. Yet, the physical insight is of paramount importance in improving fiber designs.

2.1c. Leakage Dependence on Guidance Mechanism and Cladding Design

The extent to which leakage contributes to loss in HCFs is inextricably linked to the adopted guidance mechanism. For the remainder of the paper, we focus on 2D photonic bandgap and antiresonance guiding fibers. Specifically, we often compare side by side the performance of a model PBGF with a 19c core defect and a model NANF with the same core diameter. The structural parameters for these illustrative examples used throughout the paper are described in Fig. 7. The first step in obtaining all of the results presented in the paper is to solve for the modes guided in these fibers using a fully vectorial finite-element solver. The platform used is the commercial COMSOL Multiphysics package. To guarantee the accuracy of the solution, we used for the PBGF a triangular mesh with a maximum mesh size of $\lambda/4$ in the core and $t/2$ in the glass

Figure 7

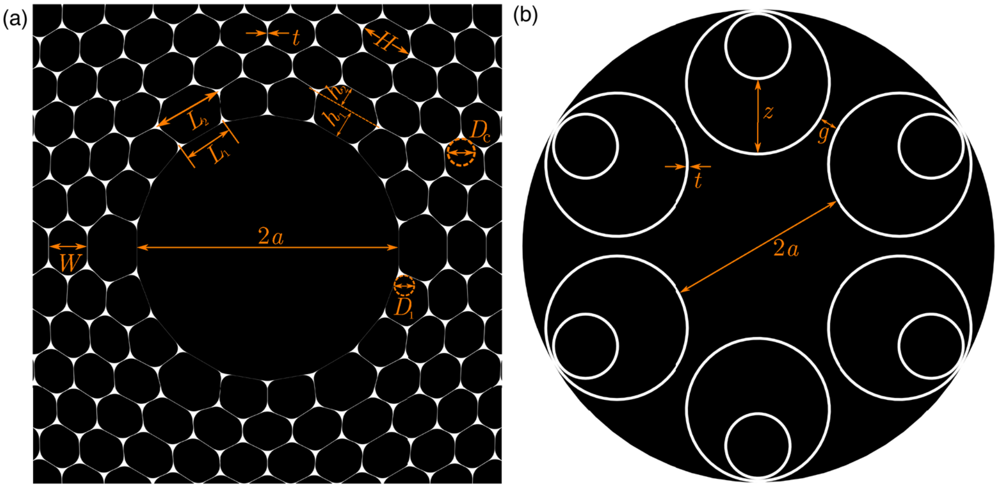

Structural parameters of the example (a) PBGF and (b) NANF used throughout the paper. The structure of the PBGF is optimized for low-loss operation as described in Ref. [135]. Its key parameters are a core diameter $2a = 29.6$ μm, an average cladding strut thickness $t = 47$ nm, average cladding hole width $W = 4.7$ μm, and average cladding hole fillet diameter $Dc = 0.63W$. The nodes on the core boundary are equidistant to give the core an almost circular shape, and the core wall is half as thick as the cladding struts. For the NANF, we use a core diameter $2a = 30$ μm, a cladding membrane thickness $t = 550$ nm, a gap between the large tubes $g = a/5 = 3$ μm, and the size of the first cladding cavity $z = 0.8a$.

Figure 8

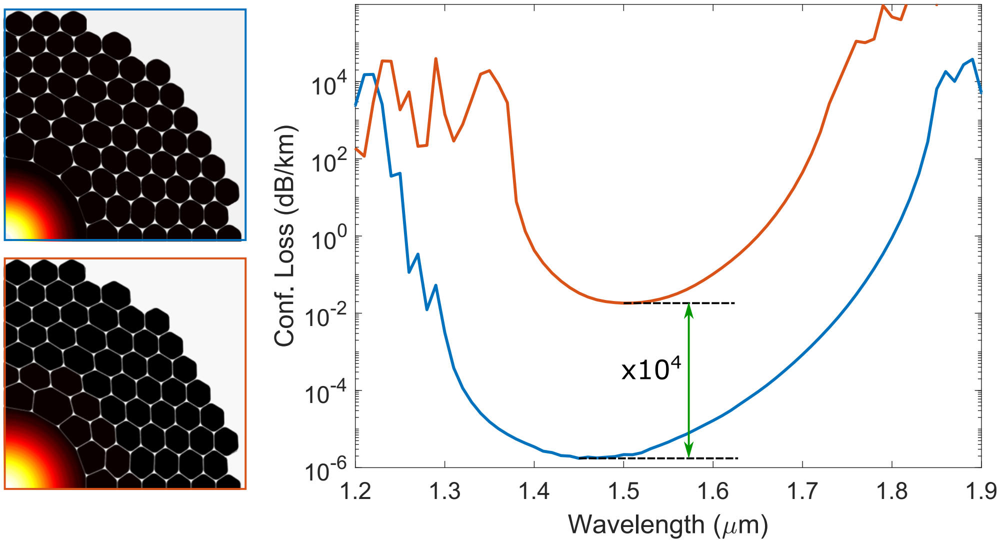

Leakage loss in PBGFs: effect of cladding strut thickness. The two fibers modeled here have the same core diameter of 29.6 μm. The cladding strut is 47 nm thick in the first fiber (blue, other parameters defined in Fig. 7) and 94 nm thick in the second fiber (orange). Note how the extremely low leakage loss (10^{-6} dB/km) in the first fiber increases dramatically with strut thickness.

regions of the cladding. Similarly, for the ARF, we used a maximum mesh element size of $\lambda/4$ in the core region and $t/6$ in the thin glass membranes (see also Ref. [52]). In addition, we used a perfectly matched layer (PML) optimized as described in Ref. [52] to surround the computational domain and to allow the calculation of the leakage loss from the imaginary part of the eigenvalues returned by the mode solver. In PBGFs, increasing the number of cladding rings outside of the hollow core is an effective way to reduce the leakage loss to arbitrarily low levels. As a rule of thumb, each additional ring of cladding air holes reduces the leakage loss by an order of magnitude, which can thus, in principle, be reduced to zero exactly if an infinite number of cladding rings are included. However, the number of cladding rings required to keep the leakage loss at a negligible level is highly dependent on the size of the core and key structural parameters of the cladding, namely the thickness of the glass struts in the cladding and the size of the glass nodes [10,47,80,120]. The interpretation of leakage loss as emanating from coupling between core and lossy cladding modes offers a helpful insight here. Thicker cladding struts make the demarcation between *nodes* and struts difficult. They support modes with higher effective index at the bottom of the bandgap (see Fig. 2), resulting in effect in shallower and narrower photonic bandgaps, and therefore a reduced $\Delta\beta$ between the fundamental core mode and lossy cladding modes. It can be understood alternatively as thicker cladding struts providing more direct pathways for the fields of the core modes to overlap with the cladding radiation modes, thus resulting in loss. To illustrate this point, we show in Fig. 8 the leakage loss calculated for the fundamental mode in two different PBGFs with a 19c core defect. Both fibers have the same core diameter and air-filling fraction. The first is the structure described in Fig. 7 and in the second, the struts are twice as thick, with the size of the cladding nodes adjusted so that the total mass of glass in the cross section is conserved. One can see that with this small readjustment of the cladding structure, the second fiber with thicker struts has a remarkable four orders of magnitude higher leakage loss and a narrower operating bandwidth.

Figure 9

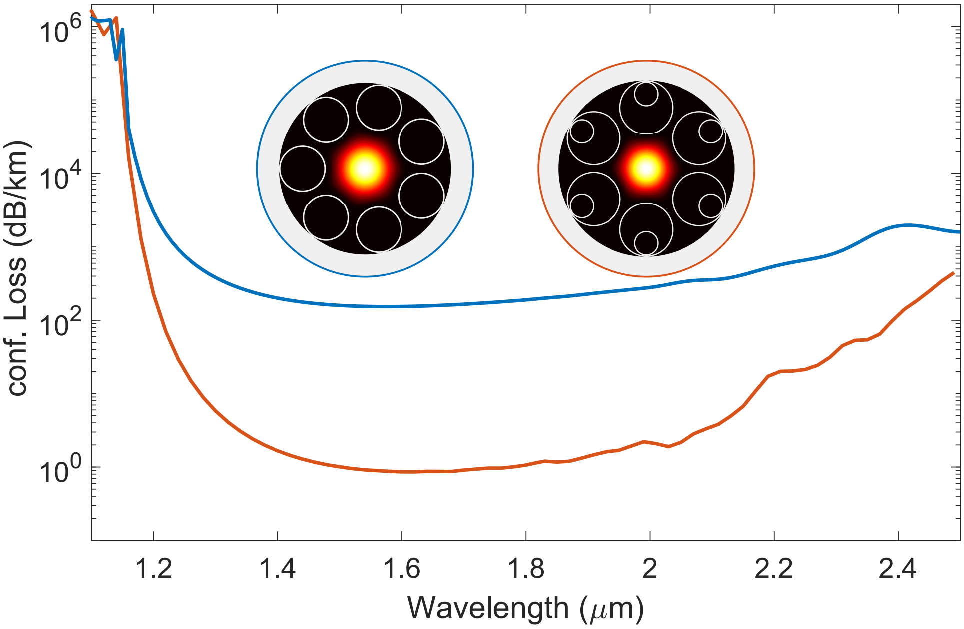

Leakage loss in two example hollow-core ARFs: the first (blue curve) is a seven-tube tubular fiber and the second (orange curve) a six-tube NANF. Both fibers have a core diameter of 30 μm and feature thin cladding tubes with 550 nm thickness. The gap between the tubes in both cases is kept at 3μm, one-tenth of the core diameter.

In ARFs, particularly the widely used tubular and nested variety, away from the resonant wavelengths in the thin glass membranes at which the loss is sharply peaked (as shown in Fig. 6) and away from anticrossing events discussed in the following section, leakage is mediated by the coupling to modes located in the air regions either enclosed by the tubes or the spaces between them, which can easily escape to radiation due to the physical contact with the glass jacket. This important insight provides an explanation as to how the leakage loss can be reduced further or increased for undesirable higher-order core modes. By choosing the size of cladding tubes so that the $\Delta\beta$ between their modes and that of a higher-order core mode is near zero, extremely high loss can be imposed on said higher-order core modes often resulting in effectively single-mode operation as explored in many prior publications [91,136,137]. On the other hand, by partitioning these hollow regions of the cladding and making them smaller, the modes they support would have a larger $\Delta\beta$ with the core modes, resulting in lower leakage loss for the core modes [138]. We plot in Fig. 9 the leakage loss calculated for two ARFs with 30 μm core diameter. The first is a tubular fiber with a cladding made of seven non-contacting tubes and the second is the NANF whose parameters we described in Fig. 7. Both fibers have the same core diameter, gaps between outer tubes and membrane thickness. The computed leakage loss is shown here across the fundamental antiresonance window, i.e., wavelengths longer than the first resonance at 1.1 μm . We can see how the addition of the nested tube results in a dramatic reduction in leakage loss.

2.1d. Role of Modal Anticrossings

In HCFs, the termination of the *cladding* around the central core plays a vital role in determining the leakage loss of the fiber. This is because such a core *boundary* may support optical modes with similar propagation constant to the core modes and which easily radiate directly to lossy cladding or jacket modes. Depending on the symmetry of the modes involved, this can lead to crossings or avoided crossing events (anticrossings) with core-guided modes, resulting in a dramatic effect on the attenuation [105].

In PBGFs, the impact of such *surface* modes was recognized early on. The phenomenological Lorentzian of Eqs. (12) and (13) was derived when studying how these surface modes affect the attenuation of the fundamental mode in the fibers [69,70,139]. As it turns out, the core boundary in PBGFs is an extremely sensitive region which must be designed carefully in order to avoid high leakage loss, the related dramatic reduction in operational bandwidth as well as all other loss contributions [75,140]. Simple prescriptions have been made to this effect, for example, using a core boundary that is half as thin as the cladding struts. This ensures that the modes they support fall outside of the photonic bandgap [57,75–77]. A more complete consideration, however, also showed that the glass nodes at the core boundary must be of the same size as those in the cladding for optimum suppression of surface modes [68]. To illustrate the drastic effect surface modes can have on leakage loss in PBGF, we plot in Fig. 10 the dispersion map for the PBGF of Fig. 7, but where surface modes are introduced deliberately through a three times thicker core wall and also smaller nodes on the core boundary. These modifications result in surface modes that anticross with the fundamental mode near 1.42 µm and also in a markedly increased leakage loss at shorter wavelengths.

In ARFs, the core boundary is an equally critical region which must be designed carefully in order for the leakage to remain low. As discussed previously, the introduction of a *negative curvature* core boundary in Kagomé fibers physically pushes the glass nodes away from the core, reducing the overlap between their modes and the core-guided modes, and resulting in low loss and a smooth transmission spectrum free of spurious peaks [141].

In antiresonant tubular fibers or NANFs, the cladding is made of non-contacting sets of cylindrical glass tubes and there are no glass nodes. However, the thin, tubular glass membranes also support modes of their own. Away from the resonances, the modes supported by the glass membranes have a transverse phase profile of approximately $e^{-im\theta}$ (θ is the angular position around the membrane) that changes rapidly (i.e., large m) and as a result have a vanishingly small overlap with core-guided modes [85,127,142,143]. The loss of the fibers in that region therefore is free of spurious peaks across the transmission bandwidth. However, as we approach the resonance wavelengths particularly from shorter to longer wavelengths the transverse phase of the membrane modes do not change as rapidly. Furthermore, as these membrane modes approach their cutoff, they expand and can have a strong overlap with the core modes, leading to the appearance of peaks in the leakage loss curves as a result. These peaks have the same phenomenological Lorentzian signature described previously, see Refs. [144,145]. The proximity of cladding tubes to one another creates, just as in the tight binding model, a band of allowed membrane modes, as described in Ref. [143]. It is the interaction between core and membrane modes that ultimately limits the useful bandwidth over which low loss can be achieved. We typically find that in ARFs with non-contacting tubular membranes, the spectral loss curve shows spurious peaks in the normalized frequency range $m \leq f \leq m + \frac{1}{2}$ where m is an integer ($f = 2t\sqrt{n^2 - 1}/\lambda$). Such small peaks are visible in the leakage loss plots in Fig. 9 for the NANF of Fig. 7 beyond the wavelength of 2 µm but are less prominent in that of the tubular fiber because of its already higher loss. To further illustrate this, we show the dispersion map for this NANF in Fig. 11 where we plot the normalized effective index $(n_{eff} - 1)\pi^2 f^2$ against the normalized frequency f for the first 50 modes of the fiber solved for with a finite-element mode solver. We also show the computed leakage loss with a finer wavelength resolution where the spurious peaks of the loss curve due to avoided

Figure 10

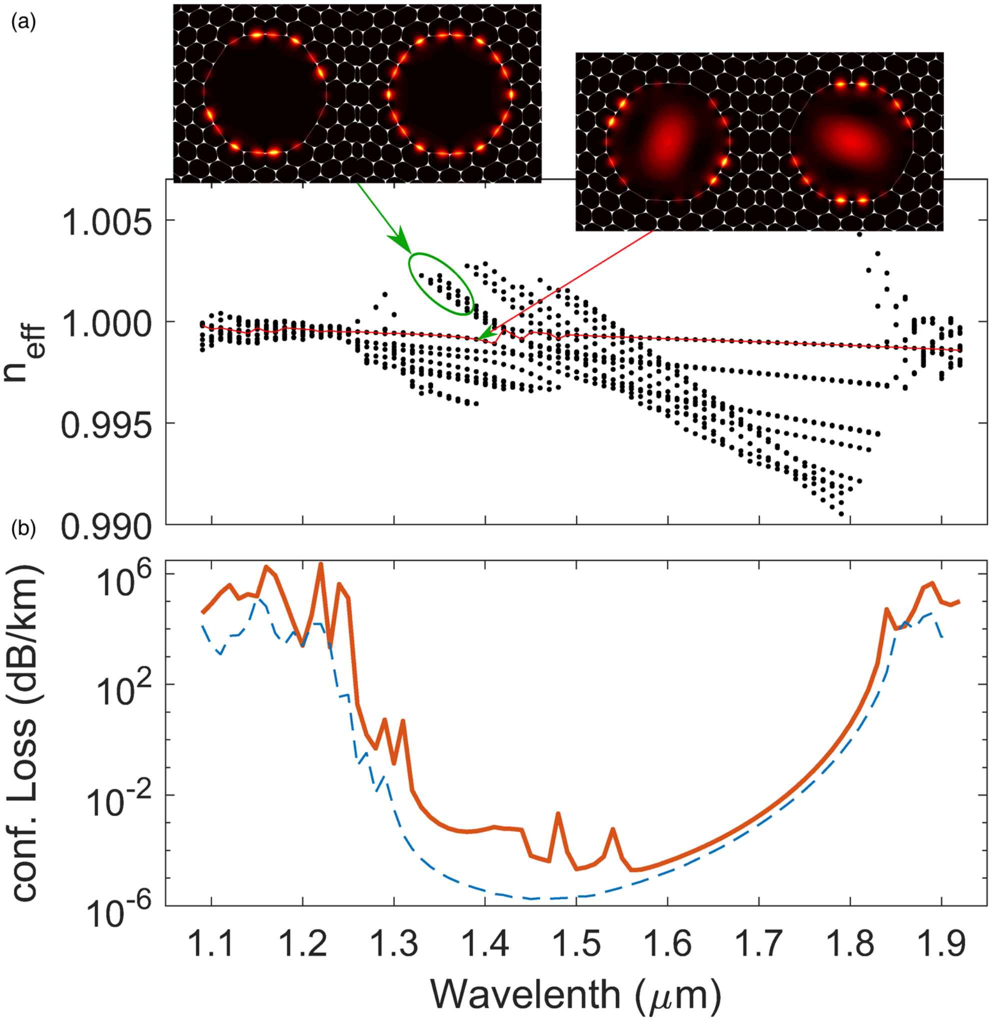

Role of surface modes on the leakage loss of PBGFs: with small modifications of the core boundary (thicker membranes and smaller glass nodes compared with the fiber in Fig. 8), surface modes are introduced and result in an anticrossing event with the fundamental mode near 1.42 μm and a marked increase in leakage loss. (a) Dispersion map as calculated by the finite-element solver; 20 modes are solved for at each wavelength. The highlighted red curve is one of the degenerate fundamental modes for which the leakage loss is plotted in (b). The surface modes (example highlighted in green) can cross or anticross with the dispersion curve for the fundamental mode, leading to the peaks observed in the loss.

crossings is more apparent. One could therefore say that in nodeless ARFs, *surface modes* appear at the long wavelength edge of each transmission window, leaving the short wavelength edge and the middle part of the transmission unaffected, allowing wide operational bandwidths.

It is interesting to note that the small spurious peaks resulting from anticrossings are absent in the loss of a single annular tube waveguide (see Fig. 6) or in the ideal cylindrical nested structures analyzed by Bird [123]. Loss is instead sharply peaked at the resonant wavelengths. This is because in the tube, the number of membrane modes with a non-vanishing overlap with the fundamental core-guided mode is reduced to exactly one by virtue of symmetry.

Figure 11

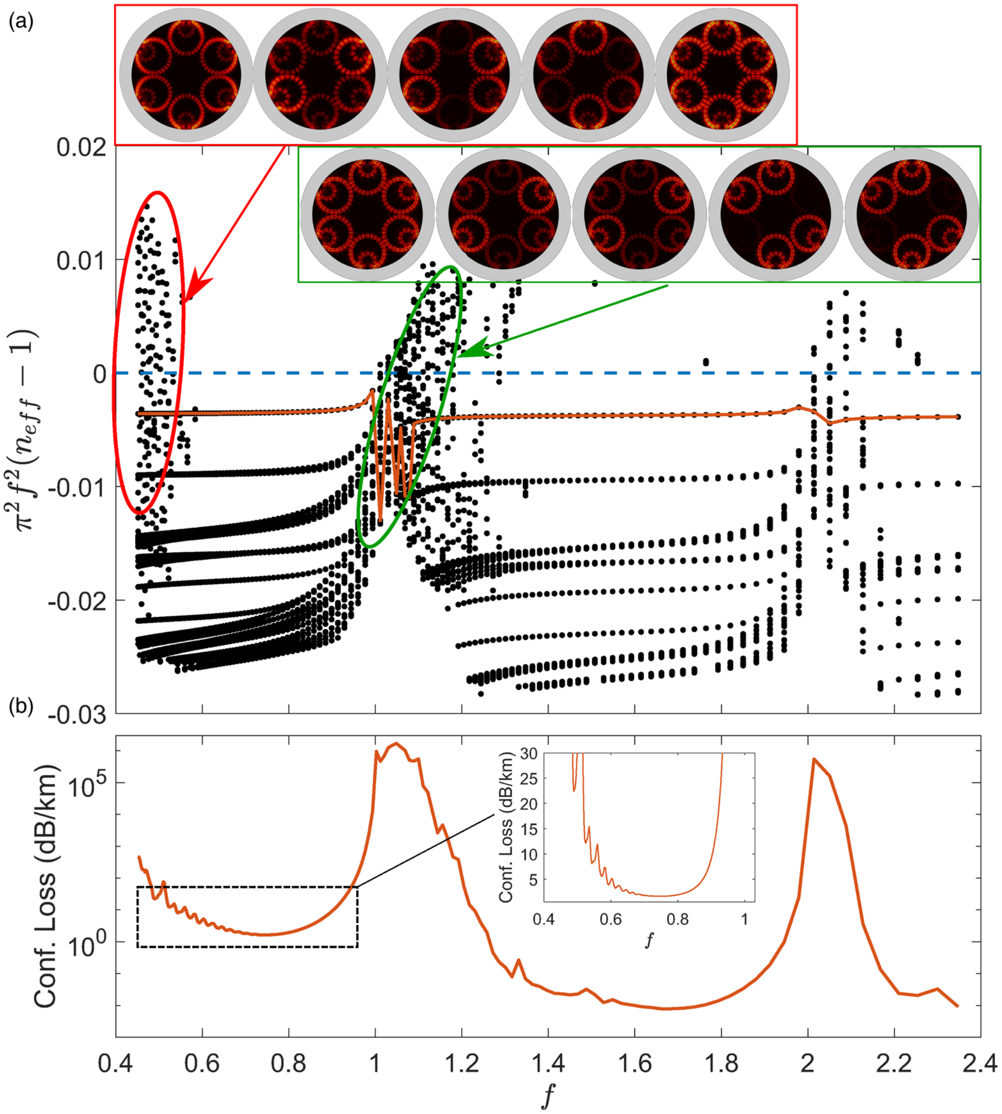

Anticrossing and leakage loss in NANFs: (a) dispersion map plotted as normalized effective index against the normalized frequency. Near the resonant frequencies, the modes supported in the thin glass membranes crossing and anticrossing events with the core-guided modes, in particular the fundamental mode whose curve is highlighted in orange and for which the leakage loss is plotted in (b). Note how the interaction between these glass modes and the core-guided mode leads to peaks in the attenuation near the low-frequency edge of the antiresonance window.

2.1e. Visualizing Leakage Loss

Leakage loss manifests as a non-vanishing radial Poynting flow away from the waveguide mode. As such, tools for visualizing this flow can be extremely useful in providing deeper understanding of its origin and informing the engineering of geometric features of the fiber to further reduce it. Useful insight into the leakage loss, particularly that of ARFs where it is a significant contributor to total loss, can be obtained by examining the radial Poynting flux at the perimeter of the fiber. Resolving it azimuthally allows to link leakage loss to specific geometric features of the fiber. This can be used, for example, to identify the loss contribution due to the asymmetries present in the cross section of a fabricated fiber [115]. As seen in Fig. 12, the azimuthally resolved radial Poynting flux (red curve) for the NANF of Fig. 7 at 1550 nm shows peaks at the position of the tubes, indicating that for this fiber, light escapes from the core predominantly through the tubes and confirming that leakage loss occurs via coupling between core and tube modes. This conclusion changes, for example, if the gaps between the tubes become large, in which case leakage through the gaps becomes important.

Another powerful and useful visualization tool is that of examining transverse power flow streamlines of the guided modes. Streamlines are defined as lines which are always normal to the vector field, as such when they are closely spaced the local power flux is greater than when they disperse. This tool which has traditionally been used in fluid mechanics to map the path followed by an imaginary particle suspended in the flow, has proved useful in identifying routes taken by the optical power lost to radiation. In so doing, it also reveals geometry features which are an effective barrier to such transverse power flow and may thus lead to improved fiber designs with much reduced leakage loss [146–148]. Figure 12 shows the streamlines visualising the transverse power flow for the NANF structure of Fig. 7. The streamlines are seeded in a tight group in the core where the power flux is relatively uniform. Here, we see that the power travel outwards from the core, but as it approaches the cladding tubes, it predominantly flows through the capillaries themselves rather than through the gaps between them. Using this insight, a structure known as antiresonant leakage-inhibited fiber structure (ALIF) was developed to add more radial gaps between capillaries. A nested pair was used instead of a single nested tube and leakage loss was reduced by a factor of 450 [147].

Figure 12

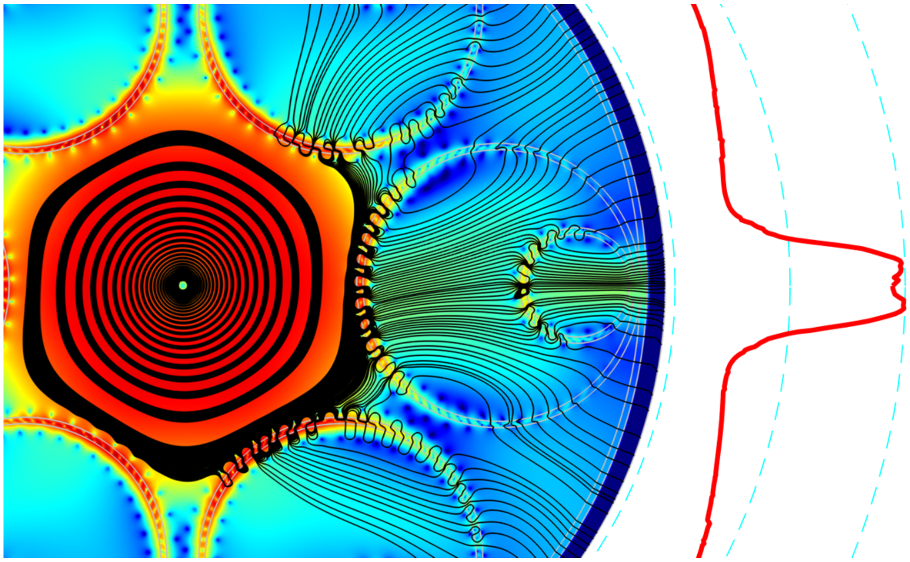

Visualizing leakage loss in NANFs with the use of streamlines following the transverse Poynting vector: the streamlines shown here are seeded near the center of the core and spiral outwards. Dense streamlines indicate stronger power flow. For example, near the outer boundary, the streamlines are denser near the nested element indicating that most of the power escapes through the tubes. The red curve shows the density of power leakage at the outer boundary of the geometry, i.e., the radial component of the Poynting vector as a function of angular position. As can be seen, it further confirms that leakage is highest at the azimuthal position of the tubes.

Figure 13

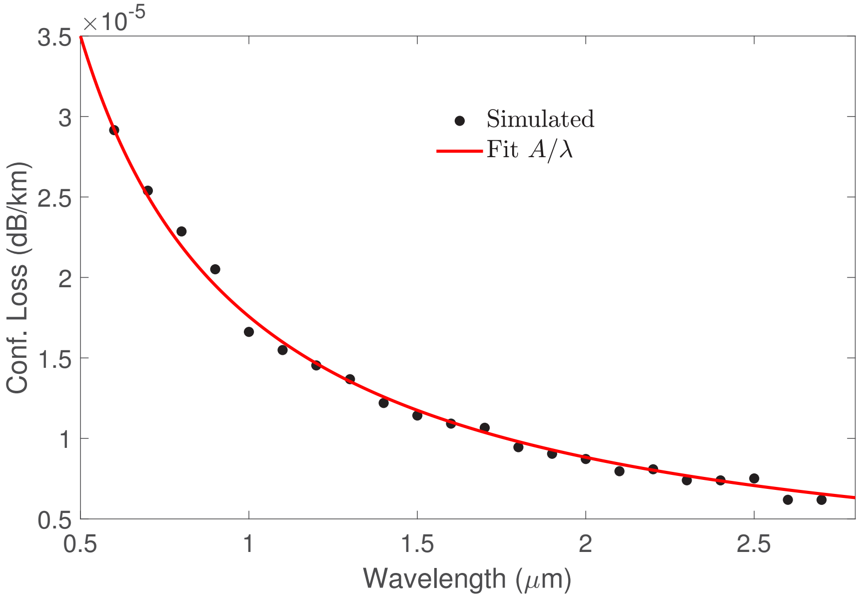

Leakage loss in rigidly scaled PBGFs. As a homothetic scaling is applied to the fiber structure for operation at different wavelengths, the leakage loss is inversely proportional to the wavelength.

2.1f. Scaling Rules

Once a choice of cladding geometry has been made it is useful to establish approximate scaling rules for the leakage loss. Key parameters of interest here are the core size and the wavelength of operation. Such scaling rules are particularly important since other loss mechanisms may scale differently and the trade-offs between them can lead to an optimum region of operation over which the total attenuation of the fiber is the lowest.

In PBGFs, the leakage loss for a single fiber follows a U-shape across the photonic bandgap. As we have discussed, the leakage contribution to loss is, in principle, negligible or can be made so with more rings of air holes outside of the core. Nonetheless, knowledge of how the leakage loss scales with the core size, for example, can help determine the minimum number of cladding rings necessary to maintain it at negligible levels and thus simplify fabrication. It was found that for a given cladding design (cladding pitch, strut thickness, and air-filling fraction), the minimum leakage loss in the photonic bandgap obeys Marcatili and Schmeltzer’s formula and scales approximately as λ^2/a^3 where a is the core radius [10]. Therefore, when the fiber is rigidly scaled to operate at different wavelengths, the leakage loss decreases as $1/\lambda$. We illustrate this in Fig. 13 where we plot the leakage loss for the bandgap fiber shown in Fig. 7, scaled rigidly to operate at wavelengths from 0.6 to 2.5 µm. We have not included material absorption or dispersion, and as can be seen, the leakage loss scales as $1/\lambda$ as expected [149]. In ARFs, leakage is a greater contributor to the total loss of the fiber and how it scales with wavelength and core size is of paramount importance. Scaling rules are more complex, however, as they depend strongly on the choice of cladding parameters and design. In model antiresonant HCFs made of l alternating air/glass layers, Eqs. (10) and (11) first derived by Bird state that to leading order, the leakage loss scales approximately as

$$\alpha_{CL} \propto \frac{\lambda^{l+2}}{a^{l+3}}. \tag{14}$$

Figure 14

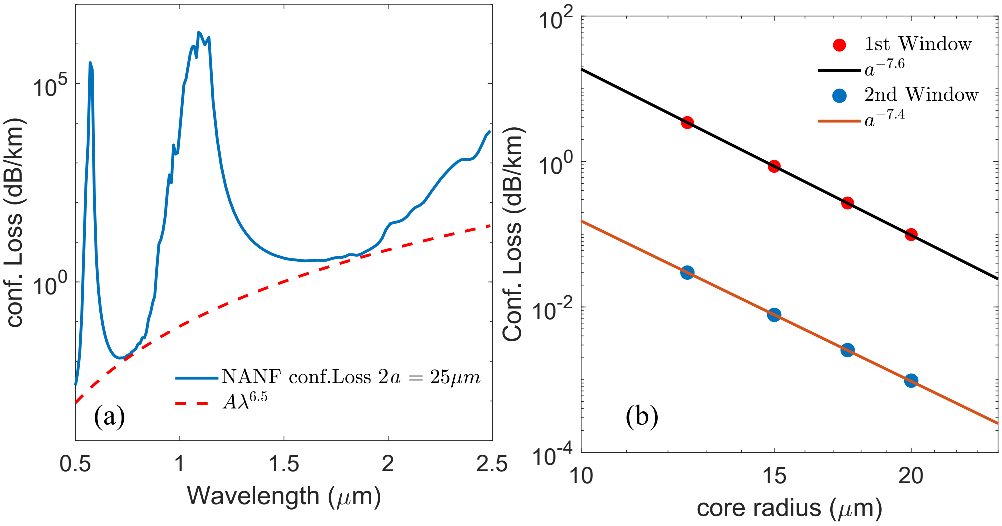

Leakage loss scaling with wavelength and core size in NANFs. In (a), the NANF has the same structural parameters as that in Fig. 9. In (b) we applied a rigid scaling to this structure, maintaining the membrane thickness of 550 nm and a relative inter-tube spacing of $a/5$. The minimum leakage loss scales approximately as $\lambda^{6.5}/a^{7.5}$.

Although practical fibers such as tubular fibers and NANFs differ from these highly simplified model structures, the insight they offer is valuable. In [52], it is shown for an example NANF structure that the minimum leakage loss across antiresonant windows scales approximately as λ^7/a^8, which would be compatible with Bird's formulas for $l = 5$ (three glass membranes and two air layers). However, the exact scaling with core size and wavelength depends on cladding parameters such as the number of tubes, their sizes, and the inter-tube gaps. Furthermore, Eqs. (10) and (11) show the explicit dependence of the loss on the refractive index n as well as the transverse phase accumulated across each layer in the structure ϕ_i which both depend on the wavelength. For the NANF example shown in Fig. 7 with $t = 550$ nm and a gap of $a/5$, we find as shown in Fig. 14 that the loss scales as $\lambda^{6.5}/a^{7.5}$, again conforming approximately to the simplified model derived by Bird for $l = 5$. The addition of nested elements in various configurations therefore not only help reduce the leakage loss, but also how rapidly it scales with wavelength and core size [52,138,147]. For the double-nested fiber we recently reported in Ref. [45], for example, we expect the loss to scale approximately as λ^9/a^{10}. Interestingly, we note from Eq. (14) that if a given ARF design is scaled so that λ/a is constant, then the minimum leakage loss also decreases as $1/\lambda$ as was the case for rigidly scaled PBGFs.

2.2. Light Absorption

Absorption is one of the most fundamental loss mechanisms in optical waveguide. The waveguide's constituent materials absorb light at wavelengths corresponding to transitions between the electronic or ro-vibrational energy levels of its molecules. In fused silica, absorption originates either from electronic transitions in the UV which have an edge in the visible and near-IR (Urbach edge [150,151]), or from vibrations of the silica oxygen bonds at wavelengths longer than about 1700 nm [152]. In addition, the preparation processes of the raw glass material may introduce impurities and related absorption bands. Hydrogen or moisture, for example, react with defect sites in silica to form absorbing species such as chemically bonded hydroxyl groups (OH) with a fundamental absorption band at 2720 nm and a first overtone near 1380 nm

[153,154]. In HCFs, as we show in the following, absorption in the glass material is suppressed by more than four orders of magnitude due to the strong confinement of the mode field in the hollow regions. On the other hand, the environment in these hollow regions may be filled with a gas or a mixture of gases with absorption lines at wavelengths of interest. This section discusses the contribution of absorption to the total loss of the fiber.

2.2a. Absorption in the Glass Membranes

One of the heralded advantages of HCFs is that they can provide low-loss optical guidance in fibers made of highly lossy materials [90]. This property naturally comes from the fact that guidance in the hollow region strongly suppresses the overlap between the guided optical mode field and the solid material. This has led, for example, to HCFs having losses as low as ~40 dB/km in the IR near the 4 μm wavelength where the absorption of the glass material is as high as 860 dB/m, showing more than a 20,000-fold suppression of absorption [112].

Mathematically, when the material is absorbing, we can calculate the resulting loss penalty incurred by the optical mode $|\psi_k\rangle$ through a perturbation treatment. Let us consider that the absorption in the material is quantified through an absorption coefficient α_{bulk} per meter. This correspond to the addition of a small imaginary component to the refractive index given by $-j\alpha_{bulk}/2k_0$ and by extension to a small imaginary part to dielectric constant $-j\delta\varepsilon = -jn\alpha_{bulk}/k_0$. From first-order perturbation theory, one can show that the purely imaginary correction to the propagation constant of mode $|\psi_k\rangle$ is [54,155,156]

$$\begin{aligned}\Delta\beta_k &= -j\frac{\omega}{c}\,\langle\psi_k|\delta\varepsilon|\psi_k\rangle \\ &= -j\iint_{A_\infty} |\mathbf{E}_k|^2\, n\alpha_{bulk}\, dx\, dy,\end{aligned} \tag{15}$$

where the modes are normalized to obey the orthonormality condition [54,157–159]:

$$\iint_{A_\infty} \vec{z}\cdot\left(\mathbf{E}_k\times\mathbf{H}_l^* + \mathbf{E}_l^*\times\mathbf{H}_k\right)\, dA = \delta_{kl}. \tag{16}$$

Here, $\mathbf{E}_k$ and $\mathbf{H}_k$ are the electric and magnetic field vectors of the mode $|\psi_k\rangle$. For the absorption in the glass material alone, the integral of Eq. (15) extends only in the glass region in the fiber's cross section. If the absorptive perturbation is further considered constant in the glass, the absorption loss is simply

$$\alpha_{abs} = -2\Im(\Delta\beta_k) = 2\alpha_{bulk}\iint_{glass} |\mathbf{E}_k|^2\, ndxdy = \zeta\alpha_{bulk}. \tag{17}$$

Clearly, the glass absorption is suppressed by a factor ζ given by

$$\zeta = \frac{\alpha_{abs}}{\alpha_{bulk}} = 2\iint_{glass} |\mathbf{E}_k|^2\, n\, dx\, dy. \tag{18}$$

In other words, the absorption in the glass is suppressed by a factor proportional to the fraction of the normalized $|\mathbf{E}_k|^2$ in the glass material, as also derived elsewhere [160]. In HCFs, the absorption in the glass is suppressed by a few orders of magnitude as compared with bulk. For the optimized 19c PBGF shown in Fig. 7, we calculated ζ across the photonic bandgap and plot the results in Fig. 15, obtaining a minimum value of the order of 400 parts per million (corresponding to an absorption suppression factor $1/\zeta$ of 2.5×10^3). In the NANF of Fig. 9 which has a similar core size, we find a minimum ζ value of 90 parts per million (suppression factor of $\sim10^4$) in the first antiresonant window, about 4.5 times smaller than the PBGF.

Figure 15

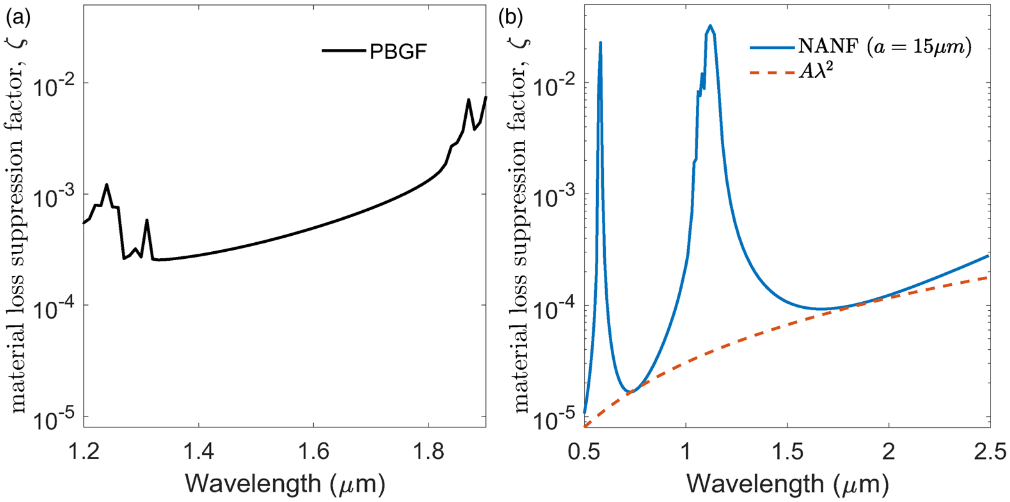

Glass absorption and bulk scattering loss suppression factor in the (a) PBGF and (b) NANF of Fig. 7. With our choice of design parameters, ζ in the PBGF increases with wavelength across the bandgap, going from 250 ppm at 1.4 µm to 2000 ppm at 1.8 µm. Here ζ is lower in the NANF with minima of 90 ppm and 18 ppm in the first and second windows, respectively. The minima across antiresonant windows increases roughly as λ^2.

The value by which glass absorption is suppressed, i.e., $1/\zeta$, evidently depends on the core size, the wavelength, and the design of the cladding, as one may expect. For example, in NANFs with larger core diameters and thinner membranes such as that reported in Ref. [115], the typical value for ζ is 40–50 ppm in the first window and 10–20 ppm in the second. We can derive a first-order scaling rule of ζ with core diameter, wavelength, and membrane thickness by considering the simple tube waveguide such as that shown in the inset of Fig. 6. At wavelengths away from the edges of the transmission windows, the field near the core boundary scales approximately as λ/a [54,121,161]. When normalized according to Eq. (16), the field at the interface is further divided by a quantity proportional to $\sqrt{\text{mode area}} \propto a$ so that the normalized field at the interface scales as λ/a^2. As the integral of Eq. (18) is performed over an area roughly equal to the product of the core boundary circumference and the membrane thickness. It follows therefore that to first order, the factor ζ scales as

$$\zeta = \frac{\alpha_{abs}}{\alpha_{bulk}} \propto \left(\frac{\lambda}{a^2}\right)^2 \cdot a \cdot t \propto \frac{\lambda^2 t}{a^3}. \tag{19}$$

We have found that this scaling rule derived for a thin tube of radius a and thickness t holds approximately for ARFs like tubular fibers and NANFs. In Fig. 15, we show the approximate λ^2 scaling for the NANF of Fig. 7. This scaling relation derived from first principles here is similar to the empirical one found by Vincetti through fitting numerical simulations of tubular fibers [144]. To first order, the scaling is independent of the exact geometry of the fiber, which does not come as surprise given that most of the field confined in the glass is located in the membranes closest to the core.

Equation (19) can be used to estimate the contribution to loss from glass absorption for fibers operating at different wavelengths without the need for computationally expensive finite-element simulations. For example, using the ζ values calculated for the PBGF in Fig. 15, we can see that if this fiber is rigidly scaled to shift the bandgap to different wavelengths, i.e., both λ and the fiber's geometrical parameters are scaled

Figure 16

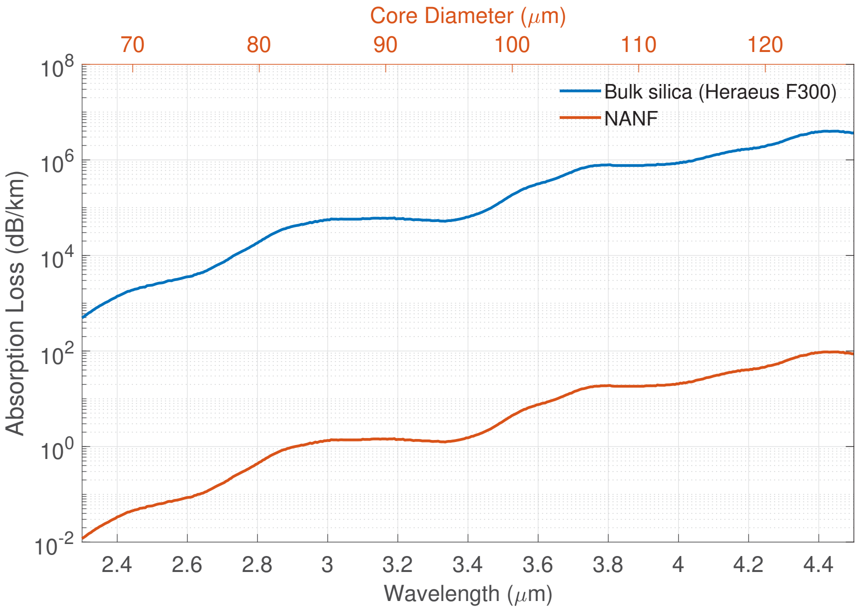

Calculated glass absorption loss in rigidly scaled NANFs. For the example shown here, we have chosen $a/\lambda = 19.35$ and $a/t = 86$. At 4 µm, with a core diameter of 113 µm, absorption loss can in principle be reduced to only 20 dB/km. Reported values stand at 40 dB/km in a tubular design [112].

in proportion, then ζ does not change appreciably with wavelength, particularly if dispersion is neglected [52].

Equation (19) also points to an important insight as to why in spectral regions where the material is highly absorptive, ARFs have the potential to outperform their PBGF counterparts. This key advantage is the freedom, at any chosen operating wavelength, to flexibly change the core size while keeping the cladding membrane thicknesses constant. For example, doubling the core size results in absorption being reduced by a factor of eight if the thickness and cladding design are kept the same. In contrast, although enlarging the core of PBGFs by removing a greater number of unit cells to make the core defect is in principle feasible, it has proved extremely challenging to do in practice and the most successful embodiment at all reported wavelengths are fibers with 19c core defects. It is no surprise that the lowest loss fibers at wavelengths beyond about 2 µm or below 1 µm are of the antiresonant type [108] (see Fig. 5).

Despite the orders of magnitude suppression of glass absorption, this loss contribution can become the dominant contribution to HCF loss in the mid-IR where silica's absorption is higher than 10 dB/m. In Fig. 16, we plot the predicted minimum absorption loss for rigidly scaled NANFs operating at wavelengths between 2.4 and 4.4 µm. For these calculations, we chose a core size to thickness ratio $a/t \sim 86$, giving a minimum value $\zeta = 2.4 \times 10^{-5}$ in the first antiresonant window. The loss of bulk silica at these wavelengths is extracted from the data provided by Heraeus [162]. We see that despite the high loss of the silica material (>1000 dB/m), for our design restriction, <100 dB/km fiber loss is possible up to 4.5µm [112,160]. We project that, for example, at 7µm where glass attenuation is 60 dB/mm (not shown here), a fiber with a core diameter of 200 µm and a membrane thickness of 2.3 µm would have an absorption loss of 1.4 dB/m, making low-loss guidance possible for a wide range of applications across the mid-IR.

2.2b. Absorption from Gases in the Hollow Regions

In applications such as gas-based photonics where relatively short lengths of fiber are required, the exact composition of the gas inside the core is often carefully controlled [35]. In contrast, in telecommunication applications, for example, where light is transmitted over tens of kilometers of fiber, little attention has traditionally been paid to the control of the gaseous mixture inside the hollow regions of the fiber. Yet, if present, gas species in the hollow regions can affect the performance of the fiber and also contribute to attenuation.

Although few studies have been devoted to the composition of gases inside HCFs when not intentionally controlled, a number of publications have reported observation of atmospheric gas species such as water vapor and carbon dioxide [163,164] and other gas species such as hydrogen chloride [86,111,112,164,165]. The presence of atmospheric gas species originates from ingress of atmospheric gases into the fiber post-fabrication if its ends are left open. This, it is now understood, is facilitated by the lower pressure inside the fiber immediately after fabrication [166,167]. The presence of gas species such as hydrogen chloride is thought to arise from remnants of halogenated precursors employed in the production of the fused silica used to make HCF preforms [86,112].

Molecular gases present within the hollow regions of the fiber affect the fiber attenuation through direct absorption, whether from direct electronic transitions or from roto-vibrational transitions [164]. In the literature, gas absorption has featured more prominently in fibers designed to operate in the mid-IR, the so-called fingerprint region. For HCFs operating at wavelengths between 1 and 1.8 μm, the absorption band around 1.4 μm often features prominently (see, for example, Refs. [45,115]). This feature originates from the hydroxyl ions in the silica, but may also come from atmospheric water vapor [168].

The contribution of gas absorption to loss in HCFs is not fundamental and, when present, can be eliminated by improvements in the fabrication process, for example, through the use of different precursors in the preparation of the raw glass material or, as has been shown, by additional post-fabrication processing steps such as purging with inert gases [86,111].

2.3. Loss from Bulk Scattering

In addition to absorption, light propagation in optical waveguides experiences Rayleigh scattering which arises because of the intrinsic microscopic inhomogeneity present in most optical materials. In HCFs, Rayleigh scattering contributions to loss come from the glass material as well as from potential gases with which the hollow regions of the fiber may be filled.

One approach to calculating the contribution from Rayleigh scattering is to consider that the inhomogeneities resulting from thermodynamic density fluctuations are effectively equivalent to a small, real perturbation to the dielectric permittivity $\Delta\varepsilon(x, y, z)$. A perturbation treatment can then be used to estimate the total power scattered as a result of such perturbation (see, for example, Ref. [161]). A more intuitive estimate of the contribution from Rayleigh scattering can be made by realising that the Rayleigh loss coefficients for most constituent materials of the HCF are well known. One can thus regard this well-known loss as equivalent to a small absorption, i.e., a small imaginary perturbation to the dielectric constant. The same conclusions from the previous section therefore follow logically.

2.3a. Scattering in the Glass Membranes

It follows from the preceding section that, like absorption, the contribution to loss from bulk scattering in the glass is expected to scale approximately as the material loss suppression factor ζ. Taking the Rayleigh scattering contribution of pure silica as $\alpha_R = 0.11 \times (1.55/\lambda\ [\mu\text{m}])^4$ [152], it follows that the loss contribution from bulk scattering in glass is proportional to

$$\alpha_{sc} = \zeta\alpha_R \propto \frac{\lambda^2 t}{a^3} \cdot \lambda^{-4} \propto \frac{\lambda^{-2} t}{a^3}. \tag{20}$$

For rigidly scaled fibers, scattering therefore scales with wavelength as λ^{-4}. However, the small values of ζ make the contribution from bulk scattering negligible. For the example NANF structure of Fig. 7, the Rayleigh scattering in the glass contributes approximately 10^{-5} dB/km at 1550 nm to the loss. If this fiber is scaled rigidly to operate at 100 nm, Eq. (20) indicates that the contribution increases to 0.6 dB/km only and is therefore safe to be neglected.

2.3b. Scattering from Gases in the Hollow Regions

When the hollow regions of the fiber are filled with a gas, a small Rayleigh scattering contribution to loss may be expected. Because nearly all of the optical field is confined in the hollow regions, this scattering loss contribution is given by the Rayleigh scattering coefficient of the filling gas. Assuming that the hollow regions of the fiber are filled with air at room temperature and atmospheric pressure, the effective Rayleigh scattering coefficient in the hollow regions is 4.7×10^{-3} dB·µm^4/km (see Ref. [169]), meaning that at 1550 nm, Rayleigh scattering loss is approximately 8×10^{-4} dB/km. Although this increases linearly with the gas pressure, it still amounts to a negligible contribution to loss and can safely be neglected.

2.4. Loss from Surface Scattering

In any optical waveguide, perturbations on boundaries between constituent materials can lead to additional contributions to loss, particularly when the amplitude of the guided optical mode field near such boundaries is high or the refractive index contrast between the constituent materials large [119,170–172]. This is the case for HCFs as their structure incorporates multiple air–glass interfaces which possess intrinsic roughness of thermodynamic origin [73]. Surface contributions to loss originate from scattering when the material boundaries are perturbed along the length of the fiber, for example by the intrinsic roughness, or from absorption and scattering when potential impurities are adsorbed on the surfaces.

One fundamental mechanism giving rise to intrinsic roughness on air–glass interface in HCFs is that of frozen-in surface capillary waves [73]. As is the case on the surface of any heated liquid, thermally excited capillary waves exist on the surface of molten glass under the restoring force of surface tension. As molten glass goes through solidification, these surface capillary waves freeze in, giving rise to an intrinsic surface roughness. In Ref. [49], Roberts *et al.* argued that it is scattering from this intrinsic surface roughness that imposes a fundamental limit on loss in HC-PBGFs. In this section, we examine the loss contribution from light scattering at the air–glass interfaces within HCFs.

2.4a. Rigorous Theoretical Treatment

Traditionally, the tools of choice for calculating loss originating from perturbations to material boundaries such as surface roughness within waveguides have been coupled-mode theory methods [119,171,173–179]. However, such tools require knowledge of the infinite set of radiation modes of the fibers in order to accurately estimate loss, making these methods challenging for use in microstructured fibers. An alternative method of estimating scattering loss is to consider that the fields scattered by each perturbation *bump* interfere coherently in the far-field [180]. This approach is generalized here using the so-called the volume-current methods [181–184].

Figure 17

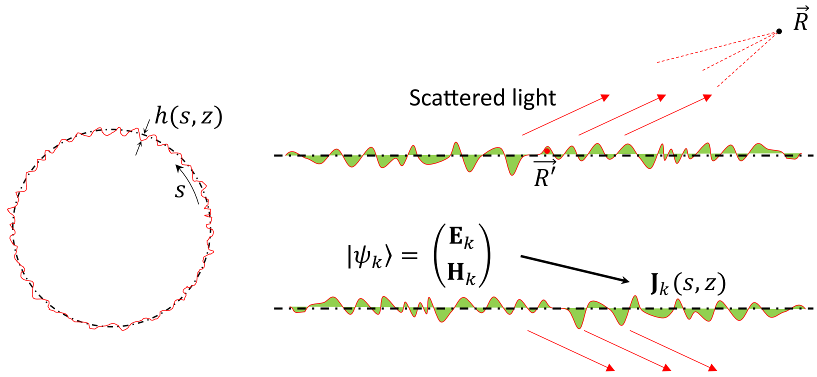

Schematic illustration of the process of roughness scattering in a HCF.

Let us consider that the mode $|\psi_k\rangle$ is propagating through a fiber section of length L, long enough to contain all the relevant features of the perturbations, but also short enough to assume the mode does not suffer significant loss. This is illustrated schematically in Fig. 17. We first compute the current density induced by the presence of the surface inhomogeneities within this section of the waveguide, and from it the far-field distribution of the radiated field and thus loss. Describing the geometric perturbations caused by roughness on the air–glass interfaces with a small, zero-mean, deviation $h(s,z)$ (s is a curvilinear coordinate along the relevant interface in the cross section) assumed not to change the local surface normal nor the refractive index, the induced current density at a point (s,z) can be expressed as [161,172,185]

$$\mathbf{J}_k(s,z) = -j\omega\varepsilon_0\left(\Delta\varepsilon_r\mathbf{E}_{\parallel k}(s,z) - \Delta\frac{1}{\varepsilon_r}\mathbf{D}_{\perp k}(s,z)\right)h(s,z). \tag{21}$$

Here, $\Delta\varepsilon_r = n_{glass}^2 - 1$, $\Delta 1/\varepsilon_r = 1/n_{glass}^2 - 1$, and $\mathbf{E}_{\parallel k}$ and $\mathbf{D}_{\perp k}$ are the components of the electric field parallel to the interface and the component of the electric displacement normal to the interfaces, respectively. By using only field expressions continuous across the interface, this expression ensures the current density is not ill-defined and does not depend on the side of the interface on which it is computed. Making the approximation that this induced current radiates in free space, the electric and magnetic field vectors at a location defined by position vector $\vec{R}$ on a far-field sphere centered on the section of the fiber under analysis are given by [181,186]

$$\mathbf{E}_s(\vec{R}) = -jk\frac{\mathrm{e}^{jkR}}{4\pi R}\left(\vec{r}\times\int_V \mathrm{e}^{-jk\vec{r}\cdot\vec{R}'}\mathbf{J}_k(s,z)\,dV\right) \tag{22}$$

$$\mathbf{H}_s(\vec{R}) = -j\omega\mu\frac{\mathrm{e}^{jkR}}{4\pi R}\vec{r}\times\left(\vec{r}\times\int_V \mathrm{e}^{-jk\vec{r}\cdot\vec{R}'}\mathbf{J}_k(s,z)\,dV\right), \tag{23}$$

where $\vec{r} = \vec{R}/R$ and $\vec{R}'$ is the location of the perturbation within the fiber. The integration extends over the total volume containing the perturbed waveguide section. We can shorten the integrand in these expressions by writing

$$\begin{aligned}\vec{r}\times\mathbf{J}_k(s,z) &= -j\omega\varepsilon_0\left(\Delta\varepsilon_r\vec{r}\times\mathbf{E}_{\parallel k}(s,z) - \Delta\frac{1}{\varepsilon_r}\vec{r}\times\mathbf{D}_{\perp k}(s,z)\right)h(s,z)\\ &= -j\omega\varepsilon_0\vec{U}_k(s)\mathrm{e}^{-j\beta_k z}h(s,z),\end{aligned} \tag{24}$$

where we have used $\mathbf{E}_k(s,z) = \mathbf{E}_k(s)\mathrm{e}^{-j\beta_k z}$, β_k being the propagation constant of the mode $|\psi_k\rangle$. The Poynting vector of the scattered field at the observation point is then given by

$$\begin{aligned}\mathbf{S}_k(\vec{R}) &= \frac{1}{2}\left\langle \mathbf{E}_s(\vec{R}) \times \mathbf{H}_s^*(\vec{R}) \right\rangle \\ &= \frac{\omega^4 \varepsilon_0^2 \mu}{32\pi^2 R^2 c}\vec{r} \int_V \int_V \langle h(s', z') h(s, z)\rangle\, \vec{U}_k(s) \vec{U}_k^*(s') \mathrm{e}^{-j\beta_k(z-z')} \mathrm{e}^{jk\vec{r}\cdot(\vec{R}'-\vec{R}'')},\end{aligned} \tag{25}$$

where $\langle \cdots \rangle$ represents an ensemble average. Equation (25) can be further simplified when the roughness autocorrelation $\langle h(s', z') h(s, z)\rangle$ can be expressed as a product of functions of $s - s'$ and $z - z'$. The roughness resulting from frozen-in thermally excited capillary waves is non-separable with respect to the longitudinal direction and that along the perimeter, making the evaluation of the integral in Eq. (25) complicated [48,73]. We argue, however, that in HCFs, the most important features of the roughness, especially those dictating the angular distribution (with respect to the polar angle with the fiber axis) of the scattered light are those along the fiber axis (see also Ref. [49]). Using a spherical coordinate for the far-field point $\vec{R}$ (R, θ, ϕ) and a cylindrical coordinate for the location $\vec{R}'$ (ρ', ϕ', z) of the perturbation, we have $\vec{r} \cdot \vec{R}' = z\cos\theta + \rho' \sin\theta \cos(\phi - \phi')$. With this, the far-field Poynting vector becomes

$$\mathbf{S}_k(\vec{R}) = \frac{\omega^4 \varepsilon_0^2 \mu}{32\pi^2 R^2 c} L \tilde{\psi}\,(\beta_k - k\cos\theta)\, \vec{r} \sum_m \left| \oint_{C_m} \vec{U}_k(s) \mathrm{e}^{jk(\rho' \sin\theta \cos\phi - \phi')}\, ds \right|^2. \tag{26}$$

Here, we have assumed that the roughness on each glass interfaces labeled m is statistically independent. In other words, the physical process giving rise to roughness is the same, but the roughness on each interface is independent of the others. The roughness on each interface does, however, have the same power spectral density (PSD) in the z direction defined as

$$\tilde{\psi}\,(\Delta\beta) = \int_0^L \langle h(z') h(z)\rangle\, \mathrm{e}^{-j\Delta\beta(z-z')} d(z - z'). \tag{27}$$

Equation (26) is essentially the same result we derived previously in Ref. [180], but is more general and without the approximations on the dipole polarizability. Equation (26) can be evaluated from the mode-field data obtained by commercial finite-element solvers such as COMSOL Multiphysics, with an overhead on computation time that depends on the resolution in θ and ϕ on the far-field scattering sphere. Figure 18 shows plots of the calculated far-field scattering pattern for the fundamental modes of the PBGF and NANF of Fig. 7. To display features of the scattering pattern, we assumed here a PSD $\tilde{\psi}\,(\Delta\beta) = 1$. As may be expected, the more complex structure of the PBGF leads to a richer scattering pattern in the far-field, where contributions from the glass nodes on the core boundary for example are visible as hotspots in the scattered field distribution. In NANFs, in contrast, one only sees that the far-field scattering pattern reflects the sixfold symmetry of its structure.

When the PSD of the roughness is known, the surface scattering loss rate from the fiber is obtained as

$$\alpha_{ssc} = \frac{1}{L} \frac{\displaystyle\int \vec{r} \cdot \mathbf{S}_k R^2\, d\Omega}{P_k}, \tag{28}$$

where the integration is carried over the 4π solid angle and P_k is the power carried by the incident mode, expressed as the integral of a Poynting flux as in the previous section.

Figure 18

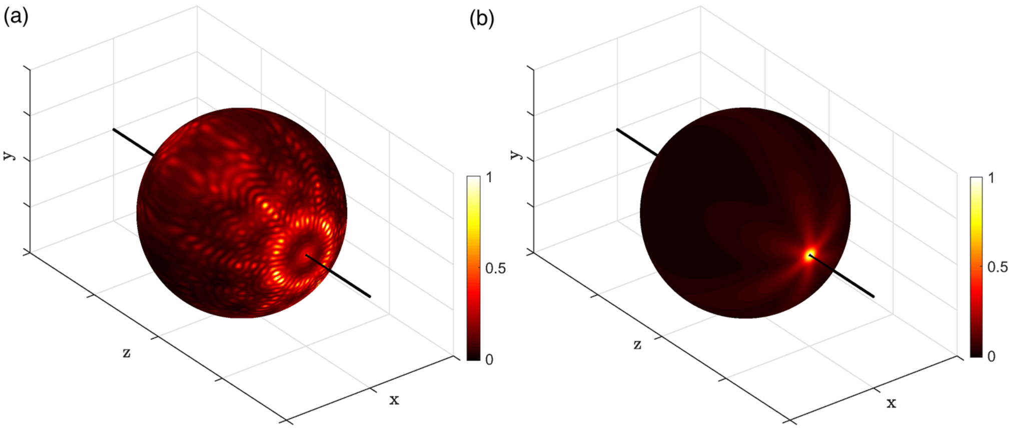

Normalized far-field distribution of the roughness-scattered power in the (a) PBGF and (b) NANF of Fig. 7 as computed from Eq. (26). The more complex structure of the PBGF reveals a richer scattering pattern, whereas the sixfold symmetry of the NANF is clearly reflected in its scattering pattern.

2.4b. Intrinsic Roughness of the Air–Silica Interfaces

It is now well known that the air–glass interfaces in microstructured optical fibers possess a fundamental and intrinsic surface roughness originating from thermally excited surface capillary waves which are frozen-in during the fiber draw [49,73]. Such roughness has been thoroughly investigated on the surfaces of horizontally formed thin glass films [73,187]. In such a scenario, gravity provides a dampening force to the excited thermal capillary waves on the liquid glass surface, leading to a 2D PSD of the form

$$\tilde{\psi}_{2D}(\kappa) = \frac{k_B T_g}{\rho g + \gamma|\kappa|^2}, \tag{29}$$

where κ is the 2D surface wave vector, ρ the glass density, and g the gravity constant. Here k_B is Boltzmann's constant, T_g is the glass transition temperature, and γ is the surface tension of the glass.

In the case of HCFs, the surfaces are typically closed in one direction (in the cross section) rather than flat and are made under an imposed vertical flow. Therefore, gravity does not play the same role as a dampening force. It remains unclear if the applied pressure differentials provide a similar restoring force. As the surfaces in fibers are closed in one direction, the surface capillary wave roughness is quantized along the coordinate on the hole perimeter in the cross section and can be expressed as an infinite Fourier series which is then summed to yield the roughness PSD in the longitudinal direction [48,49]. For loss estimates in this paper, we take this longitudinal PSD as [71,180]

$$\tilde{\psi}_{1D}(\kappa) = \frac{k_B T_g}{4\pi\gamma\sqrt{\kappa_c^2 + \kappa^2}}, \tag{30}$$

where we have introduced a low spatial frequency cutoff κ_c to avoid divergence at long spatial wavelengths where $\kappa \rightarrow 0$. Although such a cutoff for horizontal surfaces arises because of the above-mentioned restoring effect of gravity, its origin on the surfaces in HCFs is not yet known. It is worth mentioning however that atomic force microscopy (AFM) measurements performed in one dimension along the fiber axis in PBGFs revealed that the roughness was compatible with Eq. (30), but with surface tension $\gamma = 1 J \cdot m^{-2}$, more than three times higher than the value traditionally quoted for silica $\gamma = 0.3$ J m^{-2} [49,188–191]. Recently, 2D AFM measurements have shown

Figure 19

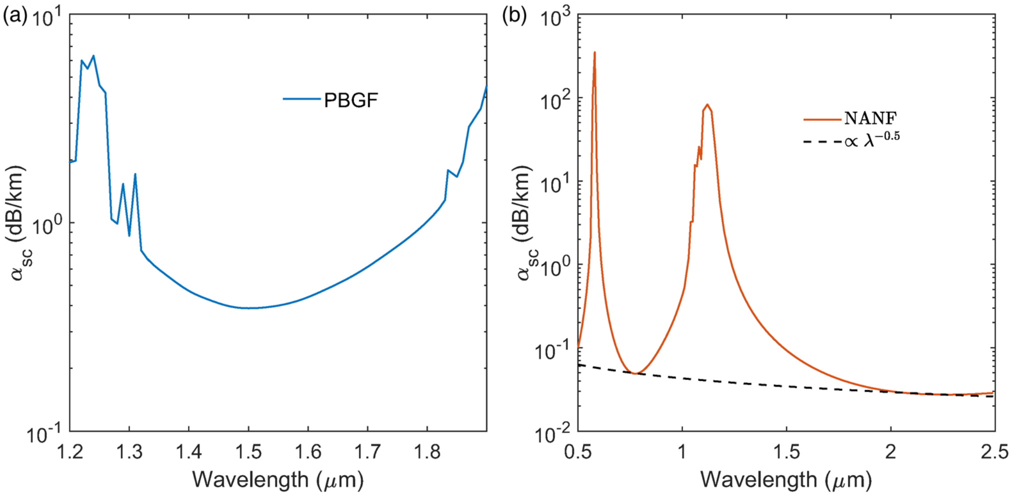

Rigorous scattering loss calculations for the (a) PBGF and (b) NANF of Fig. 7. It is assumed that the roughness present on the air–glass interfaces is the same and limited to the fundamental frozen-in surface capillary waves roughness. This results in the minimum loss in the PBGF (0.4 dB/km) being roughly a factor of 15 higher than in the NANF (0.027 dB/km). Note that for this particular NANF, the minimum loss across windows scales weakly with wavelength, decreasing approximately as $\lambda^{-0.5}$. This scaling is subject to both the exact structure of the fiber (number of tubes, gap between them) and the choice for spatial frequency cutoff for the roughness PSD.

that the externally applied draw stress during the manufacturing process results in attenuated roughness along the axial direction where such stress is applied [192]. This is compatible with earlier measurements showing a higher surface tension than in float glass thin films. For this reason, we use the following widely accepted parameter values to estimate the loss: $T_g = 1500$ K, $\gamma = 1$ J m^{-2}. For the spatial frequency cutoff, it is reasonable to assume that it corresponds to a length scale of the order of the perimeter of the air–glass interface in the cross section. For the remainder of the paper, we use the value $\kappa_c = 2\pi/100\mu m$ (i.e., slightly longer than the perimeter of the typical air–glass interface).

2.4c. Comparing Scattering Loss in Bandgap and ARFs

Inserting the roughness PSD of Eq. (30) into Eqs. (26) and (28), we calculate and plot in Fig. 19 the scattering loss of the fundamental mode of the 19c PBGF and NANF of Fig. 7 across their transmission windows. With the surface roughness parameters described previously, we calculate a scattering loss of 0.4 dB/km for the 19c fiber and only 0.067 dB/km in the NANF at 1550 nm. The minimum scattering loss for the NANF occurs at the longer wavelength of 2.2 μm, and is only 0.027 dB/km (note that 2.2 μm is the antiresonance wavelength in the first window). For the NANF, we note the slower decrease of the minimum loss with wavelength across the antiresonant windows ($\sim\lambda^{-0.5}$, see the following section for a discussion).

The significantly lower scattering loss in a NANF comes as no surprise, given that antiresonance guidance results in much reduced mode-field intensity near the air–glass interfaces (further discussion is given in the following). For the PBGF in which the loss is widely acknowledged to be limited by surface scattering, the loss value we calculate is roughly one order of magnitude lower than the best value reported in surface-mode free fibers operating at 1550 nm [78]. For the fiber reported in Refs. [18,78], with a core diameter of 26 µm and a hole diameter to pitch ratio of 0.97, we calculate a scattering loss of approximately 2 dB/km (see Ref. [180]). Its measured loss via cutback revealed a minimum loss of 3.5 dB/km at 1500 nm. The discrepancy between measured and calculated values was first thought to originate either from inaccuracies in reproducing fiber cross sections for the numerical modeling, or from the uncertainty regarding the surface roughness itself (e.g., it was shown in Ref. [18] that modeled loss matched measurements for $Tg/\gamma = 2900$). However, it is increasingly clear that the underlying assumption that surface roughness scattering alone was responsible for the measured attenuation in PBGFs did not always hold. By inducing power transfer between the guided and radiation modes, other structural perturbations such as microbending (which we examine in Section 3.1) can lead to increased attenuation [193–195]. It is crucial to take such contributions into account in order to build a complete picture of loss in HCFs and help guide the design of ultralow-loss fibers.

2.4d. Scaling Rules

For the purpose of optimizing fiber designs, it is of primary interest to examine how the surface scattering loss scales with key fiber design parameters such as core size and operating wavelength. Such scaling rules are needed to help quickly determine which fiber designs are likely to offer the lowest possible loss for a chosen wavelength of operation. Although the scattering loss at each wavelength ultimately depends on the precise mode field distributions within the fibers and near the air–glass interfaces in particular, useful simplifications can be made. This is because to first-order approximation, the field strength near the air–glass interfaces at the core boundary scales with λ/a [54,121,161]. If for simplicity we approximate this core boundary with a circle of radius a and assume the mode field is constant on the core boundary, then, to first order, the integral in Eq. (26) is proportional to

$$\oint_{C_m} \vec{U}_k(s) \mathrm{e}^{jk(\rho' \sin\theta(\cos\phi-\phi'))}\, ds \propto \int_0^{2\pi} \frac{\lambda}{a} \mathrm{e}^{jka\sin\theta(\cos\phi-\phi')} a\, d\phi' \propto \lambda J_0(ka\sin\theta). \qquad \mathbf{(31)}$$

The power P_k carried by the mode is proportional to a^2 and it follows, therefore, that the surface scattering loss is therefore proportional to

$$\alpha_{ssc} \propto \frac{\lambda^{-4}}{a^2} \int_0^{\pi} \tilde{\psi}_{1D}\left(\beta - k\cos\theta\right) \lambda^2 J_0^2(ka\sin\theta)\sin\theta\, d\theta. \qquad \mathbf{(32)}$$

Of the terms in the integral, the PSD from surface capillary waves scales with λ (when no cutoff is imposed) and the remaining integral over θ scales approximately as $1/ka \propto \lambda/a$. Combining these together, we find that the surface scattering loss scales as

$$\alpha_{sc} \propto \frac{\lambda^{-4}}{a^2} \cdot \lambda^2 \cdot \lambda \cdot \frac{\lambda}{a} \propto \frac{1}{a^3}. \qquad \mathbf{(33)}$$

This is an important and somewhat surprising result which suggests that under the approximations made here, the core size is the only important parameter in determining the scattering loss. It is compatible with the well-established and experimentally validated observations with rigidly scaled PBGFs which showed the loss decreasing as λ^{-3} when both the core size and wavelength were scaled in proportion [49,196]. To further confirm this, we plot in Fig. 20 the scattering loss computed for the PBGF of Fig. 7 rigidly scaled to operate at wavelengths from 0.6 to 2.5 µm. We also show the minimum scattering loss in the first and second antiresonant window for the NANF as a function of the core radius a.

Equation (33) suggests that, in principle, the surface scattering contribution to loss in a fiber guiding across multiple spectral regions does not depend strongly on wavelength. In Fig. 19, we see that for the NANF under analysis, there is a weaker $\lambda^{-0.5}$

Figure 20

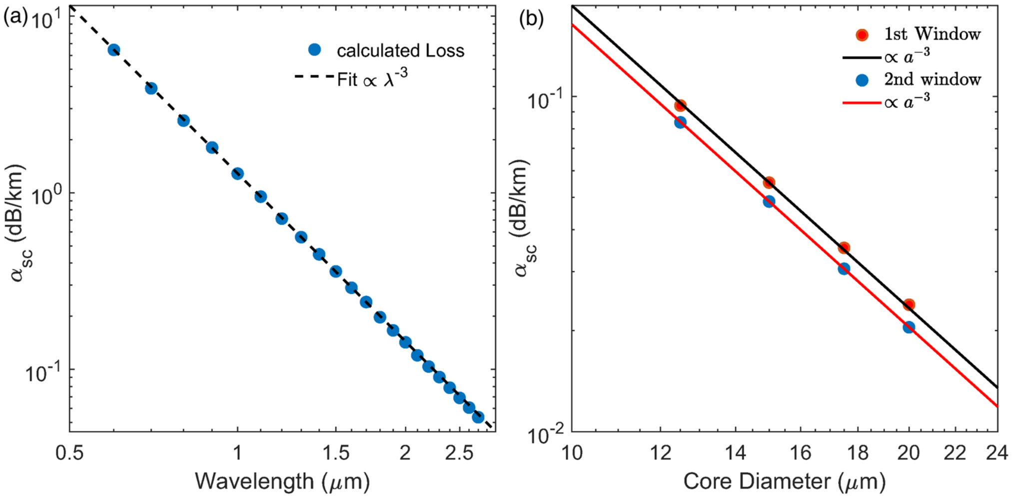

Scaling rules for the surface scattering loss in (a) PBGFs and (b) NANFs. The PBGF of Fig. 7 is rigidly scaled for operation at different wavelengths and as a result, our model predicts the well-known experimental results of a λ^{-3} scaling (or, more precisely, a^{-3} scaling; see the text). For the NANF, the loss minima within the antiresonance windows also scales as a^{-3}.

scaling with the wavelength, not too dissimilar to the one found by Roberts *et al.* for solid-core microstructured fibers [48]. This weak wavelength dependence reflects the approximations made in reaching Eq. (33).

2.4e. Simplified Heuristic Model for Surface Scattering Loss

In this section, we turn our attention to the question of whether the surface scattering loss computed rigorously in the previous sections can be approximated to facilitate less computationally intense estimates. To do so, we consider the simpler approximation of isolated and uncorrelated scatterers. Here, we assume that the rough interfaces can be thought of as a collection of independent scattering dipole elements radiating away part of the light incident upon them. Let us assume that the mode $|\psi_k\rangle$ is propagating in a section of length L of fiber which contains the rough air–glass interfaces. Following Refs. [54,197], we postulate that a typical scatterer on this surface has a volume ΔV_s. Its induced dipole moment may therefore be expressed as

$$\mathbf{p} = \varepsilon_0 \Delta\varepsilon \Delta V_s \cdot \mathbf{E}_k. \tag{34}$$

Here, $\Delta\varepsilon$ is the permittivity contrast between air and silica and $\mathbf{E}_k$ is the incident mode's electric field strength at the scatterer location. When the dipole is assumed to radiate in free space, the radiated power is approximated by

$$\begin{aligned} dP &= \frac{c^2}{12\pi}\left(\frac{\mu_0}{\varepsilon_0}\right)^{\frac{1}{2}}\left(\frac{\omega}{c}\right)^4 |\mathbf{p}|^2 \\ &= \frac{1}{12\pi}\left(\frac{\omega}{c}\right)^4 \Delta\varepsilon^2 \Delta V_s^2 \left(\frac{\varepsilon_0}{\mu_0}\right)^{\frac{1}{2}} |\mathbf{E}_k|^2 . \end{aligned} \tag{35}$$

The total radiated power from a section of length L of the fiber is therefore

$$P = \frac{1}{12\pi}\left(\frac{\omega}{c}\right)^4 \Delta\varepsilon^2 \Delta V_s^2 \left(\frac{\varepsilon_0}{\mu_0}\right)^{\frac{1}{2}} \frac{1}{\Delta\mathcal{A}} \int_L dz \oint_C |\mathbf{E}_k|^2 \, ds, \tag{36}$$

where $\Delta\mathcal{A}$ is the average area occupied by a dipole on the interface and C represents the perimeters of the air–glass interfaces in the cross section. In a further approximation, we assume that L is short enough that the field strength does not change appreciably over L. If we then express the total power P_k carried by the mode as a Poynting flux, we derive the surface scattering loss per unit length as

$$\alpha_{ssc} = \frac{P}{P_k L} \sim \frac{1}{6\pi}\left(\frac{\omega}{c}\right)^4 \Delta\varepsilon^2 \frac{\Delta V_s^2}{\Delta\mathcal{A}} \left(\frac{\varepsilon_0}{\mu_0}\right)^{\frac{1}{2}} \frac{\oint_C |\mathbf{E}_k|^2 \, dl}{\iint \mathbf{z}\cdot\mathbf{E}_k \times \mathbf{H}_k^* \, dS}. \quad \textbf{(37)}$$

The uncorrelated scatterers approximation therefore leads to the conclusion that the surface scattering loss is proportional to the geometry and mode field-dependent quantity:

$$F = \left(\frac{\varepsilon_0}{\mu_0}\right)^{\frac{1}{2}} \frac{\oint_C |\mathbf{E}_k|^2 \, dl}{\mathbf{z}\cdot\iint \mathbf{E}_k \times \mathbf{H}_k^* \, dS}, \quad \textbf{(38)}$$

known as the normalized interface field intensity [49,71,197]. This simple quantity has often been used in the literature, to compare the scattering loss performance of HCFs designs, the underlying assumption being that the lower the value of F, the lower the surface scattering loss will be. Despite the simplicity of the assumptions involved in deriving Eq. (37), it is conceivable that for fibers manufactured with the same process (thus assumed to have the same roughness statistics) and operating at the same wavelength, a simple calibration of the F parameter could be used to estimate loss. We found, for example, that for 1550 nm PBGFs fabricated in our lab, when assuming that all the loss was due to surface scattering alone, the simple scaling given by

$$\alpha_{sc}\ (\text{dB/km}) = \eta F(\mu m^{-1}) \quad \textbf{(39)}$$

often provided an adequate approximation for the fiber loss, with the proportionality coefficient taking the value $\eta = 300$ [135,198]. We plot in Fig. 21 the surface scattering loss as would be predicted from Eq. (39) for the optimized PBGF and NANF of Fig. 7 using a constant, wavelength-independent value $\eta = 300$. With this value, Eq. (39) predicts 1.2 and 0.2 dB/km at 1550 nm for the PBGF and NANF, respectively, a factor of 3 higher than obtained from Eq. (28).

As can be seen, using a constant value of η predicts for the NANF surface scattering loss minima that increase with wavelength, with the minimum loss in the first window higher than that in the second window. This is evidently incompatible with most scattering processes. Therefore, to capture the most general case, we assign a wavelength dependence to the proportionality coefficient η and write

$$\alpha_{sc}\ (\text{dB/km}) = \eta(\lambda)\cdot F \quad \textbf{(40)}$$

and use the rigorous model of the previous sections to inform the choice of such a dependence. Focusing on the NANF and by extension other ARFs, we first note that using the same reasoning as Section 2.4.4, the normalized interface field intensity F scales as λ^2/a^3. This is evidenced by the dashed orange curve in Fig. 21.

To match the weak wavelength dependence of approximately $\lambda^{-0.5}$ (see Fig. 19) resulting from the rigorous scattering model, we propose that an adequate estimate of the surface scattering loss can be obtained through

$$\alpha_{sc}\ (\text{dB/km}) = \eta_0 \cdot \left(\frac{\lambda_0}{\lambda}\right)^{2.5} \cdot F. \quad \textbf{(41)}$$

Exploiting the fact that $\eta_0 = 300$ resulted in losses 3x higher than the rigorous model at 1550 nm, we find that the lower value $\eta_0 = 100$ at a wavelength $\lambda_0 = 1550$ nm provides a reasonable agreement with the rigorous calculations of the previous sections.

Figure 21

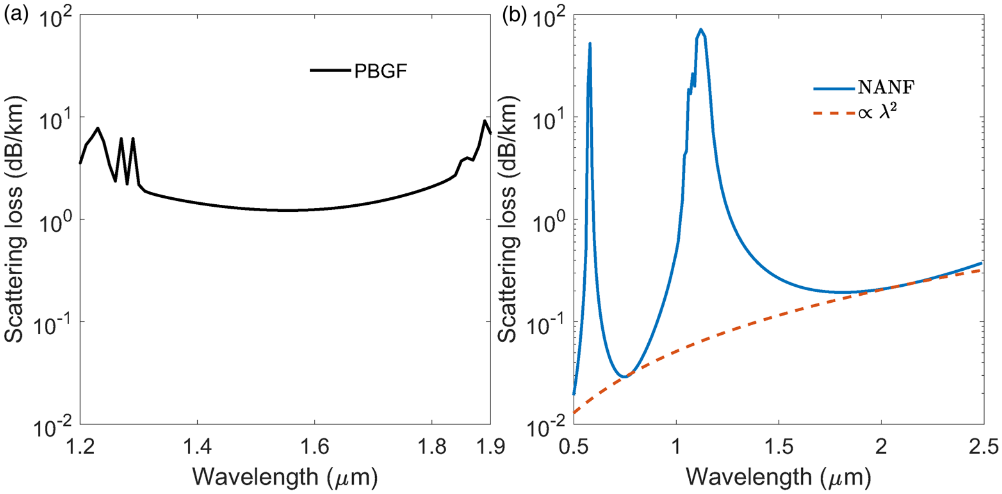

Scattering loss predicted from the normalized interface field intensity F in the (a) PBGF and (b) NANF of Fig. 7. Here, we have taken $\alpha_{sc} = \eta F$ with a constant $\eta = 300$. The estimated scattering loss reaches a minimum of 1.2 dB/km in the PBGF at 1.55 μm (three times higher than with the rigorous scattering model), whereas in the NANF, the minima in the first and second windows are ~0.18 dB/km and ~0.03 dB/km, respectively. The minima across antiresonant windows follow the λ^2 scaling approximately.

Figure 22

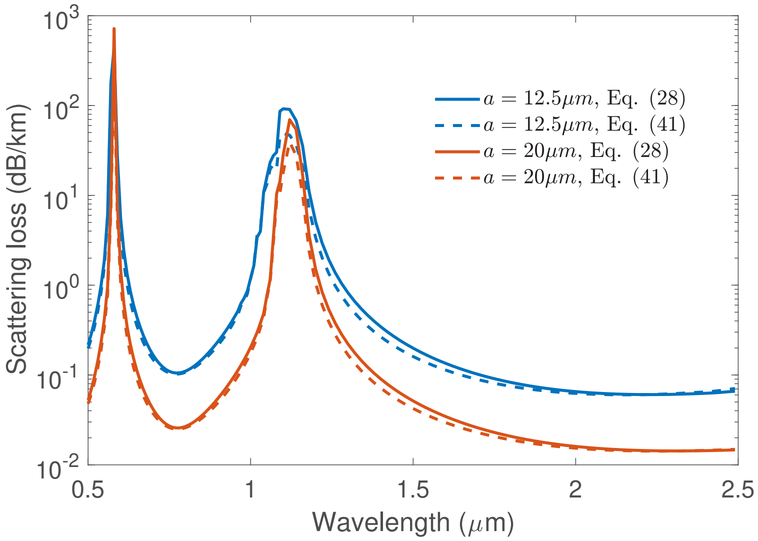

Comparison between rigorous scattering loss model (solid lines) and the heuristic approximation of Eq. (41) for two NANFs with core diameters 25 μm (blue) and 40 μm (orange).

Figure 22 shows the approximation of Eq. (41) and the surface scattering loss from Eq. (28) for two NANFs with core diameters of 25 and 40 μm. Although it is slightly less accurate and underestimates the scattering loss near the resonant wavelengths, the approximation of Eq. (41) appears adequate for rapid surface scattering loss estimates. We emphasize once again that in agreeing with the rigorous scattering model, the revised expression of Eq. (41) predicts lower scattering loss for the PBGFs than previously thought. We believe this is in line with the new understanding of other loss contributions previously unaccounted for but which we explore in the remainder of this paper.

Although not too dissimilar to the often used formula $\eta \cdot F \cdot (\lambda_0/\lambda)^3$, the revised formula Eq. (41) provides a more accurate approximation to the surface scattering loss. We emphasize that ultimately, calculating surface scattering loss from the normalized interface field intensity F is at best heuristic, but can be helpful to compare contributions from scattering in different fibers and to perform rapid loss estimates where needed.

2.4f. Surface Scattering as a Source of Intermodal Coupling

In addition to causing loss via coupling to radiation, the surface roughness scatters optical power from one guided mode of the fiber to another, resulting in intermodal interference (IMI). This can adversely affect the performance of telecoms links [199–202]. The rate of intermodal power exchange can be calculated from our treatment of scattering loss in Section 2.4.1. It is known from classical theory that the induced current density $\mathbf{J}_k(s, z)$ resulting from the propagation of mode $|\psi_k\rangle$ will excite another discrete mode $|\psi_l\rangle$ with unitless amplitude given by [203]

$$a_{kl} = \int_V \mathbf{E}_l^* \cdot \mathbf{J}_k(s, z)\, dV. \tag{42}$$

It follows from here that the power coupling coefficient per unit length to mode $|\psi_l\rangle$ is [161,204,205]

$$\begin{aligned} h_{kl} = & \frac{1}{L}\langle a_{kl} a_{kl}^* \rangle = \omega^2 \varepsilon_0^2 \tilde{\Psi}_{1D}\,(\beta_k - \beta_l) \\ & \times \sum_m \left| \oint_{C_m} \left(\Delta\varepsilon_r \mathbf{E}_{\parallel l}^*(s) \cdot \mathbf{E}_{\parallel k}(s) - \Delta\frac{1}{\varepsilon_r} \mathbf{D}_{\perp l}^*(s) \mathbf{D}_{\perp k}(s) \right) ds \right|^2 . \end{aligned} \tag{43}$$

As modes $|\psi_k\rangle$ and $|\psi_l\rangle$ propagate in the fiber exchanging power at a rate h_{kl}, it results in added noise in the form of IMI, but also additional loss when one of the modes has higher attenuation. We examine propagation in the presence of intermodal coupling by means of coupled power theory in Section 3.1 (see also Ref. [194]), but we show in Fig. 23 the calculated h_{kl} matrix from roughness scattering for the first four mode groups (LP_{01}, LP_{11}, LP_{21}, and LP_{02}, 12 guided modes in total) of the PBGF and NANF of Fig. 7 at 1550 nm.

As can be seen, roughness-induced mode coupling is significantly stronger in the PBGF than in the NANF. This originates, as before, from the lower field at the air–glass interfaces. The highest coupling rate from the fundamental mode is to the LP_{02} mode of the same polarization, amounting to 9×10^{-7} m^{-1} in the PBGF but only 1.6×10^{-8} m^{-1} in the NANF of similar core sizes. This mode, however, often suffers from high differential loss (see the following section). The lowest loss higher-order mode group is the LP_{11} mode for which we calculate a total coupling coefficient of $3 \times 10^{-7} m^{-1}$ for the PBGF and $2 \times 10^{-8} m^{-1}$ for the NANF. Finally, we note that roughness-induced coupling of one polarization of the fundamental mode to the other is significantly lower in both fibers, amounting to 1.5×10^{-9} m^{-1} in the PBGF and 10^{-10} m^{-1} in the NANF, respectively. Such low levels represent a fundamental limit to the polarizaton mode coupling in HCFs, though other perturbations may exacerbate this [206].

2.5. Loss in Higher-Order Modes

The foregoing analysis has so far pertained to the pair of degenerate fundamental HE_{11} modes in HCFs because they typically offer the lowest loss. All of the intrinsic

Figure 23

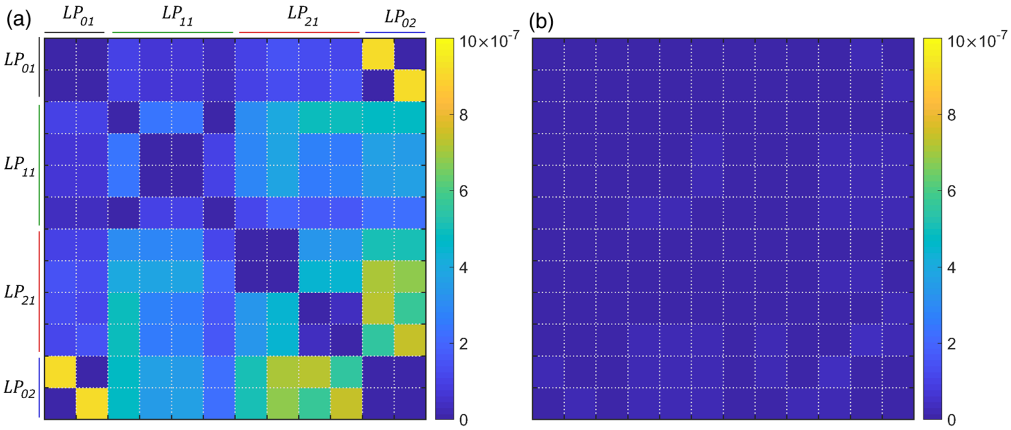

Roughness scattering-induced intermodal coupling in the (a) PBGF and (b) NANF of Fig. 7. The power transfer between the modes occurs predominantly between modes of the same azimuthal symmetry. Like loss, it is higher in PBGFs than in NANFs.

loss mechanisms we have discussed scale favorably with larger core sizes, i.e., these loss contributions decrease when the core is enlarged. However, fibers with larger core size support an increasingly high number of transverse modes of propagation [10,58,207,208]. Unlike in solid-core multimode fibers where the attenuation is virtually independent of mode order when they are far from cutoff, in HCFs, there exists an intrinsic differential attenuation between the fundamental and higher-order modes [61,208]. However, the level of differential loss can be enhanced through engineering the structure of the cladding to achieve effective single-mode operation even in large core fibers [91,128,130]. The reverse is also possible and, in principle, the cladding region can be designed in such a way that the differential loss between the fundamental and higher-order modes is minimized, thereby achieving few-mode/multi-mode operation [209,210].

In Section 2.1, we briefly discussed why higher-order modes in HCFs must inevitably suffer from higher leakage loss (see Section 2.1). From the partial reflection picture, higher-order modes correspond to rays that impinge on the core cladding interface at a steeper angle and are thus reflected less efficiently, leading to higher leakage loss. A qualitative analysis from the inhibited-coupling perspective yields the same conclusion. Higher-order modes have a stronger overlap with cladding modes and simultaneously have propagation constants closer to those of the cladding modes, thus leading to higher leakage loss (see Eq. (13)). In the simplest of HCFs analyzed by Marcatili and Schmeltzer [121], the differential leakage loss increases with the mode order, scaling as u_{nm}^2 (recall that u_{nm} is the mth zero of the Bessel function $J_{n-1}(x)$, $u_{01} \approx 2.4048$, $u_{11} \approx 3.8317$, $u_{21} \approx 5.1356$, $u_{02} \approx 5.5201$, etc.). For the model ARFs studied by Bird, Eqs. (10) and (11), show that for a structure with l antiresonant layers, the leakage loss scales with the more order as u_{nm}^{l+2}. In practical fiber designs such as photonic bandgap or ARFs, quantifying the loss of the higher-order modes is not as straightforward. Depending on its complexity and the guidance mechanism, the cladding structure supports modes whose interaction with the core-guided modes is not easily predicted.

To illustrate the differential leakage loss in HCFs, we plot in Fig. 24 the calculated leakage loss for the first four mode groups of the PBGF and NANF shown in Fig. 7. For simplicity, we adopt the LP terminology, but it should be understood the modes are not linearly polarized in practice.

Figure 24

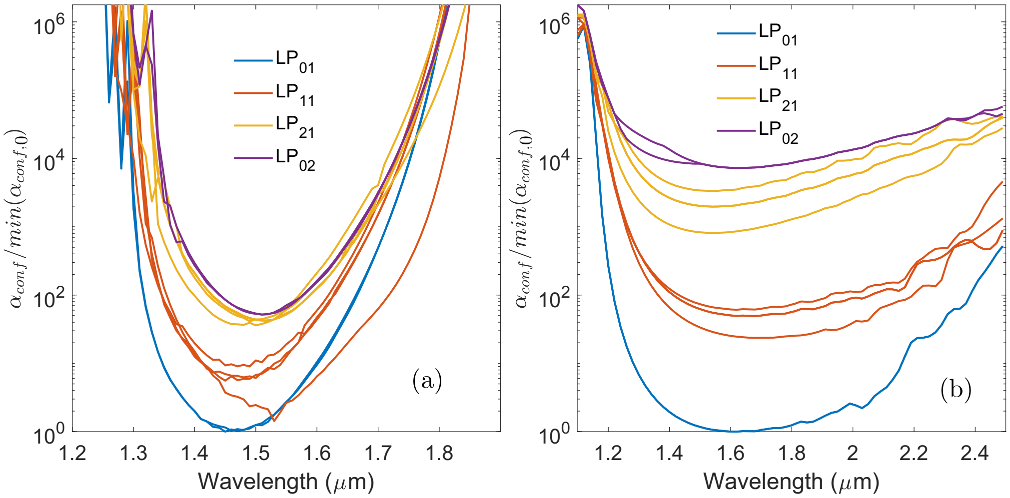

Leakage loss in higher-order modes in hollow-core optical fibers. The leakage loss calculated for the first four mode groups is normalized to the minimum leakage loss of the fundamental mode. (a) Mode-dependent leakage loss in the PBGF of Fig. 7 and (b) mode-dependent leakage loss for the NANF of Fig. 7. The leakage loss increases more slowly with mode order in the PBGF than in the NANF due to the absence of phase-matched lossy cladding modes.

In the PBGF, as the order of the mode increases, its propagation constant decreases and becomes closer to that of cladding modes at the bottom of the photonic bandgap (see Fig. 2), leading to higher leakage. However, for the first 12 modes of the 19c fiber examined here, leakage loss remains below 100 times the leakage loss of the fundamental mode, which translates to less than 10^{-3} dB/km near the center of the photonic bandgap. Interestingly, in the particular structure examined here (Fig. 7), one of the LP_{11} modes, the TE_{01} mode, has lower leakage loss than the fundamental modes at longer wavelengths beyond about 1.55 μm, a behavior similar to what is observed in hollow metallic waveguides [121].

In contrast, in the NANF, the leakage loss grows rapidly with mode order. For the selected structural parameters (see Fig. 7), we find that the lowest loss LP_{11} mode, the TE_{01} mode has a minimum leakage loss 23 times higher than that of the fundamental mode near the center of the transmission window. In this low-loss spectral region. the LP_{11} mode group averages a leakage loss of approximately 30 dB/km, 46 times higher than that of the fundamental mode. All other high-order modes (HOMs) beyond LP_{11} have higher leakage loss than approximately 1 dB/m. It appears therefore that this six-tube NANF may effectively be regarded as a two-mode fiber [115]. It is worth mentioning that the cladding can be further optimized to increase the leakage of the LP_{11} mode too, for example by changing the ratio z/a (see Fig. 7 here and Fig. 11 of Ref. [52], or adopting a geometry with five sets of tubes [52,98,211].

Next we look at potential contributions from absorption and bulk scattering in the glass to the loss of higher-order modes. We plot in Fig. 25 the material loss suppression factor ζ for higher-order modes in the PBGF and NANF of Fig. 7. In both fiber types, at wavelengths away from the edges of the transmission windows, we see that ζ is roughly proportional to u_{nm}^2. A first-order perturbation analysis reveals that because normalized field strength near the core boundary is a zero of the order of $u_{nm}\lambda/a$, the integral of Eq. (18) scales as $u_{nm}^2\lambda^2 t/a^3$ (see Section 2.2). As absorption and glass

Figure 25

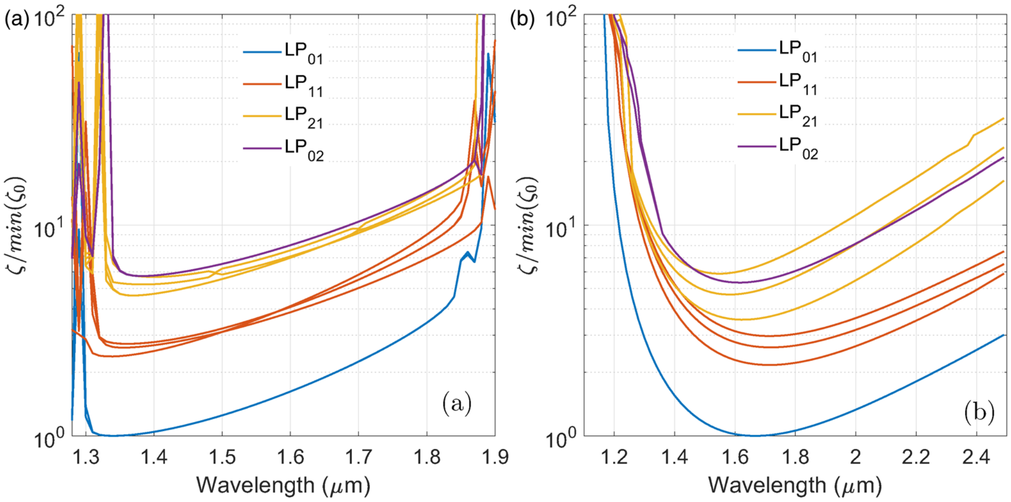

Glass absorption/bulk scattering suppression factor for higher-order modes in the (a) PBGF and (b) NANF of Fig. 7. In both fiber types, contribution from scattering and absorption within the glass scale approximately with the mode order as u_{nm}^2.

material loss only scale as u_{nm}^2, we conclude that relying on these loss mechanisms will be ineffective at rapidly stripping undesired higher-order modes.

Finally, we consider the contribution from surface roughness scattering. Using Eqs. (26) and (28), we compute the surface roughness scattering loss for the first four mode groups of the PBGF and NANF we have considered so far. The results we obtain are shown in Fig. 26. Just like with absorption, we see that in both fibers, the loss from surface scattering scales approximately as u_{nm}^2. We also observe, in the case of PBGF in particular, the degenerate modes making the LP-like HOM groups have different scattering loss contributions. In the LP$_{11}$-like mode group for example, the TE mode offers the lowest loss near the middle of the bandgap and the TM mode the highest due to the large discontinuity of its electric field near the core boundary.

We conclude from the preceding analysis that of the intrinsic loss mechanisms in HCFs, material loss and surface roughness scattering are fundamentally limited to scaling with the transverse mode order as u_{nm}^2. However, the cladding can be engineered to control the differential leakage loss between the transverse modes, e.g., through phase matching undesired core modes with lossy cladding modes. This understanding has been exploited to achieve effective single-mode fibers, whether in PBGFs via the introduction of shunt cores [130] or in ARFs through the control of the size of the cladding tube [52,91].

In PBGFs without these higher-order mode stripping shunt cores (such as in Refs. [19,130]), at wavelengths away from the edges of the bandgap or surface modes, leakage is low for all modes (below 10^{-3} dB/km for the example we considered). The total loss is essentially dominated by surface scattering (unless operating where the glass is highly absorptive). When this is the case, the total loss scales approximately with mode order as u_{nm}^2. This is supported by experimental loss measurements in 37c PBGFs used for mode-division multiplexed data transmission for example [62].

In ARFs, in spectral regions where there is no absorption, the contribution from leakage tends to be higher than scattering. As the structure can be readily engineered to achieve phase matching between lossy tube modes and core modes (e.g., through

Figure 26

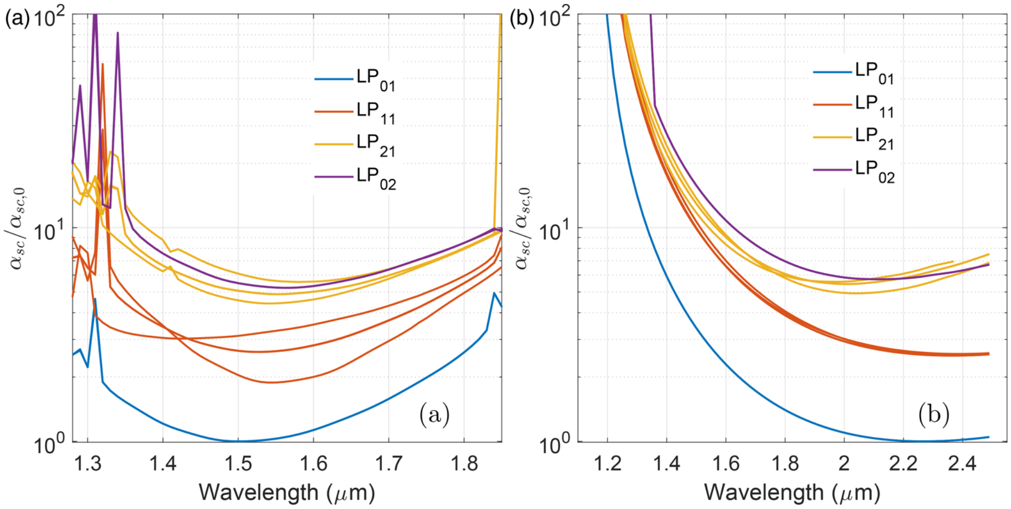

Surface scattering loss for the higher-order modes in the (a) PBGF and (b) NANF of Fig. 7. Here too, the loss scales approximately with the mode order as u_{nm}^2, i.e., is roughly 2.5 times higher for the LP_{11} mode and 4.6 times higher for the LP_{02}, etc.

the choice of the size of the hollow regions in the cladding), the total loss of all HOMs can be made orders of magnitude higher than that of the fundamental mode, resulting in effective single mode operation after an appropriate propagation distance. On the other hand, by using smaller cladding tubes or subdividing the tubes into smaller hollow regions, one can reduce the loss of higher-order modes [209,210]. In NANFs, for example, the choice of the size of the nested tubes plays an important role in determining the loss of higher-order modes [52]. The underlying principle is that of controlling the propagation constant difference between core and cladding modes as well as their spatial overlap.

3. EXTRINSIC LOSS MECHANISMS

Having analyzed the key intrinsic loss mechanisms in HCFs, we now turn our attention to those contributions to loss that result from imperfections in fabrication such as longitudinal non-uniformities, or from the macroscopic deployment conditions of the fiber such as bends. Although these can, in principle, be reduced by improvements in fiber fabrication processes, improved packaging strategies (e.g., UV curable coatings) or the relaxation of deployment criteria and conditions, their contribution to loss remains significant in most practical scenarios. Understanding them, particularly how they scale with key fiber parameters, is therefore of paramount importance in informing the fiber design and manufacturing processes. In this part of the paper, we first focus on random microbends which appear to be the most important extrinsic contributor to loss and can be addressed through adequate fiber packaging. We then briefly survey other perturbations which may be present in the fiber but which perhaps can be addressed through finer control of the drawing process. Finally, we describe the macrobend loss that the fiber incurs when it is coiled at a constant diameter for distances greater than many hundreds of wavelengths. Such bend loss is extremely important in a range of applications where the fiber must be in a compact form, see, for example, Ref. [33].

3.1. Microbend Loss

Microbending refers to microscopic displacements of the fiber axis that cause it to depart from an ideal straight trajectory. They often result from random lateral loads on the fiber, for example, when it is wound under tension on a drum with a rough surface under tension or when pressing against a strength member within a cable [212]. In the early days of research into conventional single mode fibers, it was recognized that if unaddressed, microbending would cause severe additional loss to (~100 dB/km) and exacerbate polarization mode dispersion [212–214]. In solid-core multimode fibers or even multicore fibers, microbending induces strong intermodal power transfer, thereby degrading the fiber's performance in data transmission systems. Essentially, microbends cause scattering from a mode of interest to other guided modes and to radiation, thus resulting in intermodal coupling and excess loss [215–217]. Through decades of research, it is now well established that there are three main routes to address microbending in standard solid-core optical fibers. The first is to increase the diameter of the fiber and its polymer coatings to give the fiber stiffness and thus increase its ability to resist bends. The second is to use softer primary coatings which effectively act as a shock absorber preventing external mechanical loads from displacing the fiber axis. The third route consists of engineering the refractive index profile of the fibers in such a way that it results in a large separation between the propagation constant of the guided mode of interest and that of the radiation modes to which the microbending-induced coupling is the strongest [213,218,219]. *A priori*, these solutions ought to work also for HCFs [195]. However, the extent to which this might be the case is not yet well known because a comprehensive analysis of microbending in HCFs has not hitherto been performed. This section presents such an analysis.

We start by examining a single microbend perturbation also studied in detail in Refs. [220,221]. Effectively, this consists of a short fiber section of length dz being bent with radius of curvature R_b, thus equivalent to a directional change $\phi = \dfrac{dz}{R_b}$ for the fiber axis (see Fig. 27). When the fiber mode $|\psi_k\rangle$ carrying unit power (i.e., normalized according to Eq. (16)) is incident on the bend, provided that ϕ is small, a perturbative analysis tells us that at the end of the bent section, the mode $|\psi_l\rangle$ will be excited with amplitude

$$a_{kl} = \left\langle \psi_l | \Delta\hat{A} | \psi_k \right\rangle dz, \tag{44}$$

where $\Delta\hat{A}$ is a bend perturbation operator which has been derived using a coupled-mode analysis in Refs. [54,159,174,220,221]. Assuming the bend is along the x-axis, the amplitude coupling coefficient above can be written explicitly as the integral [54]

$$a_{kl} = \left\langle \psi_l | \Delta\hat{A} | \psi_k \right\rangle dz = dz \iint \begin{bmatrix} E_x \\ E_y \\ E_z \\ H_x \\ H_y \\ H_z \end{bmatrix}_l^{\dagger} \frac{\omega x}{c R_b} \begin{pmatrix} \varepsilon & & & & & \\ & \varepsilon & & & & \\ & & -\varepsilon & & & \\ & & & \mu & & \\ & & & & \mu & \\ & & & & & -\mu \end{pmatrix} \begin{bmatrix} E_x \\ E_y \\ E_z \\ H_x \\ H_y \\ H_z \end{bmatrix}_k dx\, dy. \tag{45}$$

In waveguides with circular symmetry in the cross section, x can be written in a cylindrical coordinate system (ρ, θ, z) as $x = \rho\cos(\theta)$ and it follows that because all the modes have a dependence $e^{jm\theta}$ (m is the azimuthal mode number), only modes satisfying the selection rule $\Delta m = \pm 1$ will be coupled as a result of the bend [171]. Although the geometries of HCFs generally do not have circular symmetry (typically sixfold for the PBGF, N-fold for ARFs with N being the number of sets of cladding tubes), this selection rule also holds approximately (as shown, for example, in the coupling matrix of Fig. 28 discussed in the following).

For such a single bend, it is of interest to estimate the total power coupled out of the incident mode as a result of the perturbation. First, from the excited amplitude of

Figure 27

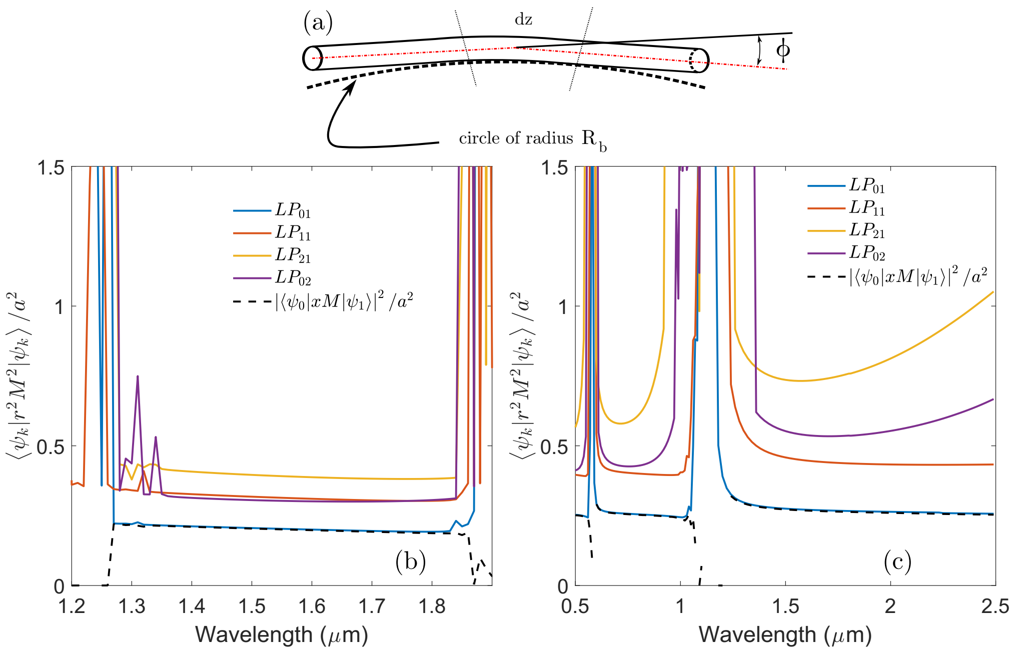

Normalized mode spot areas or normalized total power loss at a directional change in hollow-core optical fibers. (a) Illustration of a directional change ϕ around a bend of radius R_b. (b) Mode spot areas for the first four mode groups of the PBGF and (c) for the NANF. The mode spot area, and thus microbend sensitivity, increases rapidly with mode order. The dashed black lines show the normalized power coupled from the fundamental mode to the LP$_{11}$ mode group.

Figure 28

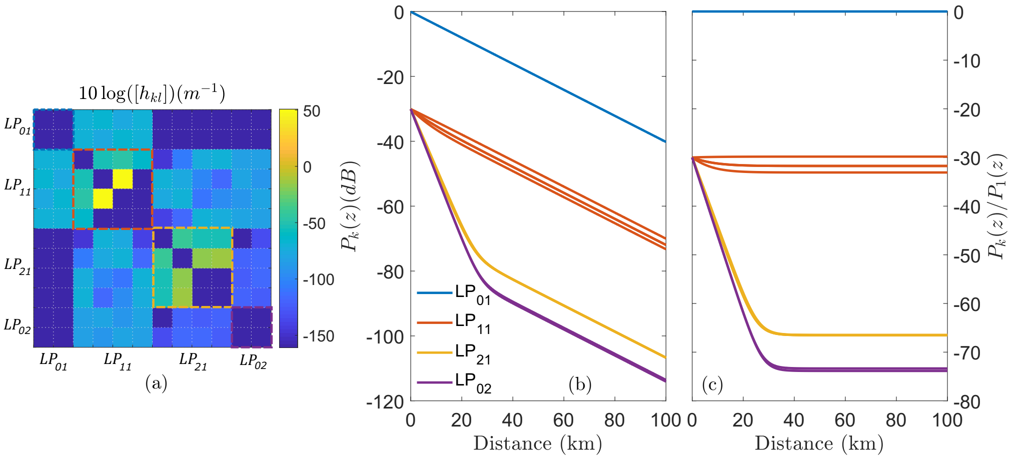

Example of a microbending-induced mode coupling matrix and modal power evolution with distance in the example PBGF. (a) Microbending coupling matrix showing the ±1 selection rule for bend-induced coupling between mode groups. (b) Solution to the coupled power equation and (c) modal power normalized to fundamental mode power. The assumed PSD for the microbend perturbations is $\Xi(\kappa) = A/\kappa^{2p}$ with $A = 10^6$ and $p = 2$. With this perturbation, it follows that microbending induces about −30 dB power in the LP$_{11}$ modes, showing that microbending can lead to considerable IMI in PBGFs because of the low differential loss.

Eq. (45), we calculate the power coupled from mode $|\psi_k\rangle$ to mode $|\psi_l\rangle$ as

$$\Delta P_{k\to l} = a_{kl}^* a_{kl} = \left\langle \psi_k|\Delta\hat{A}^*|\psi_l\right\rangle \left\langle \psi_l|\Delta\hat{A}|\psi_k\right\rangle . \tag{46}$$

The total power coupled out of the mode $|\psi_k\rangle$ is therefore a summation over all the destination modes and is obtained as (see Refs. [220–222])

$$\Delta P_k = \sum_{l\neq k} \Delta P_{k\to l} = \sum_{l\neq k} \left\langle \psi_k|\Delta\hat{A}^*|\psi_l\right\rangle \left\langle \psi_l|\Delta\hat{A}|\psi_k\right\rangle = \phi^2 \left(\frac{\omega}{c}\right)^2 \left\langle \psi_k|x^2M^2|\psi_k\right\rangle , \tag{47}$$

where we have exploited the completeness rule, i.e., $\sum |\psi_l\rangle\langle\psi_l\rangle = 1$, and where M is the diagonal matrix in Eq. (45). This interesting result shows that the total power coupled out of the mode $|\psi_k\rangle$ depends only on the quantity $\left\langle \psi_k|x^2M^2|\psi_k\right\rangle$. This quantity is effectively a mode-field weighted average of x^2 and, thus, has the meaning of an area. For standard single-mode fibers, Petermann refers to this as the mode spot area [223–225]. The total power coupled out of the incident mode is thus proportional to its mode spot area. To account for the fact that HCFs typically do not have a circular symmetry, we assume microbends may occur along any azimuthal direction in the fiber cross section and thus write

$$\Delta P_k = \frac{1}{2}\phi^2 \left(\frac{\omega}{c}\right)^2 \left\langle \psi_k|r^2M^2|\psi_k\right\rangle . \tag{48}$$

Figure 27 shows the normalized mode spot area $\left\langle \psi_k|r^2M^2|\psi_k\right\rangle /a^2$, or mode spot area, for the first 12 modes of the PBGF and NANF of Fig. 7. The spot areas are calculated from the mode-field data obtained from the finite-element solver. Unsurprisingly, we see the mode spot area increase with mode order, indicating that higher-order modes will incur greater bend-induced penalties. We also plot for both fibers (dashed black lines) the normalized power transferred from the fundamental mode $|\psi_0\rangle$ to the LP_{11} modes denoted $|\psi_1\rangle$ for simplicity (we have summed over the TE_{01}, TM_{01}, and the degenerate HE_{21} modes). Note how this quantity, $|\langle\psi_1|xM|\psi_0\rangle|^2/a^2$ is virtually identical to the spot area of the fundamental mode, showing that nearly all of the power coupled out of the fundamental mode at a directional bend is transferred to the LP_{11} modes [222]. This is important for some useful approximations which we make next.

For the fundamental mode in both fibers, the mode spot area $\left\langle \psi_k|r^2M^2|\psi_k\right\rangle$ does not change appreciably with the wavelength within the transmission window. This is in contrast to single-mode weakly guiding fibers where the mode spot area grows rapidly with wavelength due to the mode field expanding further into the cladding [225,226]. As the unnormalized ΔP_k has an additional factor $k^2 = 1/\lambda^2$, it follows that unlike in SMFs, the total power lost from a mode at a directional change in HCFs is higher at shorter wavelengths. As shown in the following discussion, microbending loss in HCFs is more prominent at shorter wavelengths as a result. Interestingly, despite their similar core sizes, the nature of the guidance mechanism results in the PBGF having a 20% smaller spot area $\left\langle \psi_k|r^2M^2|\psi_k\right\rangle$ than the corresponding NANF, giving it a small advantage in lower microbending loss and microbending-induced mode coupling (see also Fig. 30).

We now consider a section of fiber of length L is subject to random microbends with local random curvature radius $R_b(z)$. The foregoing analysis says that when L is short enough that the amplitude of incident mode $|\psi_k\rangle$ is considered constant, then at the end of this section of fiber, the mode $|\psi_l\rangle$ is excited with an amplitude given by

$$a_{kl} = \int_0^L \left\langle \psi_l|\Delta\hat{A}|\psi_k\right\rangle dz = \int_0^L \left\langle \psi_l\left|\frac{1}{R_b(z)}\frac{\omega}{c}xM\right|\psi_k\right\rangle dz. \tag{49}$$

The rate of power coupling between the two modes per unit length is therefore

$$h_{kl} = \frac{1}{L}\left\langle a_{kl}^{*} a_{kl}\right\rangle, \tag{50}$$

where $\langle\cdots\rangle$ is an ensemble average. As before (see Section 2.4), this simplifies to

$$h_{kl} = \left(\frac{\omega}{c}\right)^2 \left|\left\langle \psi_l \middle| \frac{\omega}{c} x M \middle| \psi_k \right\rangle\right|^2 \Xi(\beta_k - \beta_l), \tag{51}$$

where $\Xi(\kappa)$ is the PSD of the curvature function $1/R_b(z)$ [225]. Such a curvature spectrum is not easily determined in practice. However, in conventional solid-core fibers for which microbending effects have been studied more extensively, researchers have commonly assumed a power spectrum of the form

$$\Xi(\kappa) = \frac{A}{\kappa^{2p}}, \tag{52}$$

where A is a constant characterizing, for example, the magnitude of the lateral loads causing the microbends, the ability of the fiber's packaging to dampen such loads, the number of such local point loads per unit fiber length and p is an exponent describing how rapidly the PSD decreases with increasing spatial frequency [213,218,227–231]. Considering, for example, uncorrelated point loads on the fiber within a cable, Olshansky finds that $p = 2$ [227]. However, fitting of experimentally measured microbending loss data for single-mode fibers has suggested higher values for p between 2 and 5 [231–233]. For simplicity, we assume a value $p = 2$ in the following discussion.

In the most general case, the effect of random microbends on the evolution of the optical power carried by each mode is described by coupled power theory which states that [171,234]

$$\frac{dP_k(z)}{dz} = -\alpha_k P_k(z) + \sum_{l=1}^{N} h_{kl}\left(P_l(z) - P_k(z)\right), \tag{53}$$

where α_k is the loss of the mode $|\psi_k\rangle$, $P_k(z)$ its power as a function of z, and h_{kl} are the power coupling coefficients of Eq. (51). When solving this system of coupled equations, it has been found that after a certain distance, a *steady state* is reached and the relative distribution of power among the modes regardless of initial conditions remains unchanged [234]. In the steady state, all the modes evolve with the same loss rate, which is higher than the loss of the fundamental mode alone and is called the *steady-state loss*.

An example of a numerical solution of Eq. (53) is shown in Fig. 28. We have considered the PBGF of Fig. 7 at 1550 nm for which we first calculated the microbending induced coupling matrix $[h_{kl}]$ for the first four mode groups. For our illustration here, we chose a microbending perturbation power spectrum obeying Eq. (52) with $A = 10^6$, $p = 2$. As can be seen from the coupling matrix, microbends couple power from one core mode group to a neighboring core mode group which satisfies the condition $\Delta m = \pm 1$ as expected from symmetry considerations. The fundamental modes thus couple predominantly to the LP_{11} modes, whereas the latter couples to LP_{01}, LP_{21}, and LP_{02} modes and so on. However, we note for this fiber that microbending appears to induce a strong coupling between modes within the same mode group, particularly within the LP_{11} and LP_{21} mode groups as can be seen. Using this coupling matrix, we solved Eq. (53) numerically for propagation over 100 km. We assumed initial conditions whereby the fundamental mode is launched into the fiber with every other mode excited at the −30 dB level below it. In the first 20 km or so, the slightly higher loss HOMs (LP_{21} and LP_{02}, both only ~2 dB/km on average) decay at a rate given by

Figure 29

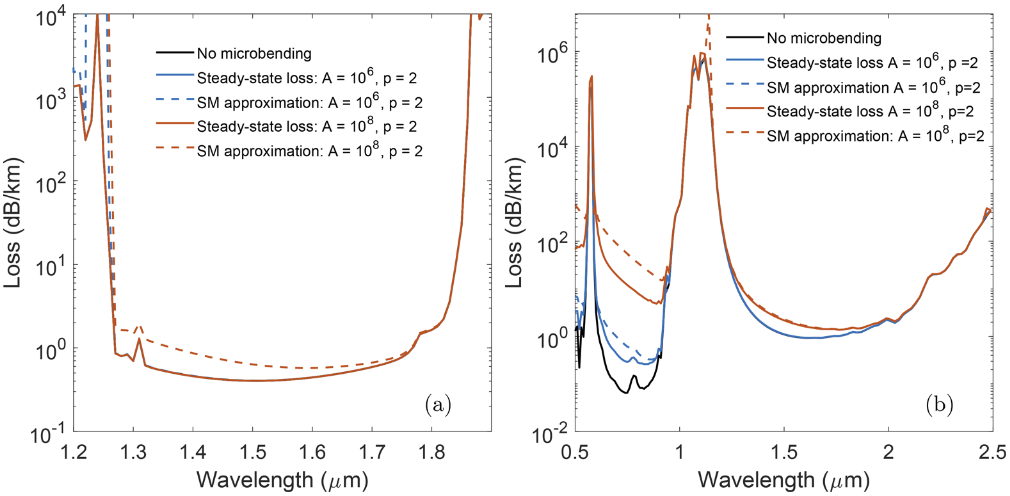

Microbending-induced loss penalty in the (a) PBGF and (b) NANF from solving the coupled power equations (53) for the first 12 guided modes. (a) PBGF: with its low differential loss, the assumed perturbation spectra do not induce appreciable added loss for the fundamental mode (all the curves overlap exactly, except for the inadequate single mode approximation discussed in the following). The biggest penalty is instead intermodal coupling. (b) NANF: in the first window, the single-mode approximation agrees well with the steady-state loss (the dashed curves overlap with the solid curves) but is less reliable in the second window at shorter wavelengths.

their respective loss coefficients (see Section 2.5). This decay is followed by power transfer to these modes from those with lower loss due to microbending. After about 30 km of propagation, a steady state is reached and, thereafter, all the modes decay at the same rate and their relative powers compared to that of the fundamental mode is constant. This decay rate is the steady-state loss.

Figure 29 shows the steady-state loss, that is, the total loss (leakage + scattering included) after the steady state is reached, calculated for the PBGF and NANF of Fig. 7 as a function of wavelength under two scenarios. First we consider the same perturbation with $A = 10^6$, $p = 2$ and a perturbation that is 100 times stronger, i.e., $A = 10^8$, $p = 2$. In the PBGF, the loss penalty from microbending is negligible as the steady-state loss value is nearly identical to the intrinsic loss of the fiber (all the curves overlap). This remains true even for the stronger perturbation with $A = 10^8$. The result is not surprising given the low differential loss between the modes of the PBGF and indicates therefore that the most important effect of microbending in this fiber type is intermodal power coupling, which would be a source of noise when the fiber is used in long-distance telecoms. For the NANF, We see that in the first antiresonant window, the weaker perturbation does not induce a noticeable loss penalty whereas such added loss is already present in the second antiresonant window. The stronger perturbation leads to loss penalties across both antiresonant windows, with higher loss at shorter wavelengths as discussed previously. The dashed lines in the plot are single-mode approximations which we discuss next.

3.1a. Single-Mode Approximation

In a host of applications using HCFs, it is often required that the fiber is effectively single-mode. In practice, this means imposing high loss on all higher-order transverse modes in the core. When light coupled from the fundamental to any other higher-order core mode or cladding mode is effectively lost, the additional loss incurred by the

Figure 30

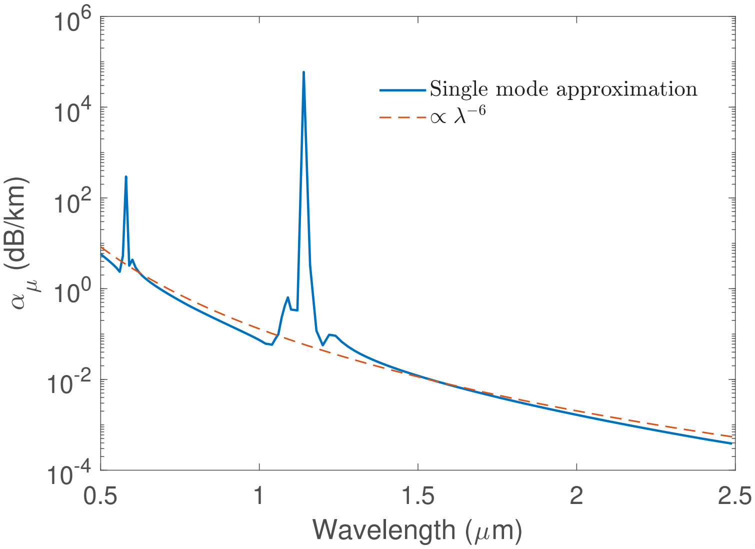

Single-mode approximation to microbend loss in the NANF of Fig. 7. It is assumed here that all the modes supported by the fiber other than the fundamental mode can be regarded as radiation modes, giving effectively an upper limit for the microbend loss. With the assumed PSD, the loss in the NANF scales approximately as λ^{-6}.

fundamental mode due to microbends can be obtained by summing up the power coupling coefficients as

$$\alpha_\mu = \sum_l \left(\frac{\omega}{c}\right)^2 \left|\left\langle \psi_l \left| \frac{\omega}{c} x M \right| \psi_0 \right\rangle\right|^2 \Xi(\beta_0 - \beta_l). \tag{54}$$

The summation extends over all the lossy HOMs and takes the meaning of an integration over the continuum of radiation modes. A further simplification can be made to this expression when this effectively single-mode condition holds and the power spectrum $\Xi(\kappa)$ decreases with spatial frequency, i.e., $d\Xi(\kappa)/d\kappa < 0$, as is the case for example from Eq. (52). We have established most of the power lost at a single bend from the fundamental mode is coupled to LP_{11} modes. As these modes also happens to have the smallest $\Delta\beta$ with the fundamental mode, so that $\Xi(\beta_0 - \beta_1)$ is the highest. It follows therefore that an upper bound to the loss can be obtained as

$$\alpha_\mu = \frac{1}{2}\left(\frac{\omega}{c}\right)^2 \left\langle \psi_0 | r^2 M^2 | \psi_0 \right\rangle \Xi(\beta_0 - \beta_1). \tag{55}$$

This expression is similar to Petermann's formula [223,224,226] for standard single-mode fibers which has been used as a first-order approximation to the microbending loss. The dashed lines in Fig. 29 are the sum of the intrinsic loss contributions and the microbending loss computed from the single-mode approximation of Eq. (55). The microbending loss contribution alone predicted by this expression is plotted in Fig. 30 for clarity for the NANF with a curvature power spectrum given by Eq. (52) with $A = 10^6$ and $p = 2$.

When the fiber is effectively single mode, Eq. (55) allows for a powerful insight into how the microbending loss scales with core size and wavelength. First, we note that the fundamental mode-field distribution in HCFs results in $\left\langle \psi_0 | r^2 M^2 | \psi_0 \right\rangle / a^2$ being constant with wavelength (see Fig. 27). From simple analytical expressions giving the propagation constant of the guided modes derived by Marcatili and Schmeltzer

[121], it follows that to the first order, $\beta_0 - \beta_1 \approx \frac{u_{11}^2 - u_{01}^2}{2}\frac{1}{ka^2}$. Finally, assuming the perturbation power spectrum follows Eq. (52), the single-mode approximation of Eq. (55) scales as

$$\alpha_\mu \propto \frac{1}{\lambda^2} \times a^2 \times \frac{1}{\left(\frac{\lambda}{a^2}\right)^{2p}} \propto \frac{a^{2+4p}}{\lambda^{2p+2}}. \tag{56}$$

For $p = 2$, the microbending loss scales as a^{10}/λ^6, which is a very strong dependence on the core size.

The steep scaling relationship with the core size explains why the core cannot be enlarged indefinitely in HCFs to reduce the intrinsic loss contributions without penalty. The $1/\lambda^6$ scaling implies that the total loss increases very sharply at short wavelengths. In our NANF example, when the single-mode approximation holds, loss which is 0.01 dB/km at 1.5 μm increases to approximately 1 dB/km at 0.7 μm. This may point to one of the reasons why it is often difficult to simultaneously achieve low loss in the same fiber in the IR and in higher antiresonant windows at shorter wavelengths.

When the curvature power spectrum of the microbending perturbation decreases with spatial frequency, Eq. (55) shows that an effective approach to reducing microbending penalties is by enlarging $\Delta\beta = \beta_0 - \beta_1$. In standard solid-core single-mode fibers, β_1 is replaced by $\bar{\beta}_r$ understood as the average propagation constant of the radiation modes to which light is coupled. Although in SMFs, low-refractive-index trenches outside the core have proved effective at enhancing $\beta_0 - \bar{\beta}_r$ and reducing the microbending loss [218,235], $\beta_0 - \beta_1$ in HCFs is determined by the core size.

3.1b. Effect of Fiber Coating and Cabling

An effective route to reducing microbending loss in standard single-mode fibers is through adequate packaging of the fiber [213]. Nowadays, the most widely adopted strategy is the application of carefully developed and optimized UV-curable polymeric coatings onto the fiber during fabrication [213]. The combination of a soft primary coating which serves in a way as a shock absorber for microbend-inducing lateral loads on the fiber, and hard secondary coating to facilitate fiber handling and processing is now industry standard for telecom fibers [219].

Over the years, many studies have explored and optimized the design of such a dual coating to effectively shield the standard solid-core fibers from external loads. In his seminal work on the topic, Gloge showed that essentially, the coating assembly behaves as a low-pass filter for external perturbations whereby components with spatial frequency higher than a cutoff given by fiber stiffness and coating moduli are effectively absorbed by the coatings [213]. Further refinements have now shown that the effectiveness of the fiber's packaging in shielding the fiber from distributed external perturbations can be captured by a mechanical transfer function (MTF). The curvature power spectrum of the fiber axis is thus generally expressed as [231]

$$\Xi(\kappa) = MTF(OD, t_p, t_s, E_p, E_s, \kappa)\Xi_{ext}(\kappa) \approx \frac{A(OD, t_p, t_s, E_p, E_s)}{\kappa^{2p}}, \tag{57}$$

where OD is the bare glass fiber diameter, t_p, t_s, E_p, and E_s the thicknesses and Young's moduli of the primary and secondary coatings, respectively, and $\Xi_{ext}(\kappa)$ is the power spectrum of the external perturbations. Deriving an expression for the MTF is beyond the scope of this paper and we would refer the reader to the works in Refs. [213,219,227,231,236,237]. From this literature, however, it is possible to express it as proportional to

$$MTF \propto OD^{-6}(t_p + t_S)^{-x}(E_p/E_s)^y, \tag{58}$$

where x and y are some characteristic constants usually obtained from statistical experimental data. Because the spatial frequencies that are responsible for coupling from fundamental (i.e., $\beta_0 - \beta_1$) are much smaller than in single-mode fibers, controlling the MTF in HCFs is of crucial importance to reduce their microbending loss sensitivity. In order to do so, a bespoke packaging strategy has to be developed. The heuristic mechanical transfer function suggests that this may take the form of increased fiber's glass diameter, increased coating thicknesses, and exploring the possibility of using bespoke coatings optimized to filter out external perturbations at the relevant spatial frequencies [218]. The final research direction is that of producing HCFs with ultralow leakage loss at smaller core sizes. For example, for the same MTF, reducing the core size from 30 to 25 μm will reduce the microbending sensitivity by a factor of 6.

3.2. Transverse and Longitudinal Geometrical Deformations

In conventional fibers, the geometry of the waveguide usually possesses a cylindrical symmetry, greatly simplifying the analysis of geometric or material perturbations and the effect they may have on the loss and other optical properties [119,171,238]. In HCFs that possess this symmetry like Bragg fibers, theoretical tools have also been developed to study the effect of such perturbations [54,174,239].

However, because PBGFs and ARFs incorporate a large number of material boundaries and do not possess the simple cylindrical symmetry, there exists a myriad of possibilities for geometric perturbations. Any study of their effect on the loss and other optical properties of the fibers cannot consider all of the possibilities. However, some of the most important can be studied and some useful conclusions obtained.

One may make the distinction between two broad classes of geometrical perturbations. The first is a departure of the geometry under study from the ideal fiber which remains constant along the length of the fiber. These are, for example, in the case of PBGFs, a deformation or asymmetry of the core, non-uniform thickness of the core boundary, or a deviation of the cladding from the perfect idealized structure [74,135]. In ARFs, this may mean an azimuthal misalignment of one or many of the tubes, a change in thickness along the circumference of the tube, non-uniform thickness among the cladding tubes, etc. This class of perturbations in fibers can be thought of in a way as inherited from the macroscopic preform from which the fiber is made or resulting from some consistent reproducible effect in the fabrication process. Such perturbations or non-idealities affect the optical properties of the fibers by introducing cladding or surface modes which may interact strongly with the desired core modes, resulting as we have seen in an increase in leakage loss, often accompanied by a narrowing of the usable bandwidth of the fiber.

When such perturbations are longitudinally invariant, their effect can be directly studied with the help of numerical mode solvers and their properties can be compared with those of fibers with idealized geometries. For example, in PBGFs, core asymmetries and the impact they have via the introduction of surface modes has already been explored [74,135]. In ARFs, the impact of a slightly broken symmetry of the fiber cross section is often reported and more comprehensive studies of this type of perturbations are now being undertaken [240]. The net effect often is, as may be expected, an increase in leakage loss and narrowing of the usable bandwidth. For long lengths of fiber, these perturbations may vary along the fiber length, making it equivalent to spliced sections of fibers with different guidance properties. It has been argued that this could lead, for example, to the loss of the photonic bandgap [69]. We believe, however, that such perturbations and their effect will be best addressed via improvements in the fiber fabrication processes.

The second class of perturbations are small changes in the geometry, typically much smaller than the relevant waveguide dimensions or wavelength, that change randomly along the fiber length. These are random variations in the dimensions of the structure such as the fiber diameter or the azimuthal position and diameter of each of the cladding tubes, and may result from random fluctuations of the key parameters of the fiber-draw process. The complexity of the geometry means that the possibilities for such perturbations are innumerable. However, their general effect when present, will be to scatter light from one core-guided mode into other guided modes, cladding modes, and radiation modes. This effect can be studied with coupled mode/coupled power theory as outlined previously. If the perturbation of interest can be expressed as a perturbation operator $\Delta\hat{A}$, then Eq. (53) can be solved to find the effect of the perturbation on the propagation, with the power coupling coefficient given by Eq. (50), with a_{kl} given by Eq. (44) (the new $\Delta\hat{A}$ replaces the bend perturbation operator). In many cases, however, the perturbation cannot be described by an analytical perturbation operator $\Delta\hat{A}$, making the computation of the coupling coefficients rather difficult. However, the coupling coefficients can be calculated alternatively by first obtaining an induced volume current $\mathbf{J}$ as we did when analyzing roughness scattering. In this case, the amplitude coupling coefficient is simply given by

$$a_{kl} = \int_0^L \iint_{A_\infty} \mathbf{E}_l^* \cdot \mathbf{J}_k \, dA \, dz, \tag{59}$$

where $\mathbf{J}_k$ is the induced current density when the mode $|\psi_k\rangle$ is propagating in the section of length L of fiber.

The first example we consider here is that of random diameter fluctuations along the fiber length. We assume a uniform scaling of waveguide dimensions, i.e., a map such that $x' \mapsto (1+\delta(z))x$ and $y' \mapsto (1+\delta(z))y$ where $\delta(z)$ is a small perturbation. Following the coupled-mode formalism described in Refs. [174,241], we find after some algebra that to the first order in δ, this mapping corresponds to a perturbation operator $\Delta\hat{A}$ such that the amplitude coupling coefficient between modes is simply

$$\begin{aligned} a_{kl} &= \langle \psi_l | \Delta\hat{A} | \psi_k \rangle \\ &= \frac{\omega}{c} \iint \begin{bmatrix} E_x \\ E_y \\ E_z \\ H_x \\ H_y \\ H_z \end{bmatrix}_l^\dagger \begin{pmatrix} & & x\varepsilon\delta'(z) & & & \\ & & y\varepsilon\delta'(z) & & & \\ x\varepsilon\delta'(z) & y\varepsilon\delta'(z) & -2\varepsilon\delta(z) & & & \\ & & & & & x\mu\delta'(z) \\ & & & & & y\mu\delta'(z) \\ & & & x\mu\delta'(z) & y\mu\delta'(z) & -2\mu\delta(z) \end{pmatrix} \begin{bmatrix} E_x \\ E_y \\ E_z \\ H_x \\ H_y \\ H_z \end{bmatrix}_k dA, \end{aligned} \tag{60}$$

with $k \neq l$ and where $\delta'(z)$ represents a derivative. It is then easy to work out from here that the power coupling coefficient takes the form of

$$h_{kl} = \left((\beta_k - \beta_l)^2 \, |I_1|^2 + 4\,|I_2|^2 \right) \tilde{\Psi}(\beta_k - \beta_l), \tag{61}$$

with $\tilde{\Psi}$ the PSD of the diameter fluctuations $\delta(z)$ and I_1 and I_2 the integrals from Eq. (60) proportional to $\delta'(z)$ and $\delta(z)$, respectively. When the fiber is effectively single mode, the added loss to the fundamental mode resulting from these fluctuations is $\sum_l h_{0l}$. The difficulty in obtaining the loss in this way is the large number of modes required. In Fig. 31, we show the additional loss incurred by our example NANF (see Fig. 7) for random diameter fluctuations using only the first 50 core and cladding modes found by the finite-element solver. We assume here that the perturbations have

Figure 31

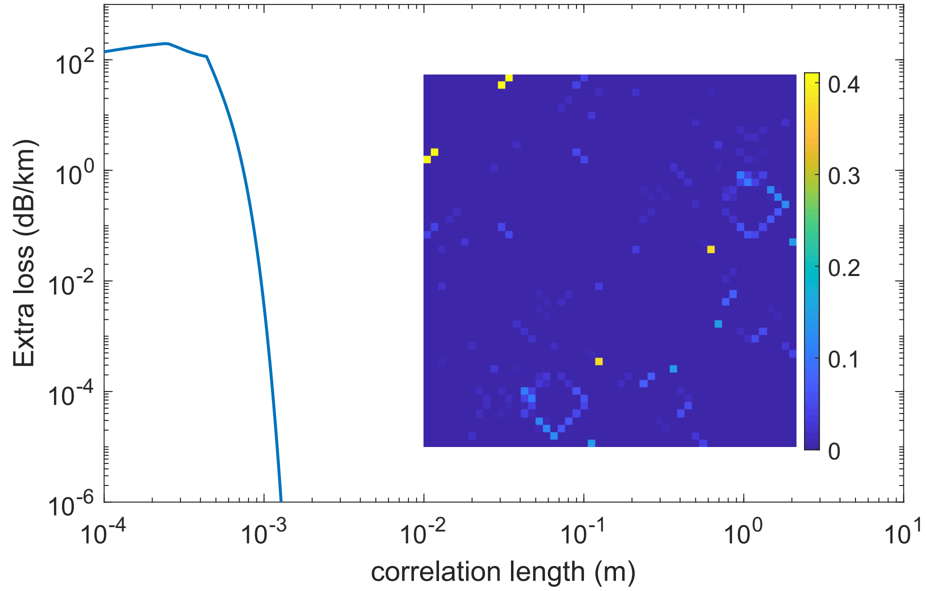

Additional loss induced by diameter fluctuations in our example NANF. The assumed perturbation has a Gaussian PSD with a r.m.s. value of 1%, and the loss is plotted as a function of the correlation length. The inset shows the calculated diameter fluctuation-induced mode coupling matrix (similar to Fig. 23) for a correlation length of 500 µm. For longer correlations than about 1 mm, the wavelength examined here (1550 nm) is unaffected by diameter fluctuations.

a Gaussian power spectrum with a 1% mean square and plot the loss as a function of the correlation length at 1550 nm. As may be expected, diameter fluctuations couple modes of the same azimuthal symmetry as can be appreciated from the coupling matrix. As the longest coupling length between the fundamental mode and modes of the same symmetry is that between it and the LP_{02} mode and is of the order of 460 µm, we see that diameter fluctuations with correlation lengths shorter than about 1 mm can cause significant added loss. With the limited number of modes considered here, fluctuations with longer correlation lengths do not appear to cause noticeable loss penalty. As rapid fluctuations of the diameter on the order of 1 mm are typically not observed in practice, we believe that small diameter perturbations (1% or smaller) on realistic length scales, i.e., 1 m or longer, will have minimal effect on the fiber loss away from resonant wavelengths. Random ellipticity fluctuations can be treated in exactly the same way as previously, and their effect as one may deduce is the introduction of birefringence as has been well documented elsewhere [119,241].

In the next example, we consider that one of the big tubes in the NANF has a random thickness variation along the length of the fiber. In such a case, we can use the tools derived in Section 2.4.1 to directly compute the light scattered and lost to radiation. One distinction, however, is that in the case of thickness fluctuations, the perturbation on the outer and inner surfaces of the membrane are perfectly correlated. It follows, therefore, that the far-field scattered power distribution is

$$\mathbf{S}_k(\vec{R}) = \frac{\omega^4 \varepsilon_0^2 \mu}{32\pi^2 R^2 c} L\tilde{\psi}\,(\beta_k - k\cos\theta)\,\vec{r} \left| \sum_{m=1,2} \oint_{C_m} \vec{U}(s) e^{jk(\rho' \sin\theta \cos\phi - \phi')}\, ds \right|^2, \qquad \textbf{(62)}$$

where $m = 1$ or 2 for the inner and outer interface of the tube. In case many tubes are perturbed, we can calculate the far-field scattered power for each tube as previously and perform a summation over all of the perturbed tubes. We plot in Fig. 32 the scattering

Figure 32

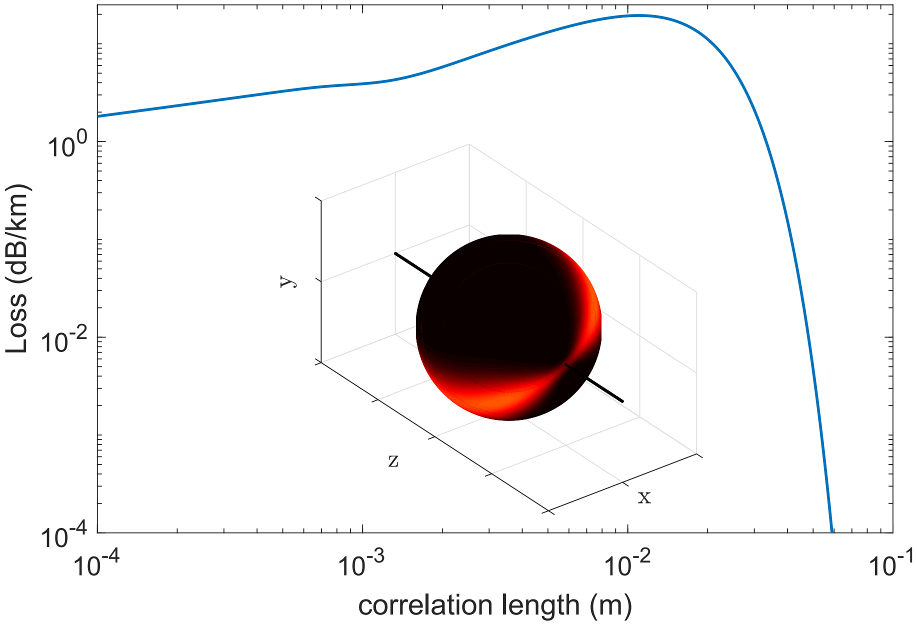

Extra loss induced by thickness fluctuations of a single large tube in a NANF. The inset shows the far-field distribution of the power scattered by the tube with thickness fluctuations. The assumed perturbation is Gaussian with a r.m.s. of 1% membrane thickness (~5 nm). For correlation lengths of 3 cm or less, the fiber can incur significant added loss.

loss that occurs for a 1% tube thickness fluctuation assumed to have a Gaussian power spectrum as a function of its correlation length. Shown in the inset is the far-field scattering pattern caused by such a perturbation. We see that for correlations lengths below 1 cm, significant added loss can occur. This added loss shows a peak of about 20 dB/km for a correlation length of approximately 1.1 cm but this then decreases sharply as the correlation length increases further. Although it is possible that short-scale thickness fluctuations exist in fibers, we believe long-range fluctuations are more likely and more compatible with the dynamics of fiber fabrication. Away from resonances, these are unlikely, as the results show, to cause significant added loss. Nevertheless, tools to confirm the magnitude of their potential contribution are of paramount importance in improving the fiber designs as well as the fabrication processes.

3.3. Macrobend Loss

3.3a. Consequences of Macrobending in Optical Fibers

In addition to the microscopic random perturbations examined in the previous sections, HCFs are often deployed in configurations that include some degree of sustained bending at a defined constant bend diameter. Bending of the fiber is of paramount importance, for example, in applications such as sensing where deploying the fiber in a small coiled topology is essential [33]. By introducing a bend to the fibers, the straightness of the propagation path no longer holds, and the modes experience a modification of their field profiles and propagation constants. What ensues is additional loss to radiation. In extreme cases of bend, for example at small bend diameters, the modes of the fiber may cease to be guided.

In general, the induced bend loss can be associated with two distinct mechanisms, namely, transition loss and curvature bend loss [242,243]. The former is the result of power transfer from modes in the straight part of the fiber to radiation modes in the constant-curvature section of the fiber. This transition loss typically accounts for a negligible part of a bent fiber because the transition section is often very short. On the other hand, significant loss can occur in the constant curvature section if it is sustained over a long distance because lossy cladding modes introduced by the bend can couple with the core-guided modes. Such loss inevitably accounts for the majority of the total bend loss.

A quantitative assessment of bending effects in optical waveguides is generally achieved by mapping the curved propagation path of the light in the bent waveguide onto a straight waveguide using conformal optics [242]. In this method, the bent path is conformally mapped to a straight one, but the impact of the curvature of the waveguide is mapped onto its material property, specifically the refractive index distribution is [242,244,245] modified as

$$n_b = n_s e^{\frac{x}{R_b}}, \tag{63}$$

where n_b is the refractive index distribution of the bent waveguide, n_s that of the straight fiber, R_b the bend radius, and it is assumed the bend is along the direction of the x-axis. The effect of the bend can then be studied with the same analytical and numerical tools. We note that this transformation is only an approximation. A more rigorous treatment accounts for the shifting of the material boundaries, an effect which is non-negligible at very small bend radii (where the approximation breaks down completely) and in fibers with high index contrast between their constituent materials such as HCFs. Such a rigorous treatment is found, for example, in the method of transformation optics [246,247]. Nevertheless, for the most relevant and practical deployment scenarios, the approximation provides adequate accuracy.

Figure 33 illustrates the effect of the simple conformal transformation on the index profile of a standard solid-core step-index fiber (SIF) and a cylindrical hole in glass (as studied by Marcatili and Schmeltzer [121]). In the SIF, the tilted index profile introduced by the bend provides the prospect of the core-guided mode being phase matched with a cladding mode, thereby resulting in loss. This observation has informed the main design approach for low-bend-loss solid-core fibers, which is via the introduction of low-index trenches in the cladding to keep the index of cladding modes low when the fiber is bent [248,249]. In the HCFs (an example in Fig. 33(b)), even

Figure 33

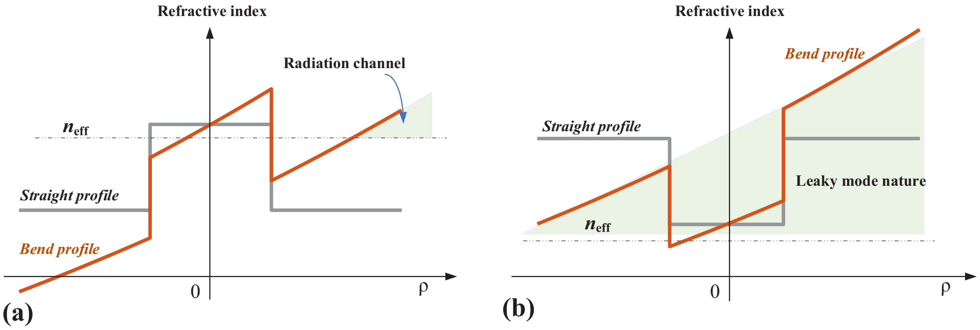

Equivalent refractive index distribution in bent waveguides obtained by conformal transformation. The bent waveguide is equivalent to a straight waveguide with a tilted refractive index profile, with the index increasing from the inside to the outside of the bend. (a) In solid-core SIFs, the bend introduces new lossy cladding modes to which the core mode can couple. (b) Similarly, in a HCF, the leakage is exacerbated by the introduction of higher effective index lossy cladding modes.

when straight, the modes suffer from leakage loss due to the cladding being capable of supporting phase-matched radiation modes. Once the bend modifies the index profile of the waveguide, the leakage is enhanced further.

For further insight into a quantitative analysis of the effect of macrobends, we note that a bend sustained over a long length of fiber can be treated as the limit of a waveguide with a very large number of small tilts [159]. We have seen in Section 3.1 that the effect of a small tilt is to couple light from an incident mode into other guided modes and radiation. One may therefore consider that for a bend sustained over long distance, it is possible to express the eigenmodes of the bent waveguide as a linear expansion of the modes of the straight fiber. For bend radii much larger than the fiber diameter, the modes are only slightly perturbed. In such a case, a second-order correction to the propagation constant (because the first-order correction vanishes under the bend perturbation) is [54]

$$\Delta\beta_k = \sum_{l\neq k} \frac{\left|\langle\psi_l|\Delta\hat{A}|\psi_k\rangle\right|^2}{\beta_k - \beta_l}, \tag{64}$$

where $\langle\psi_l|\Delta\hat{A}|\psi_k\rangle$ is given by Eq. (45) and the summation extends over all core, cladding, and radiation modes. From this expression, if the modes are associated with a loss α_k in the straight fiber in the form of a small imaginary part to the propagation constant, one may extract the loss due to bend from Eq. (64) as [54,250]

$$\alpha_{bend,k} = \sum_{l\neq k} \frac{\left|\langle\psi_l|\Delta\hat{A}|\psi_k\rangle\right|^2}{(\Re(\beta_k - \beta_l))^2}(\alpha_l - \alpha_k). \tag{65}$$

This expression, phenomenologically similar to Eq. (13), provides powerful insight. First, because from Eq. (45), $\langle\psi_l|\Delta\hat{A}|\psi_k\rangle$ is proportional to $1/R_b$, it follows that the bend loss scales as $1/R_b^2$. This inverse square law dependence on bend radius for large bend diameters has been confirmed in Ref. [250]. This scaling does not hold at small bend radii because such tight bends cause strong mode mixing and introduce new cladding modes whose propagation constants depend on R_b. Skorobogatiy *et al.* show that in this regime, the bend loss scale instead as $1/R_b$ [250]. Second, if the bend modifies cladding modes in such a way that their phase index matches that of the core mode of interest, this can result in extremely high loss for that core mode (i.e., $\alpha_{bend,k} \to \infty$ when $\Re(\beta_k - \beta_l) \to 0$). This insight is useful to determine, for example, a critical bend radius for which the bend loss becomes prohibitively high for a desired mode. Such a bend radius is solved for by considering that under bend, the cladding tube mode reaches an effective index equal to that of the core mode, see, for example, Refs. [251–253]. Interestingly, if the cladding modes to which the core-guided modes couple under the bend are discrete, it is possible that the bend loss as a function of bend radius shows discrete resonance peaks separated by relatively low-loss regions, as the discrete cladding modes are phased matched with the core modes at discrete bend radii [254,255]. On an additional practical level, once a design for the cladding is chosen, it is possible to choose an adequate bend diameter that allows to strip unwanted modes, should they be excited at launch into the fiber [256].

We note that in ARFs, a simple scaling of the bend loss with the core size and wavelength is not easily extracted from Eq. (65). This is because increasing the core size comes with a modification of the cladding arrangement and with it, the lossy modes it may support which are further modified by bending. This situation arises because the dependence of the β_l, and α_l on core size, cladding design and wavelength is not analytically tractable at all bend radii. Such scaling may in most cases therefore only be obtained empirically.

Figure 34

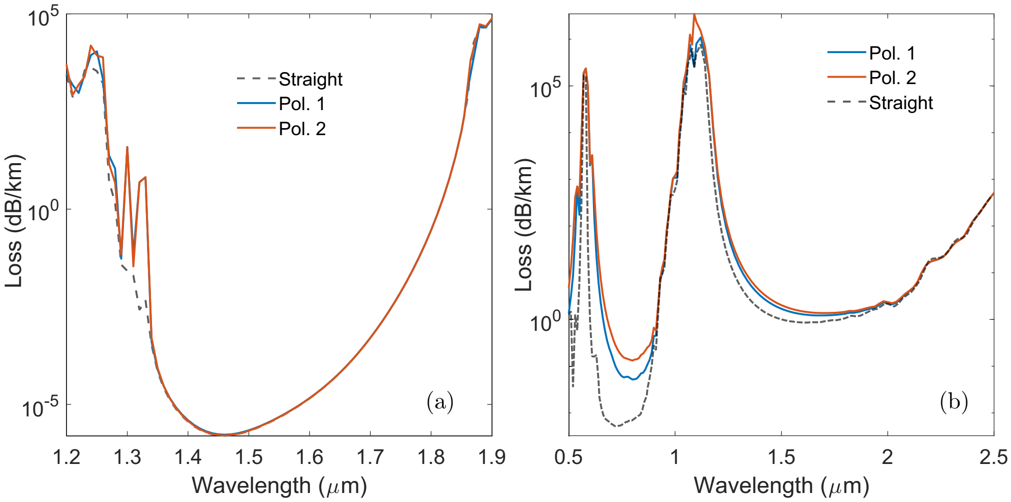

Bend-induced additional leakage loss on a standard shipping bobbin (158 mm diameter) as a function of wavelength for the (a) PBGF and (b) NANF. (a) Bent PBGF incurs virtually no additional leakage loss, as the dashed curve calculated for the straight fiber overlaps with the leakage loss for both polarizations of the fundamental mode under bending. (b) In the NANF, bending induces noticeable added leakage loss and also a small amount of birefringence and polarization-dependent loss (PDL). The bend loss calculated here is for the bend plane bisecting two sets of tubes.

3.3b. Macrobend Loss in HCFs

To examine the loss penalty incurred by PBGFs and NANFs when they are bent, we apply the conformal transformation technique mentioned previously where the bend is mapped onto a modification of the constitutive tensors of the material media of the fiber [242]. After applying such a transformation, we plot in Fig. 34 the leakage loss calculated when the PBGF and NANF of Fig. 7 are wound on a standard shipping spool with approximately 15.8 cm diameter. At this bend diameter, the PBGF suffers virtually no noticeable additional leakage loss. The resilience of PBGFs to bends is well known and documented, and our simulations at the smaller bend radius of 1 cm still show little additional loss near the center of the bandgap, as also confirmed in experiments [257,258]. This comes as no surprise since the same principles that endow them with low leakage loss are at play in keeping their bend loss low. Therefore, we focus the remainder of this section on ARFs, with the NANF of Fig. 7 as an illustrative example. For this NANF, there is a noticeable increase in the leakage loss as a result of the bend, which as we expect from our analysis of microbending is higher at shorter wavelengths. In the specific example here, the leakage loss increases from 1 dB/km when straight to an average of approximately 1.4 dB/km when wound on the shipping spool. We emphasize that this is inextricably linked to our choice in the size of the nested elements. Different bend performance can be expected when the size of these elements is modified. Bending also introduces a small birefringence and a noticeable amount of polarization-dependent loss, see Fig. 35 [206,259]. This can be conceptually understood from the picture of leakage loss as the result of partial reflection (see Section 2.1.1). The bend imposes an additional twofold symmetry about the bend plane and, as a result, the mode polarized in the plane of the bend has its polarization vector substantially more orthogonal to the *core boundary* (thus effectively resembling a *p*-polarized or TM wave) than that polarized orthogonal to the bend plane (*s*-polarized wave). The former suffers higher loss as expected, because it is less effectively reflected by the cladding membranes. We emphasize that bending

Figure 35

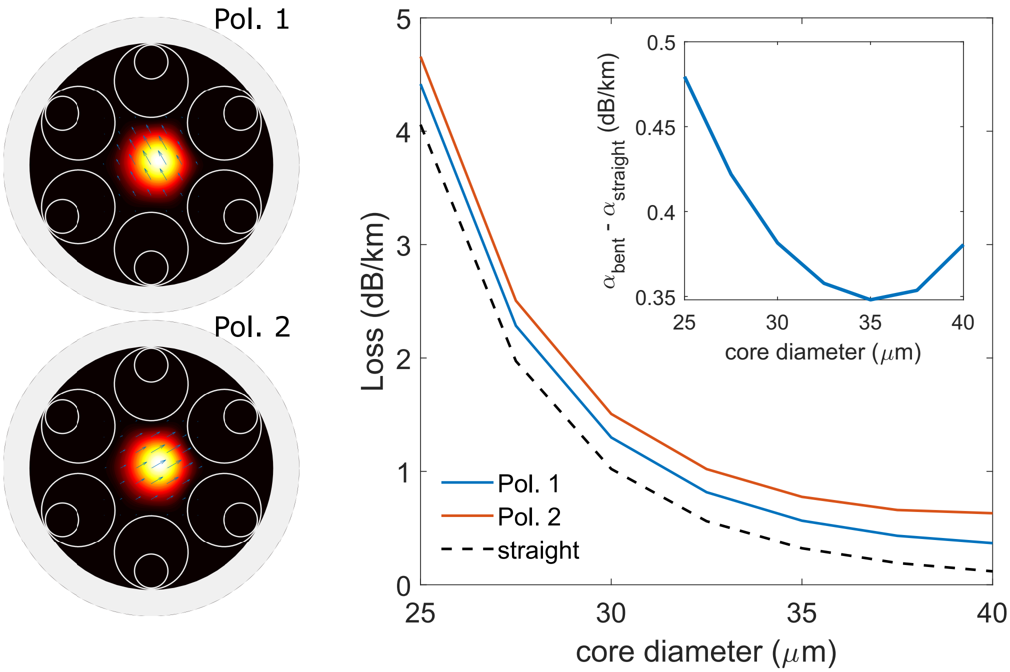

Bend loss in NANFs on a standard shipping bobbin (158 mm diameter) as a function of the core diameter. The inset shows the pure bend loss, i.e., the difference between the leakage loss when the fiber is bent (average between the two polarizations) and when it is straight. The bend plane is perpendicular to the tubes. In this special case, the added loss reaches a minimum around a core diameter of 35 μm.

loss in the NANF depends on its structural parameters and design, notably the core diameter. In Fig. 35, we plot the bend loss as a function of core diameter for a fixed bend diameter of 158 mm. In scaling the core size, the membrane thickness, the ratio between nested tube diameter and core size, and ratio between gap and core diameter are all kept constant. We can observe interestingly that the pure bend loss reaches a minimum around a core diameter of 35 μm (see inset of Fig. 35). This, we expect, would change for a different bend diameter or a different cladding design. Our observations therefore do not apply to all NANF structures, but further illustrate the complexity of how the bend loss scales with core size and wavelength. An in-depth study of macrobending effects in ARFs and NANFs in particular will be presented elsewhere [260]. One additionally expects *a priori* that the sixfold (or generally N-fold) symmetry of the structure results in a dependence of bend loss on the direction of the bend plane. Figure 36(a) shows the bend loss for both polarizations of the fundamental mode for a bend radius of 5 cm as a function of the bend plane azimuth and confirms that this is indeed the case. The total loss as a result of the bend is well expressed by $\alpha_0 + \alpha_1 \cos N\theta$ where theta is the angle between the bend plane and the x-axis. Unsurprisingly, the loss of the in-plane polarized mode (pol. 2) is highest when the bend plane is aligned with the tube (bend azimuth of 0°) and lowest when it is aligned with the gap between tubes (bend azimuth of 30°), and vice versa for the orthogonal polarization.

In Fig. 36(b), we plot the loss for both polarizations when the bend plane is aligned with the tube as a function of bend radius. We can see that for moderate values of the bend radius, i.e., at least 5 cm, the approximate $1/R_b^2$ scaling holds reasonably well. However, the loss increases sharply if the bend radius is reduced further, in this specific case, below a bend radius of 4 cm which may thus be defined as a critical bend radius for the specific NANF considered here [251].

Figure 36

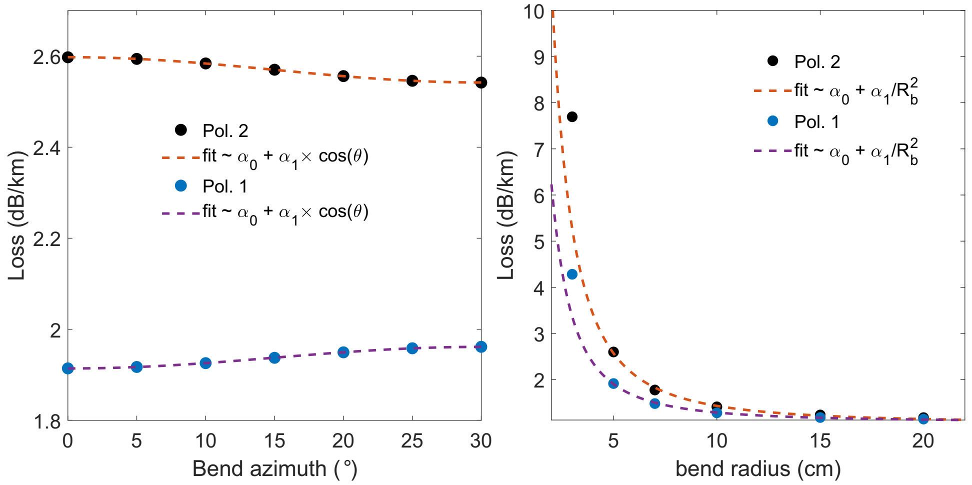

Bend loss in the NANF as a function of (a) bend plane azimuth and (b) bend radius. The bend loss in (a) is calculated at a bend radius of 5 cm. 0° corresponds to the bend plane aligned with the tube, and 30° corresponds to when it is aligned with the gap between tubes. In (b) the bend plane intersects the tube, and for $R_b \geq 5$ cm the loss follows R_b^{-2} as expected.

Clearly, macrobending can be a considerable contributor to loss in hollow-core ARFs and should be given due attention when designing fibers for applications where the deployment effectively involves bends over long distances. Macrobend loss presents a richer picture in these fibers, it is inextricably linked with the design of the fiber, its symmetry, the bend orientation as well as the bend diameter. However, it lends itself to some degree of control and significant reduction in bend loss is possible through engineering the fiber structure. Our analysis in the previous section and in Section 2.1b shows that the key is to ensure that under bend, the cladding structure does not support modes that have a strong overlap and are phase-matched to the core mode of interest. In practice, this may be accomplished through controlling the size of the hollow regions within the cladding. For example, by adding the nested tube to the simple tubular fiber design (see Fig. 9), both the straight leakage loss and bend loss are greatly reduced [52,114]. Using a large number of smaller cladding tubes in a tubular fiber also reduces the bend loss. There are trade-offs in addressing bend loss via these design techniques. For example, using many smaller tubes results in higher straight loss due to the proximity of the glass jacket to the core, whereas partitioning the hollow regions into smaller areas may reduce the loss of higher-order modes, making effective single-mode operation more difficult. Designs such as the double-NANF (DNANF) with five tubes overcome this dilemma by simultaneously providing high intermodal differential loss and low bend loss [45].

4. MINIMIZATION OF TOTAL LOSS

4.1. Loss Analysis in State-of-the-Art HCFs

In this section we use the tools derived in the previous sections to describe the loss in an example state-of-the-art six-tube NANF reported by our team [115]. This example is simply illustrative as the analysis can be (and routinely is) performed on any fiber provided its cross section can be captured accurately from scanning electron microscopy (SEM) images into the finite-element solver.

The fabricated NANF sample had an experimentally measured minimum loss of 0.28 dB/km. The NANF geometry or similar concepts has been the subject of intense

Figure 37

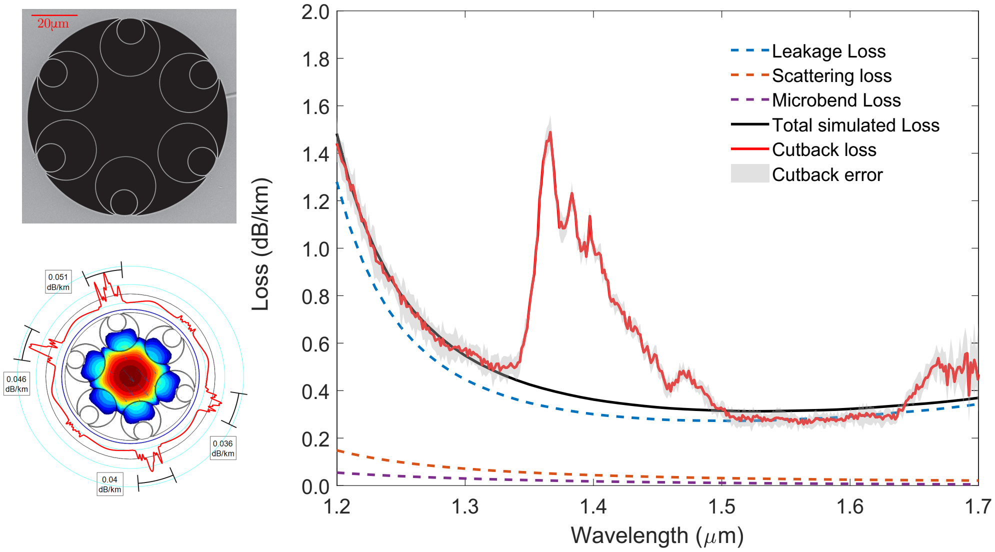

Loss analysis in a state-of-the-art six-tube NANF fiber [115]. The experimental curve (solid red) was measured via cutback from 1700 m to 500 m. This was repeated several times to give the measurement uncertainty (gray area).

research efforts over the past 5 years, resulting in dramatic and sustained loss reduction. We have since reduced the loss for the fundamental mode while increasing higher-order mode loss in the NANFs first to 0.22 dB/km by adopting a five-tube geometry [98] and later to 0.174 dB/km by introducing an additional nested tube [45]. These fibers can be modeled and analyzed in the exact same way. The fiber we analyze here, as can be seen in Fig. 37, consists of six pairs of nested silica capillaries arranged around a central hollow core. From the SEM image of the cross section, we measured an average thickness of 0.5 μm for the outer tubes, with inner tubes approximately 6% thicker. The core diameter was measured to be 34.5 μm and the average gap between the larger tubes was 4.4 μm. We reconstructed the permittivity profile of the fiber from the SEM images by accurately capturing the coordinates of the tubes and, for simplicity, assumed that they were of circular shape and even thickness all around.

Figure 37 shows the modeled loss contributions in the fiber along with the experimentally measured attenuation. We first consider the leakage loss which can be seen to account for nearly all of the loss across the C and L bands. As can be seen, at 1550 nm, the fundamental mode has a leakage loss of 0.27 dB/km, accounting for the near totality of the measured average value of 0.28 dB/km. A closer analysis through examining the azimuthally resolved radial Poynting vector shows that this leakage loss is dominated by power flowing radially outside of the core of the fiber through the tubes (note how most of the light leaks through tubes which are oriented orthogonal to the polarization vector of the fundamental mode). Interestingly, our simulations showed that the LP_{11}-like mode group suffered leakage loss in the 6–10 dB/km range, whereas other higher-order modes incurred more than 1 dB/m loss, making the fiber effectively two-mode. Next, we calculated the scattering loss using Eq. (28) and found it to amount to about 0.027 dB/km. As noted in Ref. [115], this is much lower than the approximately 0.1 dB/km that would be predicted from the empirical scaling of the normalized interface field intensity (Eq. (39)). Using the single-mode approximation of Eq. (55), we estimated an additional microbending loss contribution of 0.02 dB/km. For the microbend PSD, we chose a spectrum of the form A/κ^{2p} with model values

$A = 5 \times 10^5$ and $p = 2$ which provided consistent agreement across many experimental fibers. This gives an estimated total loss for the fundamental mode at 1550 nm of approximately 0.32 dB/km (the steady-state loss plotted in Fig. 37 is ~0.3 dB/km). Within measurement error, this is in very good agreement with experimental data, considering that sources of uncertainty exist both in the experimental measurement and the accuracy with which the fiber profile is reconstructed from the SEM images.

It is noteworthy that this agreement is consistent throughout the transmission window of the fiber, except for the water absorption band between 1350 and 1450 nm and the region beyond 1650 nm, which are instrument artifacts at the long wavelength edge of the optical spectrum analyzer. The level of agreement between the theoretical contributions to loss and the measured value are also a testimony to the already achievable levels of uniformity in the fiber structure along its length, showing particularly that if present, some of the perturbations analyzed in Section 3.2 are on length scales that do not significantly alter the loss of the fiber. Therefore, for ARFs, it is possible to make reliable analysis and predictions on possible fiber performance by relying solely on the three mechanisms of leakage, scattering, and microbending.

4.2. Scaling Rules and Design Optimizations

In this section we summarize our analysis and use the key scaling rules we have established to inform a view on the potential lowest achievable loss in HCFs and the spectral wavelength at which such lowest loss may be obtained.

As we have shown, bar for some model HCF types [123], an analytical expression for the loss at all wavelengths in HCFs remains almost unattainable. However, an empirical prediction for the minima of the key loss contributions is possible and that is what we attempt here. Let us consider that for a given operating wavelength λ_0, we have optimized the design of the cladding to minimize the leakage loss through choice of pitch, air-filling fraction, glass node size, core wall thickness in PBGFs or alternatively, by choosing the membrane thickness, the size, nesting configuration, and arrangement of cladding tubes in ARFs (we consider NANFs for simplicity). For the purpose of the discussion here, we assume that such a cladding design makes the fiber effectively single-mode. The key loss mechanisms we consider in optimizing the designs will be limited to leakage, surface scattering, and microbending. For the purpose of predicting ultimate loss performance, we thus neglect the macrobending loss contribution, which is small when the fibers are wound on large bobbins (see Section 3.3), but which must be considered in applications requiring compact coils. We also do not consider other perturbations, thus assuming that they can be removed by technological improvements or, if present, are on length scales that do not affect the propagation of the fundamental mode (see Section 3.2). Table 1 summarizes the scaling rules for these key loss contributions.

A very important question that arises then is to determine what core diameter provides the lowest possible loss at λ_0. Without considering microbending contributions to loss, both scattering and leakage decrease monotonically with core size and, thus, loss can be made arbitrarily low by choosing ever-larger core sizes. There are, however, practical limitations on the fiber's dimensions and flexibility often imposed by the intended application. With such limitations, the microbending contribution cannot be neglected at all core diameters. As it increases rapidly with core size, there exists therefore an optimum core size for which the total loss is lowest. Without loss of generality, we consider here the example of a six-tube NANF for which a choice of membrane thickness t and cladding tube size and gap between them gives a minimum leakage loss of 0.2 dB/km at 1550 nm in a 35 μm core diameter fiber. The contribution from scattering loss in such a fiber is 0.03 dB/km and the fiber is packaged in a

Table 1. Summary of Scaling Rules for Key Loss Contributions in HCFs

Loss Mechanism	Scaling	Description
Leakage loss	$\frac{\lambda^{l+2}}{a^{l+3}}$	This scaling applies to ARFs, l is the number of antiresonant layers, λ the wavelength, and a the core radius. The exact powers may depend on other geometry parameters such as gap size and size of nested elements. Refer to Section 2.1.
Material loss suppression factor	$\frac{\lambda^2 t}{a^3}$	Fraction by which either absorption or scattering loss in the glass material are suppressed. For ARFs, t is the cladding membrane thickness.
Surface scattering loss: rigidly scaled fibers	$\frac{1}{a^3}$	For a given fiber design scaled rigidly to operate at different wavelengths, the minimum scattering loss scales only with the core size. See Section 2.4d.
Surface scattering loss approximation	$\eta F \left(\frac{\lambda}{\lambda_0}\right)^{2.5}$	Approximation of the rigorous scattering loss for a given fiber across its transmission windows. See Section 2.4e.
Surface roughness-induced intermodal coupling coefficient	$\frac{\lambda^3}{a^6}$	Roughness-induced power coupling rate between core-guided modes. See Section 2.4f and also Ref. [161].
Higher-order mode surface scattering loss or absorption from glass	$\frac{\alpha_{mn}}{\alpha_0} \propto u_{nm}^2$	Ratio between the surface scattering loss or the material loss of the LP_{mn} mode and that of the fundamental mode; u_{nm} is the mth zero of the Bessel function $J_{n-1}(x)$. See Section 2.5.
Microbending loss (single-mode approximation)	$\frac{a^{2+4p}}{\lambda^{2+2p}}$	It is assumed the microbend power spectrum can be expressed as A/κ^{2p}. See Section 3.1.
Macrobend loss	$\frac{1}{R_b^2}$	The scaling is valid when the bend radius R_b is greater than a critical bend radius.

way that the microbending leads to an additional 0.02 dB/km for a total loss of 0.25 dB/km. As shown in Fig. 14, if such a NANF is scaled so that the gap to core radius ratio remains constant at 1/5, the leakage loss decreases with the core as $1/a^{7.5}$. The microbending loss contribution scales as in Eq. (56) with a p-coefficient of $p = 2$ used throughout the paper. In this case, the total loss as a function of core diameter is plotted in Fig. 38. Leakage loss accounts for nearly all of the loss for core diameters smaller than 35 μm and microbending dominates for core sizes larger than approximately 40μm. With these parameters, which are not far from those already achieved (see Section4.1 and Ref. [115]), we see that a loss as low as 0.17 dB/km can be achieved with a core diameter around 39 μm. However, fabricating such large core fibers whilst maintaining control over other cladding parameters may prove challenging in practice and care must be taken to ensure that the fiber remains highly uniform along its length and that its packaging guarantees low levels of microbending loss. Note that for the prediction shown in Fig. 38, we assume that the outer diameter and fiber packaging remains the same as the core size is changed.

Repeating the process with a PBGF for which we assume negligible leakage loss and a surface scattering limited attenuation of 1 dB/km for a 21 μm core diameter, we find, interestingly, that the loss minimum predicted for a core diameter of 41 μm is 0.19 dB/km. Note that this larger core size effectively demands removing a 61 unit cells to make the core defect which gives rise to significant challenges in fabrication and would in effect render void our assumption of single-mode guidance. We do not foresee that such a fiber could be fabricated successfully.

A second and very important question is that of the ultimate low loss achievable in HCFs and at which wavelength this may be achieved. For practically achievable PBGF geometries, i.e., with 19c core defects, the loss is dominated by surface roughness scattering and glass absorption at IR wavelengths. When microbending is neglected,

Figure 38

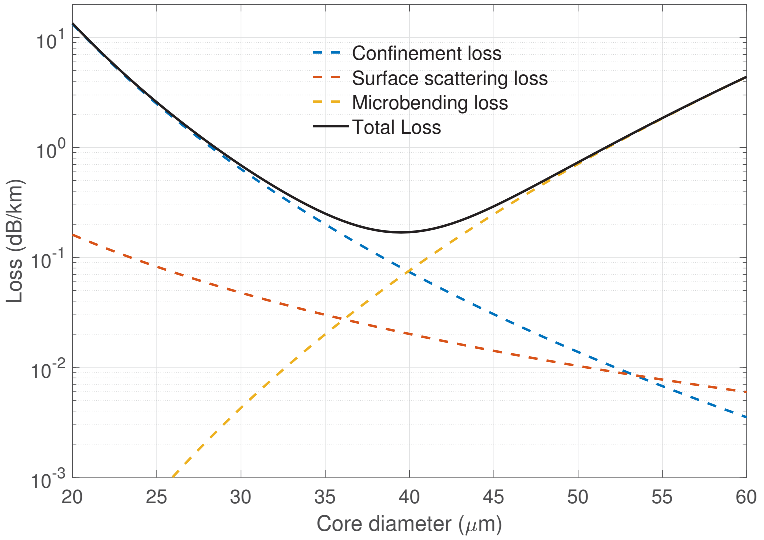

Optimizing the core diameter for a NANF with a six-tube geometry to achieve the lowest possible loss at 1550 nm.

our conclusions are similar to those in Ref. [49], where approximately 0.2 dB/km near 2 μm is predicted.

For ARFs, there is great flexibility in that the membrane thickness which controls the guidance can be adjusted separately of the core diameter with which key loss mechanisms scale. In such a scenario, without the loss contribution from microbending or practical constraints on fiber size and packaging, there is no optimization to be done as the natural choice at any wavelength will be the largest core size possible. Were this to be the case, arbitrarily low loss could be achieved at any wavelength. However low it may be though, the microbending loss contribution must be taken into account and practical limitations on the size of the fiber and its core as well as deployment conditions also play a role. As a result, for each operating wavelength, we can carry out the same optimization as in Fig. 38 to find the core size which provides the lowest loss possible at a given wavelength. Without loss of generality, we assume in the first instance that no improvement in microbending loss is possible beyond what is currently achievable and that all fibers will be restricted to the same outer diameter. Regardless of the wavelength of operation, we thus assume that the fibers are drawn to the same outer diameter and use the same coatings and packaging, thereby making them subject to the same microbending perturbation PSD. Taking the six-tube NANF as an example, we show in Fig. 39 the optimized loss as a function of wavelength from the visible up to 3 μm. For each wavelength, we optimize the core diameter of the fiber so that the combination of contributions from surface scattering, leakage, microbending, and bulk scattering or absorption is minimized. This optimized core diameter as a function of wavelength is plotted in Fig. 39(b). In scaling the leakage loss, we have assumed that the gap between the large tubes of the fibers are kept at a constant fraction of the core radius ($g = a/5$). For longer wavelengths, we also include the absorption from the glass. For simplicity, IR vibrational absorption as $\alpha_{IR} = 6 \times 10^{11} \exp(-48/\lambda\ [\mu\text{m}])$ [152] (this provides an adequate approximation to the data available from Heraeus up to approximately 3 μm [162]). The Rayleigh scattering in the glass may also be accounted for, for example by taking the Rayleigh scattering coefficient of pure silica as $\alpha_R = 0.11 \times (1.55/\lambda[\mu m])^4$ [43,152], though we found it plays a negligible role.

Figure 39

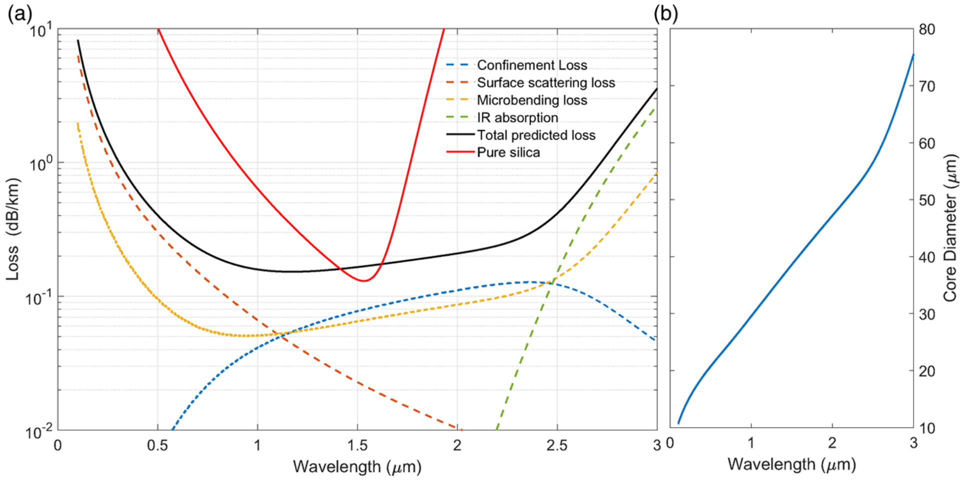

(a) Predicted achievable loss values in six-tube NANFs geometries operating from 0.2 to 3 µm. For each wavelength, we optimize the core size to obtain the minimum total loss made of contributions from leakage, surface scattering, and microbending loss. At wavelengths beyond 2 µm, IR absorption from the glass is also considered. For all wavelengths, microbending is calculated by assuming the same outer diameter and polymer coatings. Surface scattering dominates at wavelengths below approximately 1 µm and glass absorption beyond about 2.5 µm. The red curve shows the ultimate loss achievable in pure silica core fibers across the same wavelength range. With the imposed limitations, the six-tube NANF outperforms pure silica at all wavelengths, except for a narrow spectral region around the C-band. (b) Core diameter of each optimized fiber.

Our results shown in Fig. 39 paint an interesting picture. For this six-tube NANF geometry, we see that at wavelengths shorter than about 1 µm, surface scattering is the biggest contributor to loss. Below 0.5 µm, the leakage loss is very low. The implication is that more complex designs which primarily further reduce the leakage loss at similar core sizes are not necessary for fibers operating in this region. Thus, in principle, the simpler tubular designs can be optimized to provide the lowest loss possible in this spectral region (see, for example, Ref. [109]). Similarly, at wavelengths beyond about 2.5 µm, the loss is dominated by IR absorption. Although the leakage loss is relatively high for the somewhat small core diameters of the six-tube NANF, this also means that the simpler tubular design can be optimized to provide very low loss, for example by increasing the number of tubes, the core size, and the fiber diameter to lower the microbend contribution. Between 1 and 2.5 µm, leakage and microbending are the biggest loss contributors. This is the spectral region where significant loss reduction is possible via tweaking the cladding design to allow further reduction of leakage and microbending loss. For the six-tube NANF geometry adopted here, the loss minimum of approximately 0.15 dB/km is obtained near 1.2 µm. (We emphasize that this is specific to the geometry we are studying. The number of cladding tubes, gap between tubes, and size of nested element can all be changed to further reduce the loss.) We also plot the ultimate loss of pure silica fibers for comparison in red. As can be seen, the lowest loss achievable with experimentally demonstrated six-tube NANF designs is lower than that of pure silica across all wavelength regions, except in the C-band where it is higher by a few hundredths of decibels per kilometer. We reiterate that this is simply a limitation of the specific six-tube NANF design explored here for illustrative purposes only. By providing lower leakage loss, alternative structures such

Figure 40

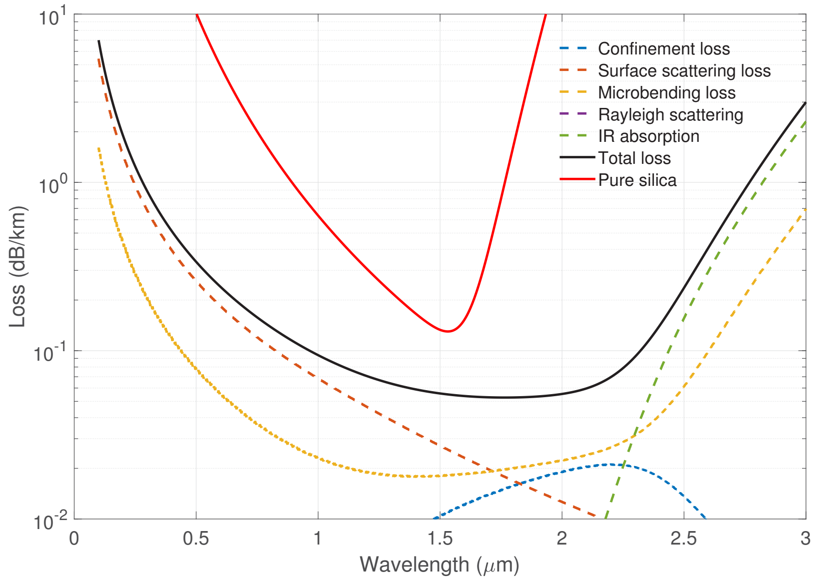

Predicted achievable loss in DNANF fibers as a function of wavelength. We assume a reduction of half in current microbending loss levels. As can be seen, the DNANF would outperform pure silica at all wavelengths from visible to mid-IR, with a remarkable minimum loss of 0.053 dB/km at 1.75 μm and only 0.055 dB/km at 1.55 μm.

as the five-tube NANF (3–4 times lower) or our recently reported five-tube DNANF which we examine next (10–20 times lower) simply outperform pure silica fibers at all wavelengths. This means that with their other attractive properties, hollow-core ARFs offer strong competition to traditional silica fibers and may well replace them in the long run.

4.3. Outlook and Future Prospects

We now take a look at what the future might hold for HCF technology. The continuing rapid pace of development and improvement in performance means that the predictions we make here may well be fulfilled or obsolete by the time the reader reads this section. We base our projections here not on as yet unrealized and promising fiber designs, but on the DNANF structure we reported recently [45]. As the dynamic research field continues to advance, we believe that significant loss reduction is possible and we will soon see reports of ever more transparent fibers with unprecedented low loss values. To illustrate why, we note that as shown in Ref. [45], for a similar core size, the DNANF can provide more than 10 times lower leakage loss compared with a five-tube NANF. We make projections here with the somewhat conservative value of leakage loss of 0.02 dB/km in a 35 μm core diameter DNANF. The surface scattering remains the same for the same core size (0.03 dB/km), as does the microbending contribution (0.02 dB/km) if the fiber is drawn to the same outer diameter. We assume that, with further likely improvements in coating and cabling technology, fiber packaging can be improved to give an overall two times reduction on the microbending loss contribution, bringing it to 0.01 dB/km. If this can be achieved, a loss of only 0.06 dB/km would seem possible, less than half the lowest-loss single-mode fiber [42,261].

With this assumption, we show in Fig. 40 our predictions for the loss values that can be achieved for such a DNANF and again, for reference, the loss limit of pure silica core fibers across the same spectral range. As may be expected, the DNANF

Figure 41

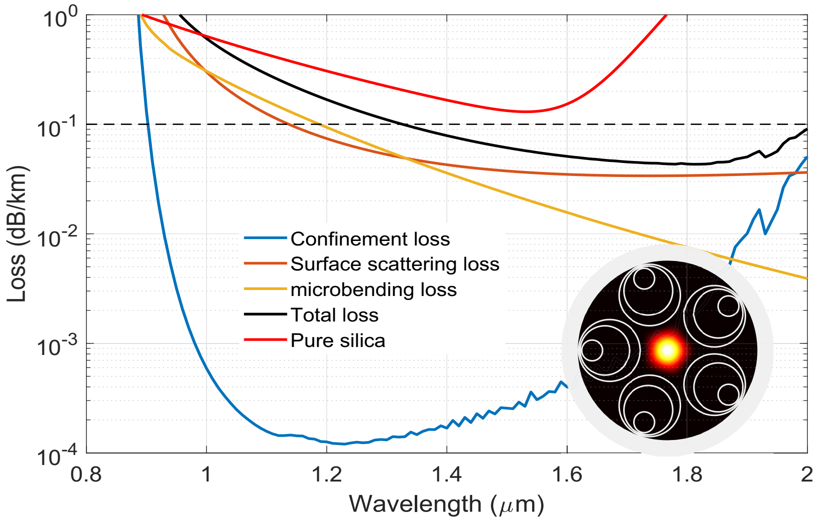

Simulated attenuation of a DNANF with optimum core size operating near 1550 nm. The fiber uses five sets of double-nested tubes and has a core diameter $2a = 35\ \mu$m, a membrane thickness of 408 nm, and a gap between the tubes $a/5$. The double-nested structure results in a significant reduction in leakage loss to a minimum of only approximately 10^{-4} dB/km and the loss is, thus, dominated by surface roughness scattering and microbending. The fiber achieves a total loss less than 0.1 dB/km between 1320 nm and 2 μm

can be tailored to have lower loss than the most transparent material known to date at all wavelengths from the UV to the mid-IR. We predict, with our self-imposed limitations on microbending, a remarkable minimum loss of 0.053 dB/km near 1.75 μm. In contrast to the six-tube NANF, microbending is the biggest contributor to loss in this low-loss spectral region (1.7–2.2 μm) and scattering or absorption dominate at either side of it. To further illustrate that these predictions are conservative and cautious, we plot in Fig. 41 the loss of a DNANF with an optimized core diameter of 35 μm and membrane thickness of 408 nm. This choice of thickness ensures the low-loss region is achieved below 2 μm where absorption does not contribute to loss and is therefore neglected. For this DNANF structure, the minimum leakage loss near 1.25 μm is only approximately 10^{-4} dB/km. Surface roughness and microbending dominate the total loss. Remarkably, the fiber achieves a loss below 0.1 dB/km from 1320 nm to 2μm, 0.055 dB/km at 1550 nm, and a minimum of 0.043 dB/km at 1780 nm.

Could loss be reduced beyond these predictions for the DNANF? It is possible that some other, as of yet undiscovered ARF designs may offer leakage loss levels rivalling that of PBGFs, but that would leave surface scattering, absorption, and microbending. If the latter is reduced by a further factor of 10, as one can see from Fig. 40, with only surface scattering (dashed orange curve) and IR absorption (dashed green curve) contributing to loss, the minimum loss would be predicted where they cross, near 2.2 μm, and in this speculative scenario, would be of the order of 0.02 dB/km.

Such fibers would effectively usher in vacuum-like optical guidance properties in flexible waveguides and over long distances, revolutionizing telecoms [202], and transforming many fields in which optical fibers have traditionally been used, such as sensing [206] and laser power delivery [262]. It is our belief that in the not-too-distant future the first less than 0.1 dB/km fiber will be reported and it will likely take the form of a hollow-core antiresonant optical fiber. Only time will tell whether loss reduction beyond these already impressive values might be achievable or not.

5. CONCLUDING REMARKS

Hollow-core optical fibers represent arguably one of the most exciting developments in optical fiber technology in the recent past. From the early excitement following the introduction of the HC-PBGF structure in 1999, to the somewhat disappointing realization that surface scattering may limit the loss in such fibers to values five to six times higher than in glass-guiding versions in the C-band, and back again to the re-ignition of the initial excitement thanks to transversally antiresonant structures, the field has developed enormously. It now sits on the cusp of transforming all application areas in which light guidance in its purest form is needed, while uniquely enabling several new ones.

A fundamental understanding of the basic mechanisms that contribute to attenuation in such fibers is of paramount importance to enable the realization of fibers with unprecedentedly low levels of loss. In this paper, we have presented a theoretical analysis of these loss mechanisms based on the best current understanding. Our theoretical analysis accounts for intrinsic loss mechanisms such as leakage loss, arising from the unique guidance mechanisms of HCFs, scattering and absorption within the bulk glass of the fiber or in the gas-filled hollow regions, and scattering from surface roughness. It is our hope that the rigorous analysis of this latter loss mechanism will prove useful to researchers in the field when designing fibers and analysing their loss characteristics. One important distinction with solid-core fibers is that higher-order transverse modes in HCFs inevitably suffer from higher losses, with all these intrinsic contributions higher than that of the fundamental mode, and often significantly so. This differential loss mechanism, which in ARFs can be tailored by controlling the phase constant of cladding modes, is the reason why hollow fibers with core diameters many tens of times larger than the optical wavelength can be realized with an effective quasi-single-mode operation.

Turning our attention to the extrinsic loss mechanisms in the fibers, we examined how randomly distributed geometrical changes to the fiber structure along its length can scatter light from one mode of the fiber to the other, resulting ultimately in loss and intermodal power coupling. We have identified, in particular, random microbends as a mechanism that imposes practical limitations to the size of the core, although their contribution to loss and intermodal coupling can, in principle, be reduced through careful coating and cabling of the fiber. Lastly, we explored the loss suffered by HCFs when deployed at a constant radius of curvature as is often the case in applications such as interferometers or compact sensors.

The scaling rules we have identified for the key loss contributions mean that in practical scenarios where microbending (and/or macrobending if the application requires tight coiling) imposes a limit on the size of the core of the fiber, there exists an optimum core diameter which minimizes the total loss at a given wavelength. Using this, we have carried out numerical projections showing that ARFs of the NANF geometry similar to those reported in the literature (we considered specifically a NANF with six sets of nested tubes) can have losses at 1550 nm as low as 0.17 dB/km, marginally higher than pure silica and on par with commercial Ge-doped single-mode fibers. At shorter and longer wavelengths than in the C-band, such fibers are predicted to have significantly lower loss than pure silica, as a few experimental demonstrations have already shown. We further predict that other ARF structures such as the recently reported DNANF, which allow for significant leakage loss reduction, have the potential to ultimately outperform any existing all-solid optical fiber technology at all wavelengths. According to the models presented in this work, a loss potentially as low as 0.05 dB/km would seem achievable in optimized DNANFs. If proven experimentally, this could usher in a new era of optical fiber technology.

FUNDING

Engineering and Physical Sciences Research Council (EP/P030181/1); Royal Academy of Engineering (RF\201819\18\200); H2020 European Research Council (682724).

ACKNOWLEDGMENTS

We are grateful to many colleagues past and present for stimulating discussions and valuable insight: John Hayes, Yong Chen, Thomas Bradley, Hesham Sakr, Natalie Wheeler, Marco Petrovich, Ian Davidson, Austin Taranta, Wei Wang, Reza Sandoghchi, and Radan Slavík. Eric Numkam Fokoua acknowledges support from a Royal Academy of Engineering Research fellowship. This work was also supported by the Engineering and Physical Sciences Research Council (EP/P030181/1: Airguide Photonics) and by the H2020 European Research Council (682724: Lightpipe).

DISCLOSURES

The authors declare no conflicts of interest.

DATA AVAILABILITY

Data underlying the results presented in this paper are available in the University of Southampton’s repository [263].

REFERENCES

1. R. F. Cregan, B. J. Mangan, J. C. Knight, T. A. Birks, P. S. J. Russell, P. J. Roberts, and D. C. Allan, “Single-mode photonic band gap guidance of light in air,” Science **285**, 1537–1539 (1999).
2. E. Yablonovitch, “Inhibited spontaneous emission in solid-state physics and electronics,” Phys. Rev. Lett. **58**, 2059–2062 (1987).
3. S. John, “Strong localization of photons in certain disordered dielectric superlattices,” Phys. Rev. Lett. **58**, 2486–2489 (1987).
4. T. A. Birks, P. J. Roberts, P. S. Russell, D. M. Atkin, and T. J. Shepherd, “Full 2D photonic bandgap in silica/air structures,” Electron. Lett. **31**, 1941–1943 (1995).
5. A. Maradudin and A. McGurn, “Out of plane propagation of electromagnetic waves in a two-dimensional periodic dielectric medium,” J. Mod. Opt. **41**, 275–284 (1994).
6. P. Russell, “Photonic crystal fibers,” Science **299**, 358–362 (2003).
7. P. S. J. Russell, “Photonic-crystal fibers,” J. Lightwave Technol. **24**, 4729–4749 (2006).
8. P. Russell, “Photonic crystal fibers: a historical account,” IEEE LEOS Newsl. **21**, 11–15 (2007).
9. F. Benabid and P. J. Roberts, “Linear and nonlinear optical properties of hollow core photonic crystal fiber,” J. Mod. Opt. **58**, 87–124 (2011).
10. F. Poletti, M. N. Petrovich, and D. J. Richardson, “Hollow-core photonic bandgap fibers: technology and applications,” Nanophotonics **2**, 315–340 (2013).
11. D. G. Ouzounov, F. R. Ahmad, D. Müller, N. Venkataraman, M. T. Gallagher, M. G. Thomas, J. Silcox, K. W. Koch, and A. L. Gaeta, “Generation of megawatt optical solitons in hollow-core photonic band-gap fibers,” Science **301**, 1702–1704 (2003).
12. A. V. Newkirk, J. M. Mercado, E. A. Lopez, R. A. Correa, and A. Schulzgen, “High power laser delivery using anti-resonant hollow core fiber,” in *Photonic Fiber and Crystal Devices: Advances in Materials and Innovations in Device*

Applications XV, Vol. 11826, S. Yin and R. Guo, eds., International Society for Optics and Photonics (SPIE, 2021), pp. 38–41.

13. J. D. Shephard, A. Urich, R. M. Carter, P. Jaworski, R. R. J. Maier, W. Belardi, F. Yu, W. J. Wadsworth, J. C. Knight, and D. P. Hand, "Silica hollow core microstructured fibers for beam delivery in industrial and medical applications," Front. Phys. **3**, 24 (2015).
14. N. V. Wheeler, Y. Chen, J. R. Hayes, T. D. Bradley, H. C. H. Mulvad, S. A. Mousavi, S. R. Sandoghchi, M. A. Gouveia, E. Numkam, G. T. Jasion, M. B. S. Nawazuddin, P. Horak, S. U. Alam, M. N. Petrovich, F. Poletti, and D. J. Richardson, "Novel hollow core fibers for ultra-high power delivery," in *2017 IEEE Photonics Conference (IPC)* (2017), pp. 279–280.
15. G. Palma-Vega, F. Beier, F. Stutzki, S. Fabian, T. Schreiber, R. Eberhardt, and A. Tünnermann, "High average power transmission through hollow-core fibers," in *Laser Congress 2018 (ASSL)* (Optical Society of America, 2018), p. ATh1A.7.
16. R.-J. Essiambre, G. J. Foschini, G. Kramer, and P. Winzer, "Capacity limits of transport in fiber-optic networks," Phys. Rev. Lett. **101**, 163901 (2008).
17. R.-J. Essiambre, G. Kramer, P. Winzer, G. J. Foschini, and B. Goebel, "Capacity limits of optical fiber networks," J. Lightwave Technol. **28**, 662–701 (2010).
18. F. Poletti, N. V. Wheeler, M. N. Petrovich, N. Baddela, E. Numkam Fokoua, J. R. Hayes, D. R. Gray, Z. Li, R. Slavik, and D. J. Richardson, "Towards high-capacity fibre-optic communications at the speed of light in vacuum," Nat. Photonics **7**, 279–284 (2013).
19. B. Zhu, B. J. Mangan, T. Kremp, G. S. Puc, V. Mikhailov, K. Dube, Y. Dulashko, M. Cortes, Y. Liang, K. Marceau, B. Violette, D. Cartsounis, R. Lago, B. Savran, D. Inniss, and D. J. DiGiovanni, "First demonstration of hollow-core-fiber cable for low latency data transmission," in *2020 Optical Fiber Communications Conference and Exhibition (OFC)* (2020), pp. 1–3.
20. M. Kuschnerov, B. J. Mangan, K. Gong, V. A. J. M. Sleiffer, M. Herrmann, J. W. Nicholson, J. M. Fini, L. Meng, R. S. Windeler, E. M. Monberg, A. DeSantolo, K. Mukasa, V. Mikhailov, U. Feiste, W. Zhang, and R. Yu, "Transmission of commercial low latency interfaces over hollow-core fiber," J. Lightwave Technol. **34**, 314–320 (2016).
21. Y. Hong, K. R. H. Bottrill, T. D. Bradley, H. Sakr, G. T. Jasion, K. Harrington, F. Poletti, P. Petropoulos, and D. J. Richardson, "Low-latency WDM intensity-modulation and direct-detection transmission over >100 km distances in a hollow core fiber," Laser Photonics Rev. **15**, 2100102 (2021).
22. X. Chen, W. Ding, Y.-Y. Wang, S.-F. Gao, F. Xu, H. Xu, Y.-F. Hong, Y.-Z. Sun, P. Wang, Y.-Q. Lu, and L. Zhang, "High-fidelity, low-latency polarization quantum state transmissions over a hollow-core conjoined-tube fiber at around 800 nm," Photonics Res. **9**, 460–470 (2021).
23. M. A. Iqbal, N. Parkin, and A. Lord, "Performance benefits analysis of low-loss hollow core fibre in UWB transmission systems," in *2021 Conference on Lasers and Electro-Optics (CLEO)* (2021), pp. 1–2.
24. A. Iqbal, P. Wright, N. Parkin, M. Fake, M. Alonso, S. R. Sandoghchi, and A. Lord, "First demonstration of 400ZR DWDM transmission through field deployable hollow-core-fibre cable," in *Optical Fiber Communication Conference (OFC) 2021* (Optica Publishing Group, 2021), p. 4C.2.
25. L. Schares, D. M. Kuchta, and A. F. Benner, "Optics in future data center networks," in *2010 18th IEEE Symposium on High Performance Interconnects* (2010), pp. 104–108.
26. B. J. Mangan, M. Kuschnerov, J. W. Nicholson, J. M. Fini, L. Meng, R. S. Windeler, E. M. Monberg, A. DeSantolo, K. Mukasa, V. Mikhailov, M. Herrmann, and U. Feiste, "First demonstration of hollow-core fiber for intra data

center low latency connectivity with a commercial 100Gb/s interface," in *Optical Fiber Communication Conference* (Optica Publishing Group, 2015), p. M3D.4.

27. X. Tian, R. Han, L. Wang, G. Lu, and J. Zhan, "Latency critical big data computing in finance," J. Finance Data Sci. **1**, 33–41 (2015).
28. R. Proietti, Z. Cao, C. J. Nitta, Y. Li, and S. J. B. Yoo, "A scalable, low-latency, high-throughput, optical interconnect architecture based on arrayed waveguide grating routers," J. Lightwave Technol. **33**, 911–920 (2015).
29. R. Slavík, G. Marra, E. Numkam Fokoua, N. Baddela, N. V. Wheeler, M. Petrovich, F. Poletti, and D. J. Richardson, "Ultralow thermal sensitivity of phase and propagation delay in hollow core optical fibres," Sci. Rep. **5**, 15447 (2015).
30. E. Numkam Fokoua, M. N. Petrovich, T. Bradley, F. Poletti, D. J. Richardson, and R. Slavík, "How to make the propagation time through an optical fiber fully insensitive to temperature variations," Optica **4**, 659–668 (2017).
31. V. Dangui, H. K. Kim, M. J. F. Digonnet, and G. S. Kino, "Phase sensitivity to temperature of the fundamental mode in air-guiding photonic-bandgap fibers," Opt. Express **13**, 6669–6684 (2005).
32. C. Lisdat, G. Grosche, and N. Quintin, *et al.*, "A clock network for geodesy and fundamental science," Nat. Commun. **7**, 12443 (2016).
33. G. A. Sanders, A. A. Taranta, C. Narayanan, E. Numkam Fokoua, S. A. Mousavi, L. K. Strandjord, M. Smiciklas, T. D. Bradley, J. Hayes, G. T. Jasion, T. Qiu, W. Williams, F. Poletti, and D. N. Payne, "Hollow-core resonator fiber optic gyroscope using nodeless anti-resonant fiber," Opt. Lett. **46**, 46–49 (2021).
34. F. Couny, F. Benabid, P. J. Roberts, P. S. Light, and M. G. Raymer, "Generation and photonic guidance of multi-octave optical-frequency combs," Science **318**, 1118–1121 (2007).
35. B. Debord, F. Amrani, L. Vincetti, F. Gérôme, and F. Benabid, "Hollow-core fiber technology: the rising of gas photonics," Fibers **7**, 16 (2019).
36. F. Benabid, G. Bouwmans, J. C. Knight, P. S. J. Russell, and F. Couny, "Ultrahigh efficiency laser wavelength conversion in a gas-filled hollow core photonic crystal fiber by pure stimulated rotational Raman scattering in molecular hydrogen," Phys. Rev. Lett. **93**, 123903 (2004).
37. M. Cassataro, D. Novoa, M. C. Günendi, N. N. Edavalath, M. H. Frosz, J. C. Travers, and P. S. Russell, "Generation of broadband mid-IR and UV light in gas-filled single-ring hollow-core PCF," Opt. Express **25**, 7637–7644 (2017).
38. T. Balciunas, C. Fourcade-Dutin, G. Fan, T. Witting, A. A. Voronin, A. M. Zheltikov, F. Gerome, G. G. Paulus, A. Baltuska, and F. Benabid, "A strong-field driver in the single-cycle regime based on self-compression in a Kagomé fibre," Nat. Commun. **6**, 6117 (2015).
39. F. Benabid, J. Knight, and P. Russell, "Particle levitation and guidance in hollow-core photonic crystal fiber," Opt. Express **10**, 1195–1203 (2002).
40. D. S. Bykov, O. A. Schmidt, T. G. Euser, and P. S. J. Russell, "Flying particle sensors in hollow-core photonic crystal fibre," Nat. Photonics **9**, 461–465 (2015).
41. D. S. Bykov, S. Xie, R. Zeltner, A. Machnev, G. K. L. Wong, T. G. Euser, and P. S. J. Russell, "Long-range optical trapping and binding of microparticles in hollow-core photonic crystal fibre," Light: Sci. Appl. **7**, 22 (2018).
42. Y. Tamura, H. Sakuma, K. Morita, M. Suzuki, Y. Yamamoto, K. Shimada, Y. Honma, K. Sohma, T. Fujii, and T. Hasegawa, "The first 0.14-dB/km loss optical fiber and its impact on submarine transmission," J. Lightwave Technol. **36**, 44–49 (2018).
43. M. Wandel, "Attenuation in silica-based optical fibers," Ph.D. thesis (DTU, 2006).
44. S. Sakaguchi and S. ichi Todoroki, "Rayleigh scattering of silica core optical fiber after heat treatment," Appl. Opt. **37**, 7708–7711 (1998).

45. G. T. Jasion, H. Sakr, J. R. Hayes, S. R. Sandoghchi, L. Hooper, E. N. Fokoua, A. Saljoghei, H. C. Mulvad, M. Alonso, A. Taranta, T. D. Bradley, I. A. Davidson, Y. Chen, D. J. Richardson, and F. Poletti, "0.174 dB/km hollow core double nested antiresonant nodeless fiber (DNANF)," in *2022 Optical Fiber Communications Conference and Exhibition (OFC)* (2022), pp. 1–3.
46. T. P. White, R. C. McPhedran, C. M. de Sterke, L. C. Botten, and M. J. Steel, "Confinement losses in microstructured optical fibers," Opt. Lett. **26**, 1660–1662 (2001).
47. K. Saitoh and M. Koshiba, "Leakage loss and group velocity dispersion in air-core photonic bandgap fibers," Opt. Express **11**, 3100 (2003).
48. P. J. Roberts, F. Couny, H. Sabert, B. J. Mangan, T. A. Birks, J. C. Knight, and P. S. J. Russell, "Loss in solid-core photonic crystal fibers due to interface roughness scattering," Opt. Express **13**, 7779 (2005).
49. P. J. Roberts, F. Couny, H. Sabert, B. J. Mangan, D. P. Williams, L. Farr, M. W. Mason, A. Tomlinson, T. A. Birks, J. C. Knight, and P. St. J. Russell, "Ultimate low loss of hollow-core photonic crystal fibres," Opt. Express **13**, 236 (2005).
50. B. Temelkuran, S. Hart, G. Benoit, J. Joannopoulos, and Y. Fink, "Wavelength-scalable hollow optical fibres with large photonic bandgaps for CO_2 laser transmission," Nature **420**, 650–653 (2002).
51. F. Benabid, J. C. Knight, G. Antonopoulos, and P. S. J. Russell, "Stimulated Raman scattering in hydrogen-filled hollow-core photonic crystal fiber," Science **298**, 399–402 (2002).
52. F. Poletti, "Nested antiresonant nodeless hollow core fiber," Opt. Express **22**, 23807–23828 (2014).
53. P. Yeh, A. Yariv, and E. Marom, "Theory of Bragg fiber," J. Opt. Soc. Am. **68**, 1196–1201 (1978).
54. S. Johnson, M. Ibanescu, M. Skorobogatiy, O. Weisberg, T. Engeness, M. Soljacic, S. Jacobs, J. Joannopoulos, and Y. Fink, "Low-loss asymptotically single-mode propagation in large-core OmniGuide fibers," Opt. Express **9**, 748 (2001).
55. C. M. Smith, N. Venkataraman, M. T. Gallagher, D. Muller, J. A. West, N. F. Borrelli, D. C. Allan, and K. W. Koch, "Low-loss hollow-core silica/air photonic bandgap fibre," Nature **424**, 657–659 (2003).
56. B. Mangan, L. Farr, A. Langford, P. Roberts, D. Williams, F. Couny, M. Lawman, M. Mason, S. Coupland, R. Flea, H. Sabert, T. Birks, J. Knight, and P. Russell, "Low loss (1.7 dB/km) hollow core photonic bandgap fiber," in *Optical Fiber Communication Conference (OFC) 2004*, Vol. 2 (2004), p. PDP 24.
57. R. Amezcua-Correa, F. Gérôme, S. G. Leon-Saval, N. G. R. Broderick, T. A. Birks, and J. C. Knight, "Control of surface modes in low loss hollow-core photonic bandgap fibers," Opt. Express **16**, 1142–1149 (2008).
58. M. N. Petrovich, F. Poletti, A. van Brakel, and D. J. Richardson, "Robustly single mode hollow core photonic bandgap fiber," Opt. Express **16**, 4337–4346 (2008).
59. X. Chen, M.-J. Li, N. Venkataraman, M. T. Gallagher, W. A. Wood, A. M. Crowley, J. P. Carberry, L. A. Zenteno, and K. W. Koch, "Highly birefringent hollow-core photonic bandgap fiber," Opt. Express **12**, 3888–3893 (2004).
60. N. K. Baddela, M. N. Petrovich, Y. Jung, J. R. Hayes, N. V. Wheeler, D. R. Gray, N. Wong, F. Parmigiani, E. Numkam, J. P. Wooler, F. Poletti, and D. J. Richardson, "First demonstration of a low loss 37-cell hollow core photonic bandgap fiber and its use for data transmission," in *CLEO: 2013* (Optical Society of America, 2013), p. CTu2K.3.
61. Y. Jung, V. A. J. M. Sleiffer, N. Baddela, M. N. Petrovich, J. R. Hayes, N. V. Wheeler, D. R. Gray, E. N. Fokoua, J. P. Wooler, N. H.-L. Wong, F. Parmigiani, S. U. Alam, J. Surof, M. Kuschnerov, V. Veljanovski, H. de Waardt, F. Poletti, and D.

J. Richardson, “First demonstration of a broadband 37-cell hollow core photonic bandgap fiber and its application to high capacity mode division multiplexing,” in *Optical Fiber Communication Conference/National Fiber Optic Engineers Conference 2013* (Optical Society of America, 2013), p. PDP5A.3.

62. V. A. J. M. Sleiffer, Y. Jung, N. K. Baddela, J. Surof, M. Kuschnerov, V. Veljanovski, J. R. Hayes, N. V. Wheeler, E. R. N. Fokoua, J. P. Wooler, D. R. Gray, N. H.-L. Wong, F. R. Parmigiani, S.-u. Alam, M. N. Petrovich, F. Poletti, D. J. Richardson, and H. de Waardt, “High capacity mode-division multiplexed optical transmission in a novel 37-cell hollow-core photonic bandgap fiber,” J. Lightwave Technol. **32**, 854–863 (2014).
63. J. M. Fini, J. W. Nicholson, B. Mangan, L. Meng, R. S. Windeler, E. M. Monberg, A. DeSantolo, F. V. DiMarcello, and K. Mukasa, “Polarization maintaining single-mode low-loss hollow-core fibres,” Nat. Commun. **5**, 5085 (2014).
64. N. V. Wheeler, A. M. Heidt, N. K. Baddela, E. Numkam Fokoua, J. R. Hayes, S. R. Sandoghchi, F. Poletti, M. N. Petrovich, and D. J. Richardson, “Low-loss and low-bend-sensitivity mid-infrared guidance in a hollow-core photonic bandgap fiber,” Opt. Lett. **39**, 295–298 (2014).
65. NKT Photonics, “Hollow core photonic crystal fibers,” https://www.nktphotonics.com/products/optical-fibers-and-modules/hollow-core-photonic-crystal-fibers/. [Online; accessed 30 March 2022.]
66. X. Xu, X. Yuan, F. Gao, X. Wang, and N. Song, “Investigation of longitudinal uniformity of the core structure in a hollow-core photonic bandgap fiber,” Opt. Express **29**, 37534–37540 (2021).
67. F. Couny, F. Benabid, P. J. Roberts, M. T. Burnett, and S. Maier, “Identification of bloch-modes in hollow-core photonic crystal fiber cladding,” Opt. Express **15**, 325–338 (2007).
68. F. Poletti and E. Numkam Fokoua, “Understanding the physical origin of surface modes and practical rules for their suppression,” in *39th European Conference and Exhibition on Optical Communication (ECOC 2013)* (2013), pp. 1–3.
69. D. C. Allan, N. F. Borrelli, M. T. Gallagher, D. Müller, C. M. Smith, N. Venkataraman, J. A. West, P. Zhang, and K. W. Koch, “Surface modes and loss in air-core photonic bandgap fibers,” Proc. SPIE **5000**, 161 (2003).
70. J. A. West, C. M. Smith, N. F. Borrelli, D. C. Allan, and K. W. Koch, “Surface modes in air-core photonic band-gap fibers,” Opt. Express **12**, 1485–1496 (2004).
71. P. J. Roberts, D. P. Williams, B. J. Mangan, H. Sabert, F. Couny, W. J. Wadsworth, T. A. Birks, J. C. Knight, and P. S. J. Russell, “Realizing low loss air core photonic crystal fibers by exploiting an antiresonant core surround,” Opt. Express **13**, 8277 (2005).
72. T. A. Birks, P. J. Roberts, F. Couny, H. Sabert, B. J. Mangan, D. P. Williams, L. Farr, M. W. Mason, A. Tomlinson, J. C. Knight, and P. S. J. Russell, “The fundamental limits to the attenuation of hollow-core photonic crystal fibres,” in *Proceedings of 2005 7th International Conference on Transparent Optical Networks, ICTON 2005* Vol. 1 (2005), pp. 107–110.
73. J. Jackle and K. Kawasaki, “Intrinsic roughness of glass surfaces,” J. Phys.: Condens. Matter **7**, 4351–4358 (1995).
74. F. Poletti, N. G. R. Broderick, D. J. Richardson, and T. M. Monro, “The effect of core asymmetries on the polarization properties of hollow core photonic bandgap fibers,” Opt. Express **13**, 9115–9124 (2005).
75. R. Amezcua-Correa, N. G. R. Broderick, M. N. Petrovich, F. Poletti, D. J. Richardson, V. Finazzi, and T. M. Monro, “Realistic designs of silica hollow-core photonic bandgap fibers free of surface modes,” in *Optical Fiber Communication Conference and Exposition and The National Fiber Optic Engineers Conference* (Optica Publishing Group, 2006), p. OFC1.

76. R. Amezcua-Correa, N. G. R. Broderick, M. N. Petrovich, F. Poletti, and D. J. Richardson, "Optimizing the usable bandwidth and loss through core design in realistic hollow-core photonic bandgap fibers," Opt. Express **14**, 7974–7985 (2006).
77. R. Amezcua-Correa, N. G. R. Broderick, M. N. Petrovich, F. Poletti, and D. J. Richardson, "Design of 7 and 19 cells core air-guiding photonic crystal fibers for low-loss, wide bandwidth and dispersion controlled operation," Opt. Express **15**, 17577–17586 (2007).
78. N. V. Wheeler, M. N. Petrovich, R. Slavík, N. Baddela, E. Numkam, J. R. Hayes, D. R. Gray, F. Poletti, and D. J. Richardson, "Wide-bandwidth, low-loss, 19-cell hollow core photonic band gap fiber and its potential for low latency data transmission," in *National Fiber Optic Engineers Conference* (Optical Society of America, 2012), p. PDP5A.2.
79. X. Zhang, S. Gao, Y. Wang, W. Ding, X. Wang, and P. Wang, "7-cell hollow-core photonic bandgap fiber with broad spectral bandwidth and low loss," Opt. Express **27**, 11608–11616 (2019).
80. M. H. Frosz, J. Nold, T. Weiss, A. Stefani, F. Babic, S. Rammler, and P. S. J. Russell, "Five-ring hollow-core photonic crystal fiber with 1.8 dB/km loss," Opt. Lett. **38**, 2215–2217 (2013).
81. Y. Chen, Z. Liu, S. R. Sandoghchi, G. T. Jasion, T. D. Bradley, E. Numkam Fokoua, J. R. Hayes, N. V. Wheeler, D. R. Gray, B. J. Mangan, R. Slavík, F. Poletti, M. N. Petrovich, and D. J. Richardson, "Multi-kilometer long, longitudinally uniform hollow core photonic bandgap fibers for broadband low latency data transmission," J. Lightwave Technol. **34**, 104–113 (2016).
82. G. T. Jasion, J. S. Shrimpton, Y. Chen, T. Bradley, D. J. Richardson, and F. Poletti, "Microstructure element method (MSEM): viscous flow model for the virtual draw of microstructured optical fibers," Opt. Express **23**, 312–329 (2015).
83. G. T. Jasion, E. N. Fokoua, J. S. Shrimpton, D. J. Richardson, and F. Poletti, "Studying the limits of production rate and yield for the volume manufacturing of hollow core photonic band gap fibers," Opt. Express **23**, 32179–32190 (2015).
84. S. Février, B. Beaudou, and P. Viale, "Understanding origin of loss in large pitch hollow-core photonic crystal fibers and their design simplification," Opt. Express **18**, 5142–5150 (2010).
85. F. Gérôme, R. Jamier, J.-L. Auguste, G. Humbert, and J.-M. Blondy, "Simplified hollow-core photonic crystal fiber," Opt. Lett. **35**, 1157–1159 (2010).
86. F. Yu, W. J. Wadsworth, and J. C. Knight, "Low loss silica hollow core fibers for 3–4 μm spectral region," Opt. Express **20**, 11153–11158 (2012).
87. J. R. Hayes, F. Poletti, M. S. Abokhamis, N. V. Wheeler, N. K. Baddela, and D. J. Richardson, "Anti-resonant hexagram hollow core fibers," Opt. Express **23**, 1289 (2015).
88. Y. Y. Wang, N. V. Wheeler, F. Couny, P. J. Roberts, and F. Benabid, "Low loss broadband transmission in hypocycloid-core Kagomé hollow-core photonic crystal fiber," Opt. Lett. **36**, 669 (2011).
89. A. D. Pryamikov, A. S. Biriukov, A. F. Kosolapov, V. G. Plotnichenko, S. L. Semjonov, and E. M. Dianov, "Demonstration of a waveguide regime for a silica hollow - core microstructured optical fiber with a negative curvature of the core boundary in the spectral region > 3.5 μm," Opt. Express **19**, 1441–1448 (2011).
90. A. N. Kolyadin, A. F. Kosolapov, A. D. Pryamikov, A. S. Biriukov, V. G. Plotnichenko, and E. M. Dianov, "Light transmission in negative curvature hollow core fiber in extremely high material loss region," Opt. Express **21**, 9514 (2013).
91. P. Uebel, M. C. Günendi, M. H. Frosz, G. Ahmed, N. N. Edavalath, J.-M. Ménard, and P. S. Russell, "Broadband robustly single-mode hollow-core PCF by resonant filtering of higher-order modes," Opt. Lett. **41**, 1961 (2016).

92. M. B. S. Nawazuddin, N. V. Wheeler, J. R. Hayes, S. R. Sandoghchi, T. D. Bradley, G. T. Jasion, R. Slavík, D. J. Richardson, and F. Poletti, "Lotus-shaped negative curvature hollow core fiber with 10.5 dB/km at 1550 nm wavelength," J. Lightwave Technol. **36**, 1213–1219 (2018).
93. J. R. Hayes, S. R. Sandoghchi, T. D. Bradley, Z. Liu, R. Slavík, M. A. Gouveia, N. V. Wheeler, G. Jasion, Y. Chen, E. N. Fokoua, M. N. Petrovich, D. J. Richardson, and F. Poletti, "Antiresonant hollow core fiber with an octave spanning bandwidth for short haul data communications," J. Lightwave Technol. **35**, 437–442 (2017).
94. S. Gao, "Hollow-core conjoined-tube negative-curvature fibre with ultralow loss," Nat. Commun. **9**, 2828 (2018).
95. A. F. Kosolapov, G. K. Alagashev, A. N. Kolyadin, A. D. Pryamikov, A. S. Biryukov, I. A. Bufetov, and E. M. Dianov, "Hollow-core revolver fibre with a double-capillary reflective cladding," Quantum Electron. **46**, 267–270 (2016).
96. T. D. Bradley, G. T. Jasion, J. R. Hayes, Y. Chen, L. Hooper, H. Sakr, M. Alonso, A. Taranta, A. Saljoghei, H. C. Mulvad, M. Fake, I. A. K. Davidson, N. V. Wheeler, E. Numkam Fokoua, W. Wang, S. R. Sandoghchi, D. J. Richardson, and F. Poletti, "Antiresonant hollow core fibre with 0.65 dB/km attenuation across the C and L telecommunication bands," in *45th European Conference on Optical Communication (ECOC 2019)* (2019), pp. 1–4.
97. F. Amrani, J. H. Osorio, F. Delahaye, F. Giovanardi, L. Vincetti, B. Debord, F. Gerome, and F. Benabid, "Low-loss single-mode hybrid-lattice hollow-core photonic-crystal fibre," Light: Sci. Appl. **10**, 7 (2021).
98. H. Sakr, T. D. Bradley, G. T. Jasion, E. N. Fokoua, S. R. Sandoghchi, I. A. Davidson, A. Taranta, G. Guerra, W. Shere, Y. Chen, J. R. Hayes, D. J. Richardson, and F. Poletti, "Hollow core nanfs with five nested tubes and record low loss at 850, 1060, 1300 and 1625nm," in *2021 Optical Fiber Communications Conference and Exhibition (OFC)* (2021), pp. 1–3.
99. F. Couny, F. Benabid, and P. S. Light, "Large-pitch Kagomé-structured hollow-core photonic crystal fiber," Opt. Lett. **31**, 3574–3576 (2006).
100. F. Poletti, J. R. Hayes, and D. J. Richardson," Optimising the performances of hollow antiresonant fibres," in *2011 37th European Conference and Exhibition on Optical Communication* (2011), pp. 1–3.
101. Y. Y. Wang, F. Couny, P. J. Roberts, and F. Benabid, "Low loss broadband transmission in optimized core-shape Kagomé hollow-core PCF," in *Conference on Lasers and Electro-Optics 2010* (Optical Society of America, 2010), p. CPDB4.
102. W. Ding and Y. Wang, "Analytic model for light guidance in single-wall hollow-core anti-resonant fibers," Opt. Express **22**, 27242–27256 (2014).
103. W. Ding and Y. Wang, "Semi-analytical model for hollow-core anti-resonant fibers," Front. Phys. **3**, 16 (2015).
104. Y. Wang and W. Ding, "Confinement loss in hollow-core negative curvature fiber: A multi-layered model," Opt. Express **25**, 33122 (2017).
105. C. Wei, R. Joseph Weiblen, C. R. Menyuk, and J. Hu, "Negative curvature fibers," Adv. Opt. Photonics **9**, 562 (2017).
106. F. Yu and J. C. Knight, "Negative curvature hollow-core optical fiber," IEEE J. Sel. Top. Quantum Electron. **22**, 146–155 (2016).
107. W. Ding, Y. Y. Wang, S. F. Gao, M. L. Wang, and P. Wang, "Recent progress in low-loss hollow-core anti-resonant fibers and their applications," IEEE J. Sel. Top. Quantum Electron. **26**, 1–12 (2020).
108. F. Yu, M. Cann, A. Brunton, W. Wadsworth, and J. Knight, "Single-mode solarization-free hollow-core fiber for ultraviolet pulse delivery," Opt. Express **26**, 10879–10887 (2018).
109. J. H. Osório, F. Amrani, F. Delahaye, A. Dhaybi, K. Vasko, G. Tessier, F. Giovanardi, L. Vincetti, B. Debord, F. Gérôme, and F. Benabid, "Hollow-core fibers

with ultralow loss in the ultraviolet range and sub-thermodynamic equilibrium surface-roughness," in 2022 Conference on Lasers and Electro-Optics (CLEO) (IEEE 2021).

110. X. Zhang, W. Song, Z. Dong, J. Yao, S. Wan, Y. Hou, and P. Wang, "Low loss nested hollow-core anti-resonant fiber at 2 μm spectral range," Opt. Lett. **47**, 589–592 (2022).
111. N. V. Wheeler, T. D. Bradley, J. R. Hayes, M. A. Gouveia, S. Liang, Y. Chen, S. R. Sandoghchi, S. M. A. Mousavi, F. Poletti, M. N. Petrovich, and D. J. Richardson, "Low-loss Kagomé hollow-core fibers operating from the near- to the mid-IR," Opt. Lett. **42**, 2571–2574 (2017).
112. F. Yu, P. Song, D. Wu, T. Birks, D. Bird, and J. Knight, "Attenuation limit of silica-based hollow-core fiber at mid-IR wavelengths," APL Photonics **4**, 080803 (2019).
113. I. A. Davidson, S. Rikimi, H. Sakr, G. T. Jasion, T. D. Bradley, N. V. Wheeler, F. Poletti, and D. J. Richardson, "Anti-resonant, mid-infrared silica hollow-core fiber," in *OSA Advanced Photonics Congress (AP) 2020 (IPR, NP, NOMA, Networks, PVLED, PSC, SPPCom, SOF)* (Optical Society of America, 2020), p. SoW1H.7.
114. W. Belardi and J. C. Knight, "Hollow antiresonant fibers with reduced attenuation," Opt. Lett. **39**, 1853 (2014).
115. G. T. Jasion, T. D. Bradley, K. Harrington, H. Sakr, Y. Chen, E. Numkam Fokoua, I. A. Davidson, A. Taranta, J. R. Hayes, D. J. Richardson, and F. Poletti, "Hollow core NANF with 0.28 dB/km attenuation in the C and L bands," in *2020 Optical Fiber Communications Conference and Exhibition (OFC)* (2020), pp. 1–3.
116. S. Gao, Y. Wang, W. Ding, Y. Hong, and P. Wang, "Conquering the Rayleigh scattering limit of silica glass fiber at visible wavelengths with a hollow-core fiber approach," Laser Photonics Rev. **14**, 1900241 (2020).
117. H. Sakr, Y. Chen, G. T. Jasion, T. D. Bradley, J. R. Hayes, H. C. H. Mulvad, I. A. Davidson, E. Numkam Fokoua, and F. Poletti, "Hollow core optical fibres with comparable attenuation to silica fibres between 600 and 1100 nm," Nat. Commun. **11**, 6030 (2020).
118. A. W. Snyder, "Leaky-ray theory of optical waveguides of circular cross section," Appl. Phys. **4**, 273–298 (1974).
119. A. W. Snyder and J. D. Love, *Optical Waveguide Theory* (Chapman and Hall, 1983).
120. J. Pomplun, L. Zschiedrich, R. Klose, F. Schmidt, and S. Burger, "Finite element simulation of radiation losses in photonic crystal fibers," Phys. Status Solidi A **204**, 3822–3837 (2007).
121. E. A. Marcatili and R. A. Schmeltzer, "Hollow metallic and dielectric waveguides for long distance optical transmission and lasers," Bell Syst. Tech. J. **43**, 1783–1809 (1964).
122. M. Zeisberger and M. A. Schmidt, "Analytic model for the complex effective index of the leaky modes of tube-type anti-resonant hollow core fibers," Sci. Rep. **7**, 11761–13 (2017).
123. D. Bird, "Attenuation of model hollow-core, anti-resonant fibres," Opt. Express **25**, 23215 (2017).
124. G. Li, R. F. Ando, M. Zeisberger, T. Weiss, and M. A. Schmidt, "Interpreting light guidance in antiresonant and photonic bandgap waveguides and fibers by light scattering: analytical model and ultra-low guidance," Opt. Express **30**, 2768–2779 (2022).
125. T. Grujic, B. T. Kuhlmey, A. Argyros, S. Coen, and C. M. de Sterke, "Solid-core fiber with ultra-wide bandwidth transmission window due to inhibited coupling," Opt. Express **18**, 25556–25566 (2010).

126. C. W. Hsu, B. Zhen, A. D. Stone, J. D. Joannopoulos, and M. Soljacic, "Bound states in the continuum," Nat. Rev. Mater. **1**, 16048 (2016).
127. B. Debord, A. Amsanpally, M. Chafer, A. Baz, M. Maurel, J. M. Blondy, E. Hugonnot, F. Scol, L. Vincetti, F. Gérôme, and F. Benabid, "Ultralow transmission loss in inhibited-coupling guiding hollow fibers," Optica **4**, 209 (2017).
128. J. M. Fini, "Suppression of higher-order modes in aircore microstructure fiber designs," in *Conference on Lasers and Electro-Optics/Quantum Electronics and Laser Science Conference and Photonic Applications Systems Technologies* (Optical Society of America, 2006), p. CMM4.
129. K. Saitoh, N. J. Florous, T. Murao, and M. Koshiba, "Design of photonic band gap fibers with suppressed higher-order modes: towards the development of effectively single mode large hollow-core fiber platforms," Opt. Express **14**, 7342–7352 (2006).
130. J. M. Fini, "Aircore microstructure fibers with suppressed higher-order modes," Opt. Express **14**, 11354–11361 (2006).
131. J. M. Fini, J. W. Nicholson, R. S. Windeler, E. M. Monberg, L. Meng, B. Mangan, A. DeSantolo, and F. V. DiMarcello, "Low-loss hollow-core fibers with improved single-modedness," Opt. Express **21**, 6233–6242 (2013).
132. B. Debord, M. Alharbi, T. Bradley, C. Fourcade-Dutin, Y. Wang, L. Vincetti, F. Gérôme, and F. Benabid, "Hypocycloid-shaped hollow-core photonic crystal fiber Part I: arc curvature effect on confinement loss," Opt. Express **21**, 28597–28608 (2013).
133. M. Alharbi, T. Bradley, B. Debord, C. Fourcade-Dutin, D. Ghosh, L. Vincetti, F. Gerome, and F. Benabid, "Hypocycloid-shaped hollow-core photonic crystal fiber Part II: Cladding effect on confinement and bend loss," Opt. Express **21**, 28609–28616 (2013).
134. W. Belardi and J. C. Knight, "Effect of core boundary curvature on the confinement losses of hollow antiresonant fibers," Opt. Express **21**, 21912 (2013).
135. E. Numkam Fokoua, D. J. Richardson, and F. Poletti, "Impact of structural distortions on the performance of hollow-core photonic bandgap fibers," Opt. Express **22**, 2735–2744 (2014).
136. C. Wei, C. R. Menyuk, and J. Hu, "Impact of cladding tubes in chalcogenide negative curvature fibers," IEEE Photonics J. **8**, 1–9 (2016).
137. L. Provino, "Effect of nested elements on avoided crossing between the higher-order core modes and the air-capillary modes in hollow-core antiresonant optical fibers," Fibers **6**, 42 (2018).
138. M. S. Habib, O. Bang, and M. Bache, "Low-loss hollow-core silica fibers with adjacent nested anti-resonant tubes," Opt. Express **23**, 17394–17406 (2015).
139. K. Saitoh, N. A. Mortensen, and M. Koshiba, "Air-core photonic band-gap fibers: the impact of surface modes," Opt. Express **12**, 394–400 (2004).
140. H. K. Kim, M. J. F. Digonnet, G. S. Kino, J. Shin, and S. Fan, "Simulations of the effect of the core ring on surface and air-core modes in photonic bandgap fibers," Opt. Express **12**, 3436–3442 (2004).
141. L. Vincetti and V. Setti, "Confinement loss in Kagomé and tube lattice fibers: Comparison and analysis," J. Lightwave Technol. **30**, 1470–1474 (2012).
142. L. Vincetti and V. Setti, "Waveguiding mechanism in tube lattice fibers," Opt. Express **18**, 23133–23146 (2010).
143. R. F. Ando, A. Hartung, B. Jang, and M. A. Schmidt, "Approximate model for analyzing band structures of single-ring hollow-core anti-resonant fibers," Opt. Express **27**, 10009 (2019).
144. L. Vincetti, "Empirical formulas for calculating loss in hollow core tube lattice fibers," Opt. Express **24**, 10313 (2016).

145. L. Vincetti and L. Rosa, "A simple analytical model for confinement loss estimation in hollow-core tube lattice fibers," Opt. Express **27**, 5230 (2019).
146. A. D. Pryamikov and G. Alagashev, "Features of light leakage from the negative curvature hollow core fibers," Opt. Eng. **57**, 1–7 (2018).
147. G. T. Jasion, D. J. Richardson, and F. Poletti, "Novel antiresonant hollow core fiber design with ultralow leakage loss using transverse power flow analysis," in *Optical Fiber Communication Conference (OFC) 2019* (Optical Society of America, 2019), p. Th3E.2.
148. A. Pryamikov, G. Alagashev, G. Falkovich, and S. Turitsyn, "Light transport and vortex-supported wave-guiding in micro-structured optical fibres," Sci. Rep. **10**, 2507 (2020).
149. T. A. Birks, D. M. Bird, T. D. Hedley, J. M. Pottage, and P. S. Russell, "Scaling laws and vector effects in bandgap-guiding fibres," Opt. Express **12**, 69–74 (2004).
150. F. Urbach, "The long-wavelength edge of photographic sensitivity and of the electronic absorption of solids," Phys. Rev. **92**, 1324 (1953).
151. J. D. Dow, "Urbach's rule," in *Optical Properties of Highly Transparent Solids*, S. S. Mitra and B. Bendow, eds. (Springer US, Boston, MA, 1975), pp. 131–143.
152. M. Lines, "Can the minimum attenuation of fused silica be significantly reduced by small compositional variations? I. Alkali metal dopants," J. Non-Cryst. Solids **171**, 209–218 (1994).
153. O. Humbach, H. Fabian, U. Grzesik, U. Haken, and W. Heitmann, "Analysis of OH absorption bands in synthetic silica," J. Non-Cryst. Solids **203**, 19–26 (1996).
154. M. Bredol, D. Leers, L. Bosselaar, and M. Hutjens, "Improved model for OH absorption in optical fibers," J. Lightwave Technol. **8**, 1536–1540 (1990).
155. N. Frateschi and A. De Castro, "Perturbation theory for the wave equation and the Effective refractive index approach," IEEE J. Quantum Electron. **22**, 12–15 (1986).
156. K. Zhang and D. Li, *Electromagnetic Theory for Microwaves and Optoelectronics* (Springer, 2008).
157. A. Villeneuve, "Orthogonality relationships for waveguides and cavities with inhomogeneous anisotropic media," IEEE Trans. Microwave Theory Tech. **7**, 441–446 (1959).
158. P. McIsaac, "Mode orthogonality in reciprocal and nonreciprocal waveguides," IEEE Trans. Microwave Theory Tech. **39**, 1808–1816 (1991).
159. B. Z. Katsenelenbaum, L. Mercader del Rio, M. Pereyaslavets, M. Sorolla Ayzaand, and M. Thumm, *Theory of Nonuniform Waveguides: the Cross-Section Method*, Electromagnetic Waves (Institution of Engineering and Technology, 1998).
160. D. Wu, F. Yu, and M. Liao, "Understanding the material loss of anti-resonant hollow-core fibers," Opt. Express **28**, 11840–11851 (2020).
161. E. Numkam Fokoua, V. Michaud-Belleau, J. Genest, R. Slavík, and F. Poletti, "Theoretical analysis of backscattering in hollow-core antiresonant fibers," APL Photonics **6**, 096106 (2021).
162. Heraeus, "Transmission calculator for optical applications," https://www.heraeus.com/en/hca/fused_silica_quartz_knowledge_base_1/t_calc_1/transmission_calc_opt/tr [Online; accessed 30 March 2022.]
163. N. V. Wheeler, M. N. Petrovich, N. K. Baddela, J. R. Hayes, E. N. Fokoua, F. Poletti, and D. J. Richardson, "Gas absorption between 1.8 and 2.1 μm in low loss (5.2 dB/km) HC-PBGF," in *2012 Conference on Lasers and Electro-Optics (CLEO)* (2012), pp. 1–2.

164. J. K. Lyngsø, B. J. Mangan, C. Jakobsen, and P. J. Roberts, “7-cell core hollow-core photonic crystal fibers with low loss in the spectral region around 2 μm,” Opt. Express **17**, 23468–23473 (2009).
165. S. Rikimi, Y. Chen, M. C. Partridge, T. D. Bradley, I. A. K. Davidson, A. A. Taranta, F. Poletti, M. N. Petrovich, D. J. Richardson, and N. V. Wheeler, “Growth of ammonium chloride on cleaved end-facets of hollow core fibers,” in *2020 Conference on Lasers and Electro-Optics (CLEO)* (2020), pp. 1–2.
166. S. Rikimi, Y. Chen, M. C. Partridge, I. A. Davidson, G. T. Jasion, T. D. Bradley, A. A. Taranta, F. Poletti, M. N. Petrovich, D. J. Richardson, and N. V. Wheeler, “Pressure in as-drawn hollow core fibers,” in *OSA Advanced Photonics Congress (AP) 2020 (IPR, NP, NOMA, Networks, PVLED, PSC, SPPCom, SOF)* (Optica Publishing Group, 2020), p. SoW1H.4.
167. S. Rikimi, Y. Chen, T. W. Kelly, I. Davidson, G. Jasion, M. Partridge, K. Harrington, T. Bradley, A. Taranta, F. Poletti, M. Petrovich, D. J. Richardson, and N. V. Wheeler, “Internal gas composition and pressure in as-drawn hollow core optical fibers,” J. Lightwave Technol. **40**, 4776–4785 (2022).
168. I. Gris-Sanchez and J. C. Knight, “Time-dependent degradation of photonic crystal fiber attenuation around OH absorption wavelengths,” J. Lightwave Technol. **30**, 3597–3602 (2012).
169. A. Bucholtz, “Rayleigh-scattering calculations for the terrestrial atmosphere,” Appl. Opt. **34**, 2765 (1995).
170. D. Marcuse, “Radiation losses of the HE11 mode of a fiber with sinusoidally perturbed core boundary,” Appl. Opt. **14**, 3021–3025 (1975).
171. D. Marcuse, *Theory of Dielectric Optical Waveguides*, 2nd ed. (Academic Press, 1991).
172. S. G. Johnson, M. Ibanescu, M. A. Skorobogatiy, O. Weisberg, J. D. Joannopoulos, and Y. Fink, “Perturbation theory for Maxwell’s equations with shifting material boundaries,” Phys. Rev. E **65**, 066611 (2002).
173. A. Yariv, “Coupled-mode theory for guided-wave optics,” IEEE J. Quantum Electron. **9**, 919–933 (1973).
174. M. Skorobogatiy, S. Jacobs, S. Johnson, and Y. Fink, “Geometric variations in high index-contrast waveguides, coupled mode theory in curvilinear coordinates,” Opt. Express **10**, 1227 (2002).
175. W.-P. Huang and J. Mu, “Complex coupled-mode theory for optical waveguides,” Opt. Express **17**, 19134–19152 (2009).
176. W. Chen, Z. Xiong, J. Xu, and Y. Chen, “Generalized coupled-mode formalism in reciprocal waveguides with gain, loss, anisotropy, or bianisotropy,” Phys. Rev. B **99**, 195307 (2019).
177. H. Haus, W. Huang, S. Kawakami, and N. Whitaker, “Coupled-mode theory of optical waveguides,” J. Lightwave Technol. **5**, 16–23 (1987).
178. D. Marcuse, “Coupled-mode theory for anisotropic optical waveguides,” The Bell Syst. Tech. J. **54**, 985–995 (1975).
179. W.-P. Huang, “Coupled-mode theory for optical waveguides: an overview,” J. Opt. Soc. Am. A **11**, 963–983 (1994).
180. E. Numkam Fokoua, F. Poletti, and D. J. Richardson, “Analysis of light scattering from surface roughness in hollow-core photonic bandgap fibers,” in *European Conference on Optical Communication* (Optica Publishing Group, 2012), p. Mo.2.F.3.
181. A. W. Snyder, “Radiation losses due to variations of radius on dielectric or optical fibers,” IEEE Trans. Microwave Theory Tech. **18**, 608–615 (1970).
182. I. A. White, “Radiation from bends in optical-waveguides - volume-current method,” IEE J. Microwaves, Opt. Acoust. **3**, 186–188 (1979).

183. M. Kuznetsov and H. A. Haus, "Radiation loss in dielectric waveguide structures by the volume current method," IEEE J. Quantum Electron. **19**, 1505–1514 (1983).
184. J. P. R. Lacey and F. P. Payne, "Radiation loss from planar waveguides with random wall imperfections," IEE Proc.-J: Optoelectron. **137**, 282–288 (1990).
185. S. G. Johnson, M. L. Povinelli, M. Soljačić, A. Karalis, S. Jacobs, and J. D. Joannopoulos, "Roughness losses and volume-current methods in photonic-crystal waveguides," Appl. Phys. B: Lasers Opt. **81**, 283–293 (2005).
186. C. H. Papas, *Theory of Electromagnetic Wave Propagation* (Dover Publications, Inc., New York, 1988).
187. T. Sarlat, A. Lelarge, E. Søndergård, and D. Vandembroucq, "Frozen capillary waves on glass surfaces: an AFM study," Eur. Phys. J. B **54**, 121–126 (2006).
188. M. C. Phan-Huy, J. M. Moison, J. A. Levenson, S. Richard, G. Mélin, M. Douay, and Y. Quiquempois, "Surface roughness and light scattering in a small effective area microstructured fiber," J. Lightwave Technol. **27**, 1597–1604 (2009).
189. C. Brun, X. Buet, B. Bresson, M. S. Capelle, M. Ciccotti, A. Ghomari, P. Lecomte, J. P. Roger, M. N. Petrovich, F. Poletti, D. J. Richardson, D. Vandembroucq, and G. Tessier, "Picometer-scale surface roughness measurements inside hollow glass fibres," Opt. Express **22**, 29554–29567 (2014).
190. X. Buet, C. Brun, B. Bresson, M. Ciccotti, M. N. Petrovich, F. Poletti, D. J. Richardson, D. Vandembroucq, and G. Tessier, "Picometer-scale surface roughness measurements inside hollow glass fibres," *Conference on Lasers and Electro-Optics Europe - Technical Digest*, Vol. 2015 (2015), pp. 4351–4358.
191. X. Buet, C. Brun, J. Gâteau, B. Bresson, S. R. Sandoghchi, E. N. Fokoua, M. Petrovich, F. Poletti, D. Richardson, D. Vandembroucq, and G. Tessier, "Nondestructive measurement of the roughness of the inner surface of hollow core-photonic bandgap fibers," Opt. Lett. **41**, 5086 (2016).
192. B. Bresson, C. Brun, X. Buet, Y. Chen, M. Ciccotti, J. Gâteau, G. Jasion, M. N. Petrovich, F. Poletti, D. J. Richardson, S. R. Sandoghchi, G. Tessier, B. Tyukodi, and D. Vandembroucq, "Anisotropic superattenuation of capillary waves on driven glass interfaces," Phys. Rev. Lett. **119**, 235501 (2017).
193. V. Dangui, M. J. Digonnet, and G. S. Kino, "Modeling of the propagation loss and backscattering in air-core photonic-bandgap fibers," J. Lightwave Technol. **27**, 3783–3789 (2009).
194. E. Numkam Fokoua, N. Wong, D. J. Richardson, and F. Poletti, "Analysis and comparison of intermodal coupling coefficient of standard and hollow core few moded fibres," in *2015 European Conference on Optical Communication (ECOC)* (2015), pp. 1–3.
195. E. Numkam Fokoua, Y. Chen, D. J. Richardson, and F. Poletti, "Microbending effects in hollow-core photonic bandgap fibers," in *ECOC 2016: 42nd European Conference on Optical Communication* (2016), pp. 1–3.
196. Y. Chen, N. V. Wheeler, N. K. Baddela, J. R. Hayes, S. R. Sandoghchi, E. N. Fokoua, M. Li, F. Poletti, M. N. Petrovich, and D. J. Richardson, "Understanding wavelength scaling in 19-cell core hollow-core photonic bandgap fibers," in *Optical Fiber Communication Conference* (Optical Society of America, 2014), p. M2F.4.
197. P. S. J. Russell, P. J. Roberts, and P. Willians, "Photonic bandgap optical waveguide with antiresonant core boundary," U.S. patent 7,346,249 B2 (18 March 2008).
198. E. Numkam Fokoua, S. R. Sandoghchi, Y. Chen, G. T. Jasion, N. V. Wheeler, N. K. Baddela, J. R. Hayes, M. N. Petrovich, D. J. Richardson, and F. Poletti, "Accurate modelling of fabricated hollow-core photonic bandgap fibers," Opt. Express **23**, 23117–23132 (2015).

199. A. Nespola, S. Straullu, T. D. Bradley, H. C. Mulvad, J. R. Hayes, G. T. Jasion, M. A. Gouveia, S. R. Sandoghchi, S. Bawn, F. Forghieri, D. J. Richardson, F. Poletti, and P. Poggiolini, "Record PM-16QAM and PM-QPSK transmission distance (125 and 340 km) over hollow-core-fiber," in *45th European Conference on Optical Communication (ECOC 2019)* (2019), pp. 1–4.
200. A. Nespola, S. Straullu, T. D. Bradley, K. Harrington, H. Sakr, G. T. Jasion, E. Numkam Fokoua, Y. Jung, Y. Chen, J. R. Hayes, F. Forghieri, D. J. Richardson, F. Poletti, G. Bosco, and P. Poggiolini, "Transmission of 61 C-band channels over record distance of hollow-core-fiber with L-band interferers," J. Lightwave Technol. **39**, 813–820 (2021).
201. A. Nespola, S. R. Sandoghchi, L. Hooper, M. Alonso, T. D. Bradley, H. Sakr, G. T. Jasion, E. Numkam Fokoua, S. Straullu, F. Garrisi, G. Bosco, A. Carena, A. M. Rosa Brusin, Y. Chen, J. R. Hayes, F. Forghieri, D. J. Richardson, F. Poletti, and P. Poggiolini, "Ultra-long-haul WDM transmission in a reduced intermodal interference NANF hollow-core fiber," in *2021 Optical Fiber Communications Conference and Exhibition (OFC)* (2021), pp. 1–3.
202. P. Poggiolini and F. Poletti, "Opportunities and challenges for long-distance transmission in hollow-core fibres," J. Lightwave Technol. **40**, 1605–1616 (2022).
203. G. Goubau, "On the excitation of surface waves," Proc. IRE **40**, 865–868 (1952).
204. M. Nakazawa, "Rayleigh backscattering theory for single-mode optical fibers," J. Opt. Soc. Am. **73**, 1175–1180 (1983).
205. M. R. Henderson, S. Afshar V., A. D. Greentree, and T. M. Monro, "Dipole emitters in fiber: interface effects, collection efficiency and optimization," Opt. Express **19**, 16182 (2011).
206. A. Taranta, E. Numkam Fokoua, S. Abokhamis Mousavi, J. R. Hayes, T. D. Bradley, G. T. Jasion, and F. Poletti, "Exceptional polarization purity in antiresonant hollow-core optical fibres," Nat. Photonics **14**, 504–510 (2020).
207. J. Nicholson, L. Meng, J. Fini, R. Windeler, A. DeSantolo, E. Monberg, F. DiMarcello, Y. Dulashko, M. Hassan, and R. Ortiz, "Measuring higher-order modes in a low-loss, hollow-core, photonic-bandgap fiber," Opt. Express **20**, 20494–20505 (2012).
208. T. D. Bradley, N. V. Wheeler, G. T. Jasion, D. Gray, J. Hayes, M. A. Gouveia, S. R. Sandoghchi, Y. Chen, F. Poletti, D. Richardson, and M. Petrovich, "Modal content in hypocycloid Kagomé hollow core photonic crystal fibers," Opt. Express **24**, 15798–15812 (2016).
209. W. Shere, G. T. Jasion, E. N. Fokoua, and F. Poletti, "Design rules for multi-mode anti-resonant hollow-core fibres," in *Optical Fiber Communication Conference (OFC) 2021* (Optical Society of America, 2021), p. F4C.4.
210. C. Goel and S. Yoo, "Multimode nested antiresonant hollow core fiber," J. Lightwave Technol. **39**, 6592–6598 (2021).
211. M. S. Habib, E. Antonio-Lopez, C. Markos, A. Schülzgen, and R. Amezcua-Correa, "Single mode, low-loss 5-tube nested hollow-core anti-resonant fiber," in *Optical Fiber Communication Conference (OFC) 2019* (Optical Society of America, 2019), p. W2A.12.
212. W. B. Gardner, "Microbending loss in optical fibers," Bell Syst. Tech. J. **54**, 457–465 (1975).
213. D. Gloge, "Optical-fiber packaging and its influence on fiber straightness and loss," Bell Syst. Tech. J. **54**, 245–262 (1975).
214. D. Marcuse, "Microbending losses of single-mode step-index and multimode fibers," The Bell Syst. Tech. J. **55**, 937–955 (1976).

215. R. Olshansky, “Mode coupling effects in graded-index optical fibers,” Appl. Opt. **14**, 935–945 (1975).
216. M. Ohashi, K. ichi Kitayama, and S. Seikai, “Mode coupling effects in a graded-index fiber cable,” Appl. Opt. **20**, 2433–2438 (1981).
217. T. Hayashi, T. Sasaki, E. Sasaoka, K. Saitoh, and M. Koshiba, “Physical interpretation of intercore crosstalk in multicore fiber: effects of macrobend, structure fluctuation, and microbend,” Opt. Express **21**, 5401–5412 (2013).
218. P. Sillard, D. Molin, M. Bigot-Astruc, K. De Jongh, F. Achten, J. E. Antonio-Lopez, and R. Amezcua-Correa, “Micro-bend-resistant low-differential-mode-group-delay few-mode fibers,” J. Lightwave Technol. **35**, 734–740 (2017).
219. A. J. Jay, “An overview of macrobending and microbending of optical fibers,” Corning white paper (2017).
220. H. F. Taylor, “Power loss at directional change in dielectric waveguides,” Appl. Opt. **13**, 642 (1974).
221. H. F. Taylor, “Losses at corner bends in dielectric waveguides,” Appl. Opt. **16**, 711 (1977).
222. H. F. Taylor, “Bending effects in optical fibers,” J. Lightwave Technol. **2**, 617–628 (1984).
223. K. Petermann, “Microbending loss in monomode fibres,” Electron. Lett. **12**, 107–109 (1976).
224. K. Petermann, “Fundamental mode microbending loss in graded-index and W fibres,” Opt. Quantum Electron. **9**, 167–175 (1977).
225. K. Petermann and R. Kühne, “Upper and lower limits for the microbending loss in arbitrary single-mode fibers,” J. Lightwave Technol. **4**, 2–7 (1986).
226. M. Artiglia, G. Coppa, and P. di Vita, “New analysis of microbending losses in single-mode fibres,” Electron. Lett. **22**, 623–625 (1986).
227. R. Olshansky, “Distortion losses in cabled optical fibers,” Appl. Opt. **14**, 1974–1975 (1975).
228. J. I. Sakai and T. Kimura, “Practical microbending loss formula for singlemode optical fibers,” IEEE J. Quantum Electron. **15**, 497–500 (1979).
229. J. I. Sakai, “Microbending loss evaluation in arbitrary-lndex singlemode optical fibers. Part II: Effects of core index profiles,” IEEE J. Quantum Electron. **16**, 44–49 (1980).
230. J.-I. Sakai, “Microbending loss evaluation in arbitrary-index single-mode optical fibers. Part I: Formulation and general properties,” IEEE J. Quantum Electron. **16**, 36–44 (1980).
231. Z. Várallyay, T. Mihálffy, S. Bilicz, G. Varga, and K. Mukasa, “Microbending loss properties of different fiber designs,” in *Optical Fiber Communication Conference (OFC) 2021* (Optica Publishing Group, 2021), p. Th1A.49.
232. K. J. Blow, N. J. Doran, and S. Hornung, “Power spectrum of microbends in monomode optical fibres,” Electron. Lett. **18**, 448–450 (1982).
233. S. Hornung, N. J. Doran, and R. Allen, “Monomode fibre microbending loss measurements and their interpretation,” Opt. Quantum Electron. **14**, 359–362 (1982).
234. D. Marcuse, “Coupled power equations for lossy fibers,” Appl. Opt. **17**, 3232–3237 (1978).
235. P. Sillard, S. Richard, L.-A. de Montmorillon, and M. Bigot-Astruc, “Micro-bend losses of trench-assisted single-mode fibers,” in *36th European Conference and Exhibition on Optical Communication* (2010), pp. 1–3.
236. T. Yabuta, C. Tanaka, N. Yoshizawa, and K. Ishihara, “Structural analysis of jacketed optical fiber under lateral pressure,” J. Lightwave Technol. **1**, 529–535 (1983).

237. F. Cocchini, “The lateral rigidity of double-coated optical fibers,” J. Lightwave Technol. **13**, 1706–1710 (1995).
238. K. Okamoto, *Fundamentals of Optical Waveguides*, 2nd ed. (Academic Press, Burlington, 2006).
239. M. Skorobogatiy, S. G. Johnson, S. A. Jacobs, and Y. Fink, “Dielectric profile variations in high-index-contrast waveguides, coupled mode theory, and perturbation expansions,” Phys. Rev. E **67**, 046613 (2003).
240. F. Melli, F. Giovanardi, L. Rosa, and L. Vincetti, “Non-idealities in hollow core inhibited coupling fibers,” *International Conference on Transparent Optical Networks*, 2020-July (2020), pp. 4–7.
241. M. Skorobogatiy, M. Ibanescu, S. G. Johnson, O. Weisberg, T. D. Engeness, M. Soljačić, S. A. Jacobs, and Y. Fink, “Analysis of general geometric scaling perturbations in a transmitting waveguide: fundamental connection between polarization-mode dispersion and group-velocity dispersion,” J. Opt. Soc. Am. B **19**, 2867–2875 (2002).
242. M. Heiblum and J. Harris, “Analysis of curved optical waveguides by conformal transformation,” IEEE J. Quantum Electron. **11**, 75–83 (1975).
243. W. A. Gambling, H. Matsumura, and C. M. Ragdale, “Curvature and microbending losses in single-mode optical fibres,” Opt. Quantum Electron. **11**, 43–59 (1979).
244. D. Marcuse, “Influence of curvature on the losses of doubly clad fibers,” Appl. Opt. **21**, 4208–4213 (1982).
245. R. T. Schermer and J. H. Cole, “Improved bend loss formula verified for optical fiber by simulation and experiment,” IEEE J. Quantum Electron. **43**, 899–909 (2007).
246. J. B. Pendry, D. Schurig, and D. R. Smith, “Controlling electromagnetic fields,” Science **312**, 1780–1782 (2006).
247. Z. Han, P. Zhang, and S. I. Bozhevolnyi, “Calculation of bending losses for highly confined modes of optical waveguides with transformation optics,” Opt. Lett. **38**, 1778–1780 (2013).
248. M. Bigot-Astruc, F. Gooijer, N. Montaigne, and P. Sillard, “Trench-assisted profiles for large-effective-area single-mode fibers,” in *2008 34th European Conference on Optical Communication* (2008), pp. 1–2.
249. M.-J. Li, P. Tandon, D. C. Bookbinder, S. R. Bickham, K. Wilbert, J. S. Abbott, and D. Nolan, “Designs of bend-insensitive multimode fibers,” in *2011 Optical Fiber Communication Conference and Exposition and The National Fiber Optic Engineers Conference* (2011), pp. 1–3.
250. M. Skorobogatiy, K. Saitoh, and M. Koshiba, “Full-vectorial coupled mode theory for the evaluation of macro-bending loss in multimode fibers: application to the hollow-core photonic bandgap fibers,” Opt. Express **16**, 14945–14953 (2008).
251. M. H. Frosz, P. Roth, M. C. Günendi, and P. S. Russell, “Analytical formulation for the bend loss in single-ring hollow-core photonic crystal fibers,” Photonics Res. **5**, 88–91 (2017).
252. J. Olszewski, M. Szpulak, and W. Urbanczyk, “Effect of coupling between fundamental and cladding modes on bending losses in photonic crystal fibers,” Opt. Express **13**, 6015–6022 (2005).
253. G. K. Alagashev, A. D. Pryamikov, A. F. Kosolapov, A. N. Kolyadin, A. Y. Lukovkin, and A. S. Biriukov, “Impact of geometrical parameters on the optical properties of negative curvature hollow-core fibers,” Laser Phys. **25**, 055101 (2015).

254. R. M. Carter, F. Yu, W. J. Wadsworth, J. D. Shephard, T. Birks, J. C. Knight, and D. P. Hand, “Measurement of resonant bend loss in anti-resonant hollow core optical fiber,” Opt. Express **25**, 20612–20621 (2017).
255. V. Setti, L. Vincetti, and A. Argyros, “Flexible tube lattice fibers for terahertz applications,” Opt. Express **21**, 3388 (2013).
256. Y. Wang and W. Chang, “Understanding bending-induced loss and bending-enhanced higher-order mode suppression in negative curvature fibers,” Opt. Express **29**, 23622–23636 (2021).
257. T. P. Hansen, J. Broeng, C. Jakobsen, G. Vienne, H. R. Simonsen, M. D. Nielsen, P. M. W. Skovgaard, J. R. Folkenberg, and A. Bjarklev, “Air-guiding photonic bandgap fibers: spectral properties, macrobending loss, and practical handling,” J. Lightwave Technol. **22**, 11–15 (2004).
258. Y. Chen, S. R. Sandoghchi, E. Numkam, T. D. Bradley, J. R. Hayes, N. V. Wheeler, G. Jasion, D. R. Gray, F. Poletti, M. N. Petrovich, and D. J. Richardson, “Detailed study of macrobending effects in a wide transmission bandwidth hollow-core photonic bandgap fiber,” in *Micro-Structured and Specialty Optical Fibres IV*, Vol. 9886 K. Kalli and A. Mendez, eds., International Society for Optics and Photonics (SPIE, 2016), pp. 141–146.
259. C. Wei, C. R. Menyuk, and J. Hu, “Bending-induced mode non-degeneracy and coupling in chalcogenide negative curvature fibers,” Opt. Express **24**, 12228 (2016).
260. S. A. Mousavi is preparing a manuscript to be titled “Bend-induced propagation effects in hollow-core antiresonant fibers.”
261. K. Nagayama, M. Kakui, M. Matsui, T. Saitoh, and Y. Chigusa, “Ultra-low-loss (0.1484 dB/km) pure silica core fibre and extension of transmission distance,” Electron. Lett. **38**, 1168–1169 (2002).
262. H. C. Mulvad, S. M. A. Mousavi, V. Zuba, L. Xu, H. Sakr, T. Bradley, J. Hayes, G. Jasion, E. Numkam Fokoua, A. Taranta, S. Alam, D. Richardson, and F. Poletti, “Kilowatt-average-power single-mode laser light transmission over kilometre-scale hollow-core fibre,” Nat. Photonics **16**, 448–453 (2022).
263. E. Numkam Fokoua, S. M. A. Mousavi, G. Jasion, D. Richardson, and F. Poletti, “Data for Loss in hollow-core optical fibers: mechanisms, scaling rules, and limits,” University of Southampton, 2023, https://doi.org/10.5258/SOTON/D2391.

Eric Numkam Fokoua received the BSc degree in Microelectronics from Nankai University, Tianjin, China, in 2008, MSc degrees in photonics from the Universities of St Andrews, Scotland, UK, and Ghent, Belgium, in 2010 and a PhD degree in optoelectronics from the Optoelectronics Research Centre, University of Southampton, UK, in 2014 for work on the numerical modeling of hollow-core Optical fibers. His research interests include theoretical and numerical analysis of optical waveguides, in particular light propagation in microstructured and hollow-core optical fibers and their applications. He currently holds a Royal Academy of Engineering University Research Fellowship and has been the recipient of the Corning Outstanding Student paper award (2012) and the Tingye Li Innovation Prize (2019).

Seyed Mohammad Abokhamis Mousavi received his MSc in electrical-electronics engineering from Amirkabir University of Technology (2008) before moving to Southampton, where he received his MSc and PhD degrees from the Optoelectronics Research Centre, Southampton, UK (2018). His PhD research has focused on designing and modeling new hollow-core fibers and studying the nonlinear optical effects in gas-filled hollow-core fibers. In 2018, he started a new role as Research Fellow at Optoelectronics Research Centre, where his research focuses on the design and study of new hollow-core fibers for sensing applications. His main interests include hollow-core fibers for special applications, nonlinear optics, coherent control on metamaterials, and quantum photonics.

Gregory Jasion obtained his MEng in Aerospace engineering at the University of Southampton in 2008. He completed his PhD on helicopter dust clouds in 2013 and subsequently joined the Microstructured Optical Fibres group in the Optoelectronics Research Centre as a specialist in numerical modeling of multiphase flow. He was awarded a Research Fellowship from the Royal Academy of Engineering in 2016. He has developed several techniques to model the flow of glass during microstructured fiber draws, allowing the team to draw fibers virtually. This work is vital to the multiple low loss records in hollow-core fibers achieved at the ORC.

David J. Richardson received the BSc and PhD degrees in fundamental physics from Sussex University, Brighton, UK, in 1985 and 1989, respectively. He joined the Optoelectronics Research Centre (ORC), Southampton University, Southampton, UK, in 1989 and was awarded a Royal Society University Fellowship in 1991 in recognition of his pioneering work on short pulsed fiber lasers. He has served as Deputy Director of the ORC with responsibility for optical fiber and laser-related research since 2000. His current research interests include optical fiber communications, microstructured optical fibers, and pulsed high-power fiber lasers. He is a prominent figure in the international photonics community and has published more than 500 journal papers and produced more than 20 patents. He was elected as a Fellow of the Royal Academy of Engineering in 2009 and most recently as a Fellow of the Royal Society in 2018. He is also a Fellow of the IEEE, Optica, and IET.

Francesco Poletti received the Laurea degree in electronics engineering from the University of Parma, Parma, Italy, and the PhD degree from the Optoelectronics Research Centre (ORC), Southampton, UK, in 2000 and 2007, respectively. He is currently a Professor with the ORC. He has worked for 3 years on optical network design at Marconi Communications and for more than 10 years on the development of new generations of microstructured optical fibers at the ORC. He has coauthored more than 80 journal and 200 conference publications and produced four patents. His research interests include the design of photonic bandgap and antiresonant fibers, the development of fiber-optic characterization techniques, and the fabrication of non-silica-based fibers and devices. He is the holder of a European Research Fellowship Consolidator Grant.